The resistivity and permeability of fractured rocks

A dissertation presented
by
Alison Louise Kirkby

In fulfilment of the requirements
for the degree of
Doctor of Philosophy
in the subject of
Geophysics

THE UNIVERSITY
of ADELAIDE

Submitted to the
Department of Earth Sciences,
School of Physical Sciences, Faculty of Sciences

Adelaide, August 2016


THE UNIVERSITY
of ADELAIDE


Australian Government
Geoscience Australia

CONTENTS

LIST OF TABLES

LIST OF FIGURES

ABSTRACT

The resistivity and permeability of fractures and faults

by Alison Kirkby

Fracture permeability is necessary for the development of many unconventional energy resources, as they are often hosted in rocks with low primary permeability. The magnetotelluric (MT) method has previously imaged temporal resistivity changes associated with injection of conductive fluids into the subsurface. This thesis examines MT responses over two areas of the Otway Basin, Australia, to determine what characteristics of natural fractures can be imaged using MT. In addition, the resistivity and permeability of synthetic fractures and 3D fracture networks are modelled, to draw a link between the resistivity values that are measured and the permeability.

One dimensional anisotropic MT inversions in the Koroit region, Victoria, central onshore Otway Basin, delineate strong resistivity anisotropy at 2-3 km depth with a north-northwest strike. The anisotropy strike is consistent with that of known fracture networks in the Koroit region, and the groundwater at this depth is known to be saline. Thus, the resistivity anisotropy is interpreted as fluid-filled fractures and faults, reducing the resistivity in the north-northwest direction. In contrast, anisotropic inversions in the Penola Trough, western Otway Basin, reveal only minor anisotropy that is inconsistent with known fractures from coincident well image log and seismic data. Thus, an isotropic interpretation is consistent with the data here. Likewise, higher resistivities and lower permeabilities have been measured in wells in Penola, compared to Koroit.

The resistivity and permeability of synthetic fractures filled with an electrically conductive fluid change non-linearly as the fractures are incrementally opened. A percolation threshold can be defined, below which the permeability and resistivity are close to the rock matrix values. At the percolation threshold, the permeability increases by three orders of magnitude or more over an aperture change of < 0.1 mm. The resistivity change depends on the ratio of the rock to fluid resistivity but is generally less than the permeability change, and occurs over a wider aperture range. Similar characteristics are observed in 3D fracture networks except that in networks, percolation is controlled by both the fault network density and fault connectivity. Many sparse networks will not percolate no matter how open the faults are. When the fault density is sufficiently high, a percolation threshold can be defined in terms of the mean fault aperture. At the percolation threshold, a change in mean aperture of 0.02 mm changes the perme-

ability by four orders of magnitude and resistivity by a factor of four. The percolation threshold does not necessarily occur at the same aperture for different flow directions, so fault networks near their percolation threshold commonly show anisotropy in both resistivity and permeability.

Therefore, not only are the MT responses in the Koroit region of the Otway Basin consistent with the presence of resistivity anisotropy due to pervasive open fractures and faults, but realistic fault networks can produce such anisotropic resistivities and permeabilities, with the amount of anisotropy highly sensitive not only to the density of faults in an area but also the degree of openness in the fractures themselves.

Thesis Supervisors: Graham Heinson, Simon Holford, Derrick Hasterok

STATEMENT OF ORIGINALITY

I certify that this work contains no material which has been accepted for the award of any other degree or diploma in my name in any university or other tertiary institution and, to the best of my knowledge and belief, contains no material previously published or written by another person, except where due reference has been made in the text. In addition, I certify that no part of this work will, in the future, be used in a submission in my name for any other degree or diploma in any university or other tertiary institution without the prior approval of the University of Adelaide and where applicable, any partner institution responsible for the joint award of this degree.

I give consent to this copy of my thesis when deposited in the University Library, being made available for loan and photocopying, subject to the provisions of the Copyright Act 1968.

The author acknowledges that copyright of published works contained within this thesis resides with the copyright holder(s) of those works.

I also give permission for the digital version of my thesis to be made available on the web, via the University's digital research repository, the Library Search and also through web search engines, unless permission has been granted by the University to restrict access for a period of time.

Signed _____ Date _____

ACKNOWLEDGEMENTS

First and foremost, I would like to thank my supervisors, Graham Heinson, Simon Holford and Derrick Hasterok, for helping me develop such an exciting and relevant project. Thanks also for giving me the freedom to develop my ideas but providing guidance and advice as necessary, and for your continued enthusiasm for this work throughout the project.

Thanks to all my fellow geophysics PhD students and postdocs for making the time spent working here so enjoyable. I've really enjoyed working with you all and having you there to discuss ideas and provide advice when needed. Thanks to Sebastian Schnaidt in particular for sharing this fantastic thesis template.

I'd also like to thank all my family and friends, near and far, for your support. In particular, thank you Tim, for your support, understanding and patience throughout the PhD. Thanks also to Kate, for our many helpful discussions on geophysics (and everything else), whilst running, and potentially more frequent; discussions on running whilst doing geophysics.

Finally, thanks to Hot Rock Ltd (in particular, Mark Elliott and Peter Barnett) for providing the Koroit MT data and supporting information for Chapter 2 and for giving me the freedom to publish and present it, and the Australian Geophysical Observing System (AGOS) for funding to collect the MT data in Chapter 3.

This project was carried out with the assistance of a scholarship from Geoscience Australia, as well as resources from the National Computational Infrastructure, which is supported by the Australian Government.

CHAPTER

ONE

INTRODUCTION

1.1 Contextual Statement

Continuing demand for fossil fuel resources has resulted in increased interest in alternative energy sources in Australia and overseas (Law and Curtis, 2002; Carson et al., 2014). Exploration for hydrocarbons has been expanded to resources contained in unconventional reservoirs with generally lower natural permeability. In an attempt to curb carbon emissions worldwide, renewable resource industries such as geothermal are also being expanded, resulting in increased exploration of unconventional geothermal resources (e.g., Fridleifsson and Elders, 2005; Tester et al., 2007; Barnett and Evans, 2010; Reid and Messeiller, 2013). Both industries have faced challenges associated with developing these new types of targets. Existing exploration workflows that are tailored to the conventional resource types cannot simply be brought across to the unconventional equivalents as the geological settings and/or target depths are often different. Therefore, these industries are facing challenges to their successful development which require technological advancements to overcome.

One of the challenges facing both industries is the ability to characterise the permeability of the subsurface prior to drilling. The permeability can determine whether or not a resource is economic. Geothermal targets require both elevated temperatures at accessible depths, and adequate permeability to allow extraction of hot fluids at an economic rate. However, primary permeability, present at the time of deposition of sedimentary rocks, is often not preserved at the high temperatures and pressures present in geothermal settings. Therefore, secondary permeability, which includes permeability in fractures and faults, is vital to the success of such projects. Unconventional oil and gas reserves are often contained in rocks with naturally low permeability, such as shale formations. It is often possible to create fractures through hydraulic stimulation. However, this job is made substantially easier (and more cost-effective) by targeting rocks with pre-existing open fractures.

One of the major challenges with targeting fracture permeability is that it can vary by orders of magnitude over length scales of kilometres to metres or less. Measurements on core samples or from well tests provide a very good estimate of the local permeability, however the variability makes it difficult to extrapolate these measurements very far from the well. This makes it difficult to characterise the permeability without drilling directly into the target, which is expensive when the target is at 3-4 km depth or greater.

The seismic reflection method has traditionally been the main method used to map reservoir properties prior to drilling. It has been used for decades in the oil and gas industry, with 3D seismic surveys first being used commercially in the 1970s (Davies et al., 2004). One of the more recent applications of 3D seismic is in the exploration of both unconventional hydrocarbon and unconventional geothermal targets (e.g. Lüschen et al., 2014, 2015). However, seismic reflection data, particularly 3D seismic surveys, are expensive to collect, and, while they can provide detailed information of the distribution of fractures, they not directly sensitive to the presence of pore fluid and its interconnectivity (e.g. MacGregor et al., 2001). The magnetotelluric (MT) method, on the other hand, is a low cost technique that is directly sensitive to the resistivity contrasts that can be induced by the presence of interconnected conductive fracture fill material such as saline fluids. The MT method has recently shown promise in detecting the addition of fluids during hydraulic fracturing of Australian unconventional geothermal and shale gas prospects (Peacock et al., 2012, 2013; Rosas-Carbajal et al., 2015; Rees et al., 2016a) as well as detecting changes due to coal seam gas depressurisation (Rees et al., 2016c). In this thesis, the utility of MT in detecting fluid contrasts prior to drilling will be assessed.

1.2 Background

1.2.1 Geophysical methods applied to permeability exploration

The geophysical methods most widely used in the exploration of permeability are the seismic reflection method in the oil and gas industry, and electrical methods, including MT, in the conventional geothermal industry (Wright et al., 1985; Davies et al., 2004; Muñoz, 2014). In this section, the application and scope of each of these methods for exploration of permeability is discussed.

One of the primary uses of the seismic reflection method is for mapping sedimentary basin structure, as it is able to precisely locate structural boundaries (e.g. Davies et al., 2004). The seismic reflection method is also sensitive to changes in physical properties that affect the acoustic velocity, such as porosity (e.g. Pramanik et al., 2004) which can then be related empirically to permeability through empirical or petrophysical relationships (e.g. Kozeny, 1927; Carman, 1937; Nelson, 1994; Pape et al., 1999). Seismic reflection data is also used to map the location of subsurface fractures through the calculation of attributes such as similarity and curvature (e.g. Roberts, 2001; Backé et al., 2011; Bailey et al., 2014). Assuming the fractures are open, the fracture density

identified on seismic data then provides an estimate of permeability variations. However, in order to determine the fracture fill material, and identify whether the fractures on seismic are open or not, data from well logs, borehole image logs or core sample measurements must be used (Bailey et al., 2014).

Electromagnetic (EM) techniques such as MT may be more useful in identifying the nature of the fracture fill in such situations. These methods provide information on the fracture fill material and its connectedness that may complement seismic reflection data and interpretations (Jones, 1987; MacGregor et al., 2001). Techniques that measure the resistivity of the subsurface have traditionally been used to map the low resistivity anomalies that commonly occur above the upflow zone of conventional geothermal targets, resulting from high temperature clay alteration of the host rock (e.g. Wright et al., 1985; Ussher et al., 2000; Muñoz, 2014). The target is the higher resistivity zone below the clay cap. However, a clay alteration zone is not always present in unconventional geothermal settings, and where it is present, it may not be visible due to the low background resistivities often present in sedimentary basins (e.g Peacock, 2012; Kirkby et al., 2015; Didana, 2016).

The MT method was applied to an unconventional geothermal target in 2011, when Peacock et al. (2012, 2013) carried out MT monitoring of an enhanced geothermal system near Paralana, South Australia. Magnetotelluric data were collected before, during, and after injection of a conductive fluid into a natural fault network at 3.6 km depth. Changes in the resistivity along the strike of the fault network were observed during and after injection, showing that the presence of fluid-filled fractures at depth can produce measurable changes in the subsurface resistivity.

Electromagnetic techniques are less widely applied in the oil and gas industry, although they are increasingly being used to complement the information contained in seismic data (e.g. Hoversten et al., 2003). More recently, however, MT was used to monitor fluid injection in a shale gas prospect, and coal seam gas depressurisation (Rees et al., 2016a,b,c). The resistivities are often linked to porosity through relationships such as Archie's Law (Archie, 1942). The porosities can be used as a link to the seismic data, for use in joint inversion algorithms (e.g. Hoversten et al., 2003) or linked to permeability (e.g. Nelson, 1994; Pape et al., 1999). However, Archie's Law was empirically determined in porous rocks where the majority of the fluid and current passes through the rock matrix. In low porosity, fractured rocks, both the current and fluid flow paths are likely to be different compared to porous rocks, since both fluid flow and electrical conduction rely on the connectivity of the pore space as well as the total volume (e.g. Brown, 1989).

1.2.2 The magnetotelluric method

The MT method measures time variations in the Earth's electric ($\mathbf{E}$) and magnetic ($\mathbf{B}$) fields (Tikhonov, 1950; Cagniard, 1953; Simpson and Bahr, 2005; Chave and Jones, 2012). These measurements are related to the impedance tensor $\mathbf{Z}$ through the relationship

$$\begin{bmatrix} E_i \\ E_j \end{bmatrix} = \begin{bmatrix} Z_{ii} Z_{ij} \\ Z_{ji} Z_{jj} \end{bmatrix} \begin{bmatrix} B_i \\ B_j \end{bmatrix} \tag{1.1}$$

Where i and j are indices of the orthogonal **E** and **B** fields. The impedance tensor provides information on the resistivity of the subsurface in the frequency domain. The apparent resistivity, or resistivity of an equivalent uniform half-space, is related to **Z** through

$$\rho_{app,\ ij} = \frac{T}{2\pi\mu_0} |Z_{ij}|^2 \tag{1.2}$$

where Z_{ij} represents the elements of the impedence tensor **Z** as defined in Equation 1.1. The corresponding depth can be approximated by the electromagnetic skin depth d, defined as

$$d = \sqrt{T\rho_{app}/\pi\mu_0} \approx 500\sqrt{T\rho_{app}} \tag{1.3}$$

where μ_0 is the magnetic permeability and T is the period. The skin depth is the depth at which the corresponding surface **B** fields are attenuated by $e^{-1} \approx 37$ %.

The MT phase tensor provides information on the dimensionality of the data **Φ** and is given by

$$\mathbf{\Phi} = Re(\mathbf{Z})^{-1} Im(\mathbf{Z}) \tag{1.4}$$

and can be depicted as an ellipse (Bibby, 1986; Caldwell et al., 2004). If the geoelectric structure is 1D, the ellipse is a circle (Caldwell et al., 2004; Heise et al., 2006). If it is 2D, the orientation of the major axis of the ellipse is either parallel or perpendicular to the geoelectric strike (Bibby, 1986; Caldwell et al., 2004). Likewise, in the case of a 1D model with anisotropy (e.g. isotropic layer overlying an anisotropic layer) the orientation of the major axis aligns either perpendicular or parallel to anisotropy strike (Heise et al., 2006).

1.2.3 Anisotropy vs heterogeneity in MT data interpretation

Anisotropy is the dependence of a property on orientation and can either be present in the rock fabric itself or, in many cases, macro-scale anisotropy might be observed from mixing of two materials with different resistivities (Wannamaker, 2005; Martí, 2014).

Magnetotelluric data are usually interpreted isotropically unless an isotropic model fits the data poorly or there is specific evidence for anisotropy (e.g. Heise and Pous, 2003; Naif et al., 2013). However, measurements from well logs and on core samples have shown that upper crustal rocks are commonly anisotropic, with anisotropy often resulting from sedimentary layering, fractures and faults filled with a conductive material,

the rock fabric, or a combination of these (e.g. Wang and Fang, 2001; Kennedy et al., 2004; Herwanger et al., 2004; Cook et al., 2010; Nabawy et al., 2010; Newman et al., 2010). Furthermore, resistivity-based borehole image logs such as FMS and FMI are routinely used to map the location and orientation of electrically conductive fractures intercepted by a well, and these normally show a preferred orientation of conductive fractures (e.g Backé et al., 2011; Bailey et al., 2014). Anisotropy should therefore be considered when modelling and interpreting MT datasets.

One complication in interpreting MT datasets anisotropically is there can be no difference in the impedance tensor at a single site between a 2D isotropic and 1D anisotropic subsurface (e.g. Heise et al., 2006). In order to distinguish between isotropic and anisotropic models, the presence or absence of lateral variations in resistivity can sometimes be inferred through arrays of measurements, other geoscientific data, or through calculation of induction vectors (Martí, 2014). However, it is often the case that both lateral variations and anisotropy are present, and it can be problematic separating the two effects.

Where macro-scale anisotropy can be detected, it may be useful in characterising the orientation of electrically conductive fractures and the amount by which they enhance the conductivity. If the fractures are found to be fluid-filled (through analysis of well logs, or in the case of MT monitoring, by measuring characteristics of the injected fluid), then it may be possible to link this conductivity enhancement to enhancement of the permeability.

1.2.4 The resistivity and permeability of fractured rocks

Numerical modelling of the electrical and flow properties of synthetic fractured rocks may help to provide a link between the resistivities measured in fluid-filled fractured rocks and permeability (e.g. Brown, 1989; Bernabé, 1995; Van Siclen, 2002; Madadi et al., 2003). An advantage of numerical modelling over direct measurement of resistivity and permeability is that it can be carried out relatively quickly and inexpensively compared to core sample or well log measurements, and can easily be repeated using a range of different parameters. In this way, it is possible to investigate which parameters have the strongest control on the electrical and flow properties of fractured rocks.

1.2.4.1 Resistor networks

A resistor network approach is a simple method for analysing the electrical and flow properties of materials containing two or more phases, and was applied by Bahr (1997) to analyse the connectivity of lower crustal rocks containing highly conductive material in micro-cracks. A similar approach was applied in the analysis of fluid flow by Guéguen et al. (1991). In the analysis by Bahr (1997), the conductivity of the rocks was assessed via a connectivity factor.

The connectivity, C, was defined in terms of the Hashin–Shtrikman upper bound for any given mixing ratio of high and low conductivity materials (Hashin and Shtrikman,

1963). The perfectly interconnected case was defined by the upper bound and assumes the conductivity of the high conductivity material is much higher than that of the lower conductivity material:

$$\sigma_{eff} = \frac{2}{3}\beta\sigma_m \tag{1.5}$$

Where σ_{eff} is the effective conductivity of the mixture, β is the ratio of the high conductivity material to low conductivity material; and σ_m is the conductivity of the high conductivity material. The connectivity can be included in this model by incorporating a dimensionless factor C describing the electrical connectivity of the high conductivity material (Bahr, 1997). Equation 1.5 then becomes:

$$\sigma_{eff} = \frac{2}{3}C\beta\sigma_m \tag{1.6}$$

C ranges from 0 to 1, and describes the interconnectivity of the high conductivity phase within the medium.

Bahr (1997) used random resistor networks to evaluate C. Electrical current flow was assumed to occur through a network of resistors, which could be defined to be open (i.e., conductive) or closed to electrical current flow (i.e., resistive). These resistors are analogous to faults within a fracture network that contain an electrically conductive phase and those that are closed, or cemented with electrically resistive cement. Importantly, the value of C is controlled not only by the total number of bonds that are blocked, but also on the position of the blocked bonds within the network. The resistors were assigned randomly according to a probability of connection, P. Furthering this concept, embedded networks were analysed, where, instead of being either conductive or resistive, a bond could contain a new network. Embedded networks were used in order to replicate changes in conductivity on different scales (Bahr, 1997). The probability P was then progressively increased, analysing C at each point, to define a percolation threshold for the network. At low values of P, the high conductivity phases were not connected and C was therefore close to zero. As P was increased, C increased gradually, until the network reached its percolation threshold and the connectivity increased by a large amount. By slightly varying P in two directions, Bahr (1997) was able to replicate the anisotropy identified in crustal MT surveys.

1.2.4.2 Percolation theory

The work presented by Bahr (1997) demonstrates a characteristic of both permeability and resistivity that they are dependent on the distribution as well as the volume fraction of the electrically (or hydraulically) conductive phase. Linearly increasing the amount of the conductive phase present in a rock does not correspond to a linear increase in the electrical conductivity or permeability, and a percolation threshold can be defined, at which point the conductivity or permeability increases rapidly (e.g. Guéguen et al., 1991; Bahr, 1997; Berkowitz, 2002). In classical percolation theory, there is no conduction and fluid flow in the surrounding rock mass, and the permeability and conductivity is solely dependent on the conductive phase (Berkowitz, 2002). This implies that the properties of the rockmass are governed by the connectivity of the backbone

network, i.e. the part of the network that is fully connected (Bour and Davy, 1997; Berkowitz, 2002).

In reality, the conductivity and permeability in any rockmass is non-zero. This means that disconnected parts of the fracture network will have some finite contribution to the overall hydraulic and electric properties of the network. In cases where the contrast between the matrix and fracture or fluid properties are not extreme, this contribution may be significant and thus may alter the percolation behaviour that is observed.

1.2.4.3 Fracture modelling in realistic fractures

The resistor network approach applied by Bahr (1997) could be extended further by modelling fluid and current flow in fractures with realistic aperture distributions as fractures open. This approach has the advantage that the modelling can be interpreted in terms of physically meaningful characteristics of the fractures. Fractures are self-similar (e.g. Brown, 1987), and show predictable patterns in both the elevation of each fracture surface, and the mismatch between opposing fractures. They can therefore be replicated using a simple mathematical model (Brown, 1987). Brown (1989) used this method to model current and fluid flow through synthetic fractures with no horizontal offset between the plates, using a local parallel plate approximation to carry out the fluid flow modelling, and Ohm's Law for electrical current flow. The parallel plate approximation is a simplification of the Navier-Stokes equations for laminar fluid flow that assumes the fracture consists of a series of flat plates.

Applying the parallel plate model and Ohm's Law for fluid and current flow is of course a simplification of the flow processes occurring in real fractures. Many authors have carried out modelling using more complex models that incorporate other processes or effects, for example, permeable fracture walls, or use the full Navier-Stokes equations (e.g. Berkowitz, 1989; Brown et al., 1995; Al-Yaarubi et al., 2005; Crandall et al., 2010; Mohais et al., 2012). However, these more complex approaches can be considerably more expensive computationally and therefore there are restrictions on the size of problems that can be computed. A simplified approach is sometimes sufficient to address the problem of interest. For example, Brush and Thomson (2003) showed the parallel plate model, modified to incorporate the local slope of the fracture planes, provided a good approximation to the full Navier-Stokes equations for their tested fracture geometries at the low flow velocities likely to be encountered in the subsurface. Applying a simplified, computationally inexpensive method opens up the possibility of running many simulations to investigate the influence of different fracture and rock parameters on their transport and electrical properties.

1.3 Objectives

This thesis aims to help address the challenge of predicting permeability from the surface using the MT method. The following questions will be examined:

- Can MT array data be used to infer the distribution of subsurface fractures, and their characteristics (including fill material and degree of interconnectivity)?
- What resistivity characteristics might we expect in fractured rocks filled with an electrically conductive fluid, and how do these characteristics relate to permeability?
- What do MT responses look like in areas that we know (based on data from well and seismic reflection data) contained fractured rocks?

To address these questions, the MT method is used to characterise the subsurface resistivity using both isotropic and anisotropic inversions, in two areas of the Otway Basin, Victoria, Australia. Modelling is then carried out on synthetic fractures to determine their resistivity and permeability and thus determine the characteristics we might expect in fractured rocks.

In the first field area, in Koroit, Victoria, there is limited existing information on the basin structure. The data that are available include 2D seismic lines and six resistivity logs. In Chapter 2, MT data are used to further improve the understanding of the resistivity structure and its relationship to the structure. The content of this chapter has been published as: Kirkby, A.L., Heinson, G., Holford, S., and Thiel, S., 2015. Mapping fractures using 1D anisotropic modelling of magnetotelluric data: a case study from the Otway Basin, Victoria, Australia. Geophysical Journal International, v. 201, pp. 1961-1976.

The second field area, the Penola Trough, is very well characterised in terms of its lithology and structure. The availability of 3D seismic reflection data in the survey area, as well as data from sixteen petroleum wells, has allowed prior analyses of the distribution of fractures and faults to be carried out. In Chapter 3, a new MT survey is carried out in this area and used evaluate the influence these known fractures have on the subsurface resistivity. This work has been accepted for publication in the Australian Journal of Earth Sciences.

In Chapters 4 and 5, synthetic modelling is carried out to determine what resistivity and permeability characteristics we might expect in fractured rocks. These properties are evaluated as the fractures are incrementally opened. Chapter 4 looks at the electrical and hydraulic properties of individual fractures, and has been published as: Kirkby, A.L., Heinson, G., and Krieger, L., 2016. Relating permeability and electrical resistivity in fractures using random resistor network models. Journal of Geophysical Research: Solid Earth, v. 121, pp. 1546-1564. Chapter 5 extends this work by considering the resistivity and permeability of fracture networks.

CHAPTER

TWO

MAPPING FRACTURES USING 1D ANISOTROPIC MODELLING OF MAGNETOTELLURIC DATA: A CASE STUDY FROM THE OTWAY BASIN, VICTORIA, AUSTRALIA

Alison Kirkby[1,2], Graham Heinson[1], Simon Holford[1] and Stephan Thiel[1,4]

[1] Electrical Earth Imaging Group, School of Physical Sciences, University of Adelaide, Adelaide, SA 5000, Australia
[2] Geoscience Australia, Canberra, ACT 2601, Australia
[3] Australian School of Petroleum, University of Adelaide, Adelaide, SA 5000, Australia
[4] Geological Survey of South Australia, GPO Box 320, Adelaide, SA 5001, Australia

Published on March 7th, 2015 as:
Kirkby, A.L., Heinson, G., Holford, S., and Thiel, S., 2015. Mapping fractures using 1D anisotropic modelling of magnetotelluric data: a case study from the Otway Basin, Victoria, Australia. Geophysical Journal International, v. 201, pp. 1961-1976.

Statement of Authorship

Title of Paper	Mapping fractures using 1D anisotropic modelling of magnetotelluric data: a case study from the Otway Basin, Victoria, Australia
Publication Status	☑ Published ☐ Accepted for Publication ☐ Submitted for Publication ☐ Unpublished and Unsubmitted work written in manuscript style
Publication Details	Kirkby, A.L., Heinson, G., Holford, S., and Thiel, S., 2015. Mapping fractures using 1D anisotropic modelling of magnetotelluric data: a case study from the Otway Basin, Victoria, Australia. Geophysical Journal International, v. 201, pp. 1961-1976.

Principal Author

Name of Principal Author (Candidate)	Alison Kirkby
Contribution to the Paper	Analysed and modelled data, wrote the manuscript
Overall percentage (%)	85%
Certification:	This paper reports on original research I conducted during the period of my Higher Degree by Research candidature and is not subject to any obligations or contractual agreements with a third party that would constrain its inclusion in this thesis. I am the primary author of this paper.
Signature	Date 10/8/16

Co-Author Contributions

By signing the Statement of Authorship, each author certifies that:

i. the candidate's stated contribution to the publication is accurate (as detailed above);

ii. permission is granted for the candidate in include the publication in the thesis; and

iii. the sum of all co-author contributions is equal to 100% less the candidate's stated contribution.

Name of Co-Author	Graham Heinson
Contribution to the Paper	Supervised and aided in MT data interpretation, critical analysis, and manuscript evaluation
Signature	Date 8TH AUG 2016

Name of Co-Author	Simon Holford
Contribution to the Paper	Contributed to geological interpretation and manuscript evaluation
Signature	Date 10/8/16

Name of Co-Author	Stephan Thiel		
Contribution to the Paper	Contributed to data interpretation and manuscript evaluation		
Signature		Date	09/08/16

SUMMARY

We present 1D anisotropic inversion of magnetotelluric (MT) data as a potential tool for mapping structural permeability in sedimentary basins. Using 1D inversions of a 171 site, broadband MT dataset from the Koroit region of the Otway Basin, Victoria, Australia, we have delineated an electrically anisotropic layer at approximately 2.5 to 3.5 km depth. The anisotropy strike is consistent between stations at approximately 160 ° east of north. The depth of anisotropy corresponds to the top depth of the Lower Cretaceous Crayfish Group, and the anisotropy factor increases from west to east. We interpret the anisotropy as resulting from north-northwest oriented, fluid-filled fractures resulting in enhanced electrical and hydraulic conductivity. This interpretation is consistent with permeability data from well formation tests. It is also consistent with the orientation of mapped faults in the area, which are optimally oriented for reactivation in the current stress field.

2.1 Introduction

The ability to predict crustal permeability distribution is important for a number of resource industries, for example, geothermal energy and oil and gas. Geothermal energy targets require both elevated temperatures at accessible depths, and sufficient permeability to sustain adequate flow rates for commercial production. Likewise, understanding the permeability distribution is vital to accurately model the performance of an oil or gas reservoir (Babadagli and Al-Salmi, 2004).

Electromagnetic techniques have been applied extensively to exploration for conventional geothermal targets (e.g., Pellerin et al., 1996; Muñoz, 2014). In conventional geothermal systems, the target is a strong electrical conductivity anomaly resulting from a clay cap caused by alteration of the host rock to electrically conductive clay minerals (Wright et al., 1985; Ussher et al., 2000). However, enhanced geothermal energy targets such as those being investigated in Australia (e.g., Barnett and Evans, 2010; Hogarth et al., 2013; Reid and Messeiller, 2013) are generally deeper and are located in a range of geological settings, making the application of a single exploration model difficult. In addition, the rocks in many of the sedimentary basins in Australia are highly electrically conductive (e.g., Peacock et al., 2013) and therefore high conductivities resulting from, for example, saline fluids or clay alteration may not produce strong conductivity anomalies. For these reasons, the application of electromagnetic techniques such as MT may be less straightforward in exploration for unconventional geothermal resources.

Time lapse MT monitoring of an enhanced geothermal system near Paralana, South Australia was performed in 2011 (Peacock et al., 2012, 2013; MacFarlane et al., 2014). In this experiment, MT data were collected pre- and post-injection of an electrically conductive fluid into a natural fault network at 3.6 km depth. Much stronger increases

in electrical conductivity were observed parallel to the strike of the fault network than perpendicular to it, consistent with an increase in hydraulic (and electrical) conductivity. These observations show that the presence of fluid-filled fractures in a medium changes the effective electrical conductivity that is measured.

To date, electromagnetic techniques have had limited application in the oil and gas industry, where seismic reflection data is routinely used to map reservoir properties (e.g., Russell et al., 1997; Hart and Balch, 2000). Seismic and well log data are used to infer properties such as porosity and water saturation. Alternatively, electrical resistivity logs can be used to derive porosity through Archie's Law (Archie, 1942). The porosities can then be linked to permeability, through either empirical or petrophysically-based relationships (e.g., Nelson, 1994; Pape et al., 1999). However, the application of these relationships can be problematic in that they do not generalise well: an equation that works well for a particular rock may not be useful for another, even if they are lithologically similar (Babadagli and Al-Salmi, 2004). A simpler approach may be the use of the electrical resistivity information directly to characterise the subsurface permeability distribution.

The Australian Otway Basin has long been a target for petroleum exploration, with the first commercial discovery in 1987 (O'Neil, 2002). As a result, substantial seismic and well data exist for the Otway Basin, and these data have been used to characterise the regional structure and stress field (e.g., Hillis et al., 1995; Vandenberg, 2000; Nelson et al., 2006). More recently, the Otway Basin has been of interest for geothermal energy, with exploration occurring in the Tyrendarra Embayment near Koroit, Victoria (e.g., Barnett and Evans, 2010) and in the Penola Trough (e.g., de Graaf et al., 2010). In 2008, an MT dataset was collected for Hot Rock Ltd to identify the distribution of heat and fluids near Koroit. We present 1D anisotropic modelling of these data as a potential tool for mapping hydraulic conductivity in sedimentary basins.

2.2 The Magnetotelluric Method

The magnetotelluric (MT) method, first formulated by Tikhonov (1950) and Cagniard (1953), is a passive geophysical technique that measures time variations in orthogonal components of the Earth's electrical ($\mathbf{E}$) and magnetic ($\mathbf{B}$) fields. The measurements provide information on the electrical conductivity structure of the subsurface in the frequency domain. The impedance tensor $\mathbf{Z}$ is related to the horizontal components of the $\mathbf{E}$ and $\mathbf{B}$ fields through the relationship $\mathbf{E} = \mathbf{ZB}$.

Electromagnetic waves diffuse as they pass through the Earth with the depth of penetration related to the period of the inducing magnetic field. The electromagnetic skin depth d, or the depth at which the electromagnetic fields are attenuated to e^{-1} of their surface amplitudes, is defined as $d = \sqrt{T\rho_{app}/\pi\mu_0} \approx 500\sqrt{T\rho_{app}}$, where μ_0 is the magnetic permeability, equal to $4\pi \times 10^{-7} N/A^2$, T is the period, and ρ_{app} is the apparent

resistivity, or resistivity of an equivalent uniform half-space. The apparent resistivity is related to $\mathbf{Z}$ through

$$\rho_{app,\ ij} = \frac{T}{2\pi\mu_0}|Z_{ij}|^2 \tag{2.1}$$

where Z_{ij} represents the elements of the impedence tensor $\mathbf{Z}$.

The MT phase tensor (Caldwell et al., 2004) is the ratio of the imaginary part of the impedance tensor to the real part, $\mathbf{\Phi} = Re(\mathbf{Z})^{-1}Im(\mathbf{Z})$. The phase tensor is free of distortion, which can affect the apparent resistivity values, and can be depicted as an ellipse (Bibby, 1986; Caldwell et al., 2004). The orientation of the ellipse is either parallel or perpendicular to the geoelectric strike. To overcome this ambiguity in geoelectric strike, the vertical magnetic field information can also be utilised through calculation of induction vectors. Induction vectors are a representation of the complex ratio of the vertical to horizontal magnetic field components. Vertical magnetic fields are induced by lateral variations in conductivity, and therefore induction vectors can be used to infer the presence and direction of lateral conductivity variations.

Because MT is a diffusive technique, resolution decreases with depth of penetration. As a result, fractures spaced less than 1 to 2 km apart are unlikely to be individually resolved at depths greater than a few kilometres. Instead, such features may be detected as larger scale electrical anisotropy. Electrical anisotropy is the variation in electrical resistivity with orientation (Wannamaker, 2005). It is often the result of mixing of different materials with contrasting electrical conductivities, for example fractures filled with an electrically conductive material. In these circumstances, anisotropic models are substitute models, as the rocks themselves are not anisotropic, but structural anisotropy results from the presence of fractures and faults.

Evidence for anisotropy can sometimes be found in the impedance tensor. For example, anisotropy can result in the diagonal impedance phase values falling outside the normal ranges of [0 °, 90 °] and [180 °, 270 °] (e.g., Heise and Pous, 2003; Weckmann et al., 2003). However, such characteristics are not always present, and there is often no observable difference in the impedance tensor $\mathbf{Z}$ between the 2D isotropic and 1D anisotropic case. In this case, other information (e.g. arrays of measurements, induction vectors, other geophysical or geological information) must be utilised to determine if anisotropy is present.

2.3 The Otway Basin

2.3.1 Regional structure and stress field

The Australian Otway Basin covers southern Victoria, South Australia and Tasmania and extends offshore (Figure 2.1). The basin is broadly west-northwest trending, and developed along the Australian southern margin as a result of Jurassic to Cretaceous rifting of the Australian continent from Antarctica (Perincek and Cockshell, 1995). Sedimentation commenced with the deposition of the Casterton Formation, followed

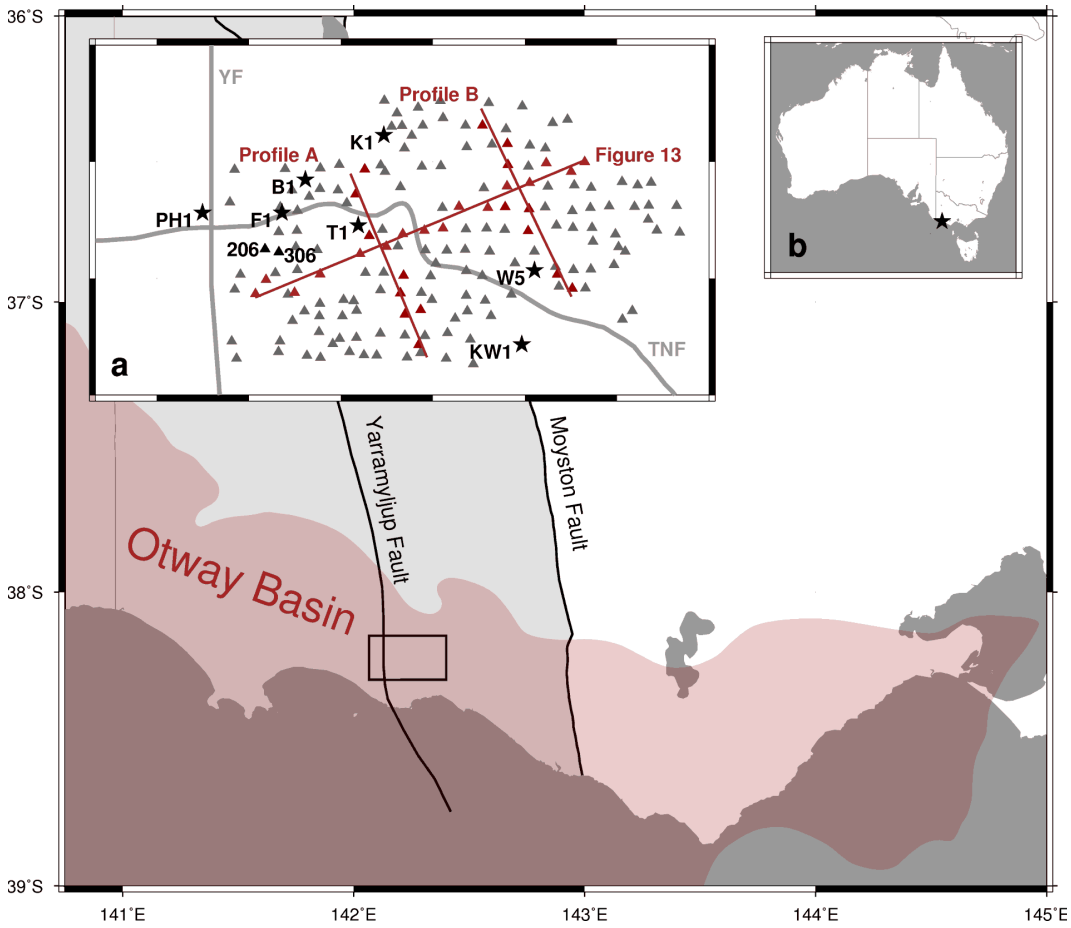

Figure 2.1: Map showing the regional geology and MT station locations. Delamerian Fold Belt (light grey), Lachlan Fold Belt (white), water bodies (dark grey) onshore Otway Basin (light pink), offshore Otway Basin (dark pink), and Yarramyljup and Moyston Faults. Inset (a) MT stations (grey triangles), Stations 206 and 306 (Figure 2.4; black triangles), wells (black stars); T1 = Taralea 1, F1 = Findra 1, KW1 = Koroit West 1, B1 = Banganna 1, K1 = Killara 1, W5 = Warrong 5, and major faults; YF = Yarramyljup Fault, TNF = Tyrendarra North Fault. Profile locations for Figures 7, 9, and 10 (Profiles A and B) and Figure 13 are shown in brown. Inset (b) survey location on a map of Australia.

by the Crayfish Group in the Early Cretaceous. Deposition of the Crayfish Group was followed by a period of uplift, tilting and erosion in the mid-Cretaceous, leaving an unconformity between the Crayfish Group and overlying sediments. The current stress field in the Otway Basin is reverse to strike-slip with the maximum horizontal stress oriented at approximately 135 ° (Hillis et al., 1995; Nelson et al., 2006; Tassone, 2014).

Deposition of the Crayfish Group was concentrated in a series of west to northwest trending depocentres that extend across the Otway Basin (Perincek and Cockshell, 1995). These depocentres include the Tyrendarra Embayment, an approximately west trending half graben in the central Otway Basin (Perincek and Cockshell, 1995).

The orientation of the depocentres within the Otway Basin cross-cuts the north-northwest orientation of basement fabric in the Delamerian Fold Belt, which underlies the Otway Basin within the Tyrendarra Embayment (Vandenberg, 2000).

2.3.2 Lithology and reservoir properties of the Crayfish Group

Sediments of the Crayfish Group have been targeted as a reservoir for both oil and gas and geothermal prospects, due to their high permeability (Morton et al., 2002; Barnett and Evans, 2010; de Graaf et al., 2010). In South Australia, the Crayfish Group has been divided into the Pretty Hill Formation and the overlying Laira Formation and Katnook Sandstone (Boult et al., 2002b). However Ryan et al. (1995) noted that within the Tyrendarrah Embayment, this subdivision is much less clear.

Within the Tyrendarrah Embayment, the Crayfish Group consists mainly of sandstone and siltstone, and less commonly shale, mudstone and claystone (Ryan et al., 1995). Clay minerals present include chlorite and kaolinite (Ryan et al., 1995). The permeability of the Crayfish Group has been measured in Pretty Hill 1 (Figure 2.1), and ranges from 200 to 2800 mD, with a median of 600 mD (Geoscience Australia, 2014; Geoscience Victoria, 2014). Porosity has been measured in Killara 1 and Pretty Hill 1, with medians of 19 % and 22 % for the Crayfish Group respectively. These porosity and permeability values are consistent with measurements on the Pretty Hill Formation of the Crayfish Group elsewhere in the Otway Basin (e.g., Alexander, 1992; Morton et al., 2002).

2.4 Data

2.4.1 Magnetotelluric data

In 2008, 171 MT stations were collected by Quantec Geoscience Ltd for Hot Rock Ltd near Koroit, Victoria, in the Otway Basin (Figure 2.1). The data were collected over a period range of 0.004 to 1000 s. The area is relatively flat topographically, with the surface elevation decreasing by about 75 m from west to east, a distance of about 20 km (Hot Rock Ltd., 2009). The MT data cover an area of approximately 240 km^2, an average station spacing of approximately 1.5 km.

Figure 2.2 shows the data plotted as phase tensor ellipses and induction vectors, plotted using the Parkinson convention (Parkinson, 1959), for periods of 1, 12.5 and 100 s. At a period of 1 s, which, given an apparent resistivity of 5 Ωm, is equivalent to about 1 km depth, the ellipses are close to circular, indicating the geoelectric structure is close to 1D. The phase is approximately 55 °, consistent with a gradual decrease in resistivity with depth as observed at this period across almost all stations. The induction vectors are small with no preferred orientation. At 12.5 s, or about 2.5 to 3 km depth given an apparent resisitivity of 2 to 3 Ωm, the ellipses become elongated, reflecting phase splits in the data, and indicate either 2D structure or electrical anisotropy. The magnitude

of the phase is, on average, approximately 40 ° in the Z_{xy} component and 20 ° in the Z_{yx} component, consistent with an observed increase in apparent resistivity at periods greater than about 12.5 s. The induction vectors at 12.5 s are aligned in a north-northwest to northeast direction, though their magnitudes are small. This, together with the east-northeast orientation of the major axes of the phase tensor ellipses, suggests a geoelectric strike of about 70 °. At periods of 50 to 100 s (depending on the location) and greater, or about 10 to 20 km depth, the induction vectors become aligned in a south-southeast direction.

2.4.2 Resistivity Logs

There are seven wells in the area with resistivity logs, with depth extents ranging from 0.8 to 2.75 km. Their locations are shown in Figure 2.1 and the resistivity logs are shown in Figure 2.3. All seven resistivity logs show similar characteristics despite being in different locations. The resistivity in the top 100 to 200 m is about 10 Ωm, decreasing to 2 to 3 Ωm at about 300 to 400 m depth. Resistivity then increases sharply at the top of the Dilwyn Formation, then gradually decreases with depth, reaching a minimum of about 1 Ωm at approximately 1 km depth, near the top of the Eumeralla Formation. The logs then show a gradual increase in resistivity to about 10 Ωm at 1.8 km depth, and then, in Killara 1, Banganna 1 and Pretty Hill 1, resistivity decreases again at the top of the Crayfish Group.

2.5 Magnetotelluric data distortion removal

At some of the MT stations, there is a frequency-independent shift between the Z_{xy} and Z_{yx} component resistivities at periods up to about 1 s, while the phase angles are the same. For most stations the shift is very small (e.g., Figure 2.4a), however there are some stations that appear to be affected to a larger degree (e.g., Figure 2.4b). Spatially, there is no consistent pattern in both the magnitude and direction of the shift across the study area. Therefore, we interpret the shift to be due to near-surface distortion, and so we have removed this shift from the worst affected stations prior to modelling the data, as described below.

The magnitude of the shift (defined here as the ratio of the median Z_{xy} to Z_{yx} resistivity for the 1D part of the curve) ranges from a factor of 0.1 to 5.7, with most stations within the range 0.6 to 1.5. In order to correct for the shift we corrected either the Z_{xy} or Z_{yx} component depending on the resistivity at a nearby station.

First, the 1D distortion tensor was calculated at each site using the method of Bibby et al. (2005) and used to calculate the ratio of the Z_{xy} and Z_{yx} resistivities. The sites were then divided into three groups. The first group comprised stations where the median Z_{xy} and Z_{yx} resistivities were within a specified threshold of each other (we have chosen 35 %); these stations were assumed to be largely unaffected by static shift and were therefore used to correct the worst affected stations as described below.

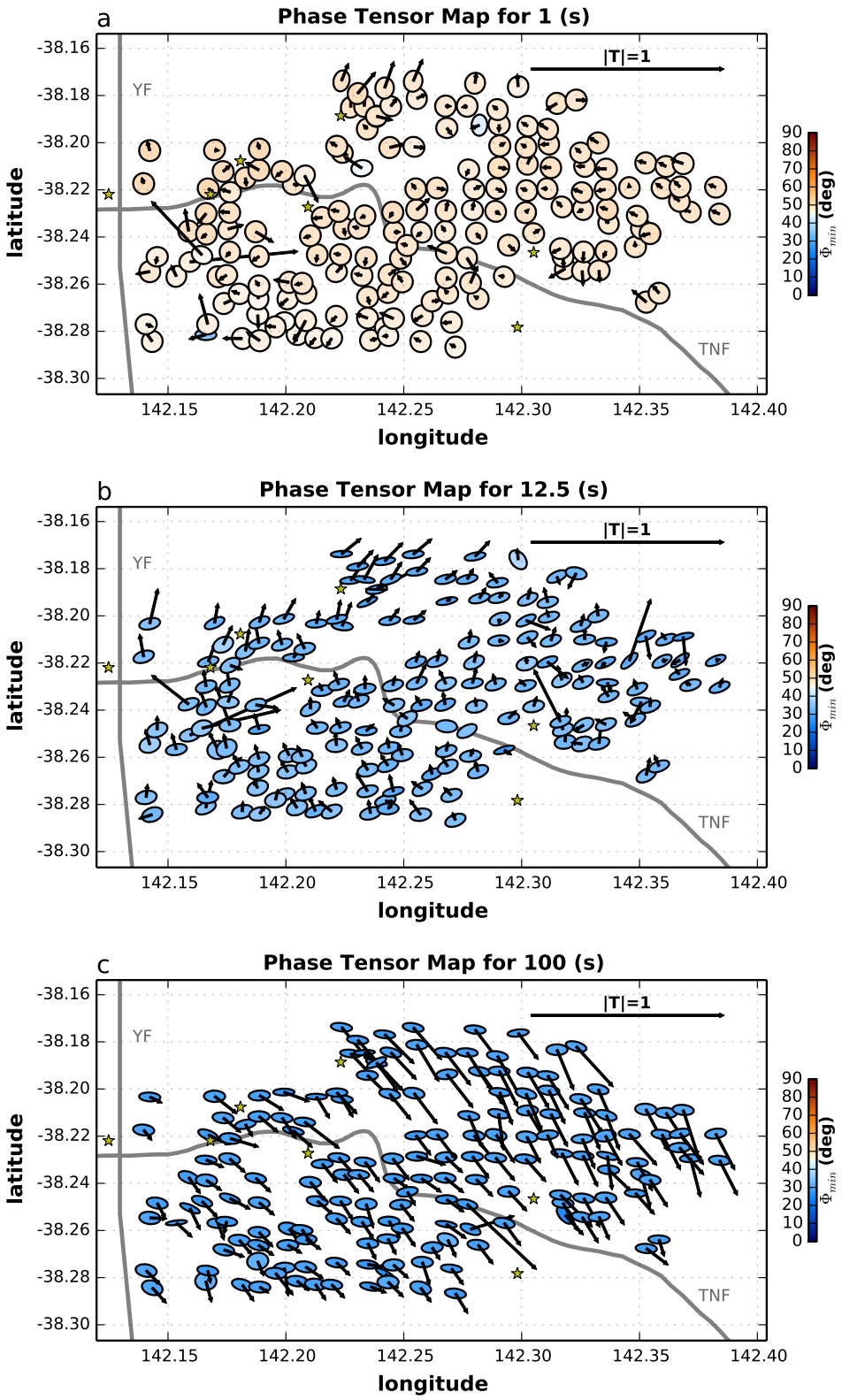

Figure 2.2: Maps showing phase tensor ellipses and induction vectors, plotted using the Parkinson convention (Parkinson, 1959), for periods of (a) 1, (b) 12.5 and (c) 100 s. Ellipses are coloured by the minimum phase, Φ_{min}. Locations of the Yarramyljup Fault (YF) and Tyrendarra North Fault (TNF) (grey lines), and wells (yellow stars) also shown.

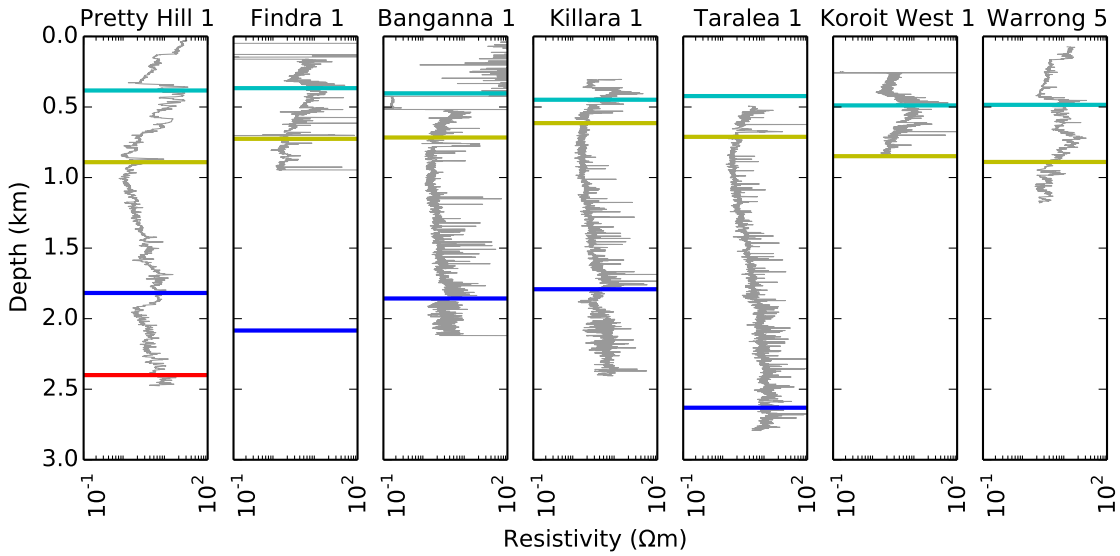

Figure 2.3: Deep resistivity logs for the Koroit region. Stratigraphic units shown as horizontal lines; top Dilwyn Formation (approx. 40 Ma, cyan), top Eumeralla Formation (approx. 96 Ma, yellow), top Crayfish Group (approx. 119 Ma, blue), Basement (approx. 300 Ma, red). Stratigraphic horizon interpretations for Pretty Hill 1 are from Geoscience Victoria (2014) and for all other wells from Hot Rock Ltd. (2009).

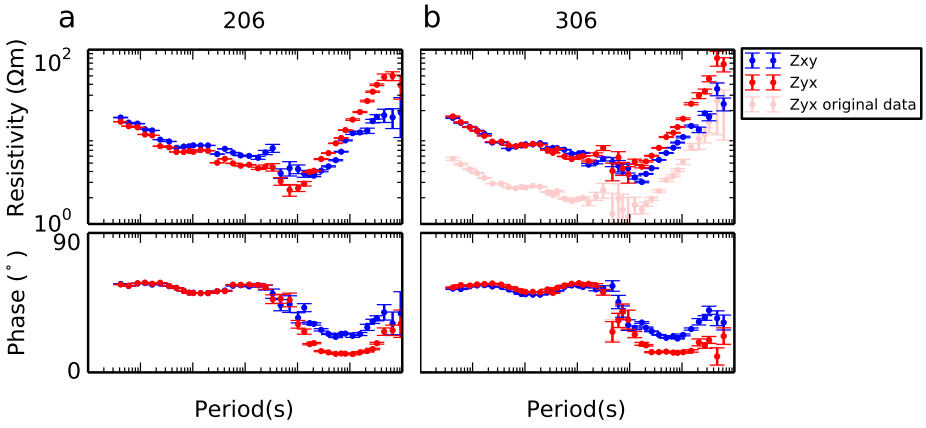

Figure 2.4: Resistivity and phase vs. period for two stations. (a) Station 206, where the Z_{xy} and Z_{yx} resistivities are different by less than our chosen threshold of 35 %. (b) Station 306 where the uncorrected Z_{xy} and Z_{yx} resistivities are different by more than 50 %. The Z_{xy} resistivity from Station 306 is closer to the median resistivity of the Z_{xy} and Z_{yx} components at Station 206 over the 1D part of the tensor, and therefore the Z_{yx} resistivity at Station 306 has been shifted to match the Z_{xy} component. Locations of Stations 206 and 306 are shown in Figure 2.1.

A second set of stations, with resistivities differing by between 35 and 50 %, were assumed to be affected to a small degree by static shift, and excluded from the process. Stations in the third group, with Z_{xy} and Z_{yx} resistivities differing by more than 50 %, were corrected in the following way. For each station, the nearest station unaffected by static shift was identified and the median resistivity over both modes calculated over the 0.001 to 0.1 s period range. This resistivity was then compared to each of the Z_{xy} and Z_{yx} component resistivities for the static shift-affected station. If the Z_{xy} component resistivity from the affected station was closest to this median resistivity value, the Z_{yx} component was shifted to match the Z_{xy} component resistivity over the 1D part of the impedance tensor. Conversely, if the Z_{yx} component was closer, the Z_{xy} component was shifted.

2.6 Unconstrained 1D anisotropic inversions

2.6.1 Method

As discussed in Section 2.4, the phase tensors from the Koroit dataset indicate the structure is 1D at periods less than 12.5 s. Phase splits occur at about 12.5 s but the induction vectors are small in magnitude up to periods of 50 to 100 s. Neither these nor the phase tensors vary considerably across the array. While the coast is located only 10 km away from the southernmost MT stations, the sea is shallow, reaching a water depth of 150 m at 75 km offshore, and we found the effects of the ocean to be minimal from 2D forward modelling tests. Therefore, we interpret the phase splits in the data as resulting, at least in part, from electrical anisotropy. We have undertaken 1D anisotropic modelling at each station in order to characterise the distribution and amount of anisotropy.

The inversion algorithm of Pek and Santos (2006) was used to generate smooth 1D anisotropic resistivity models at each station. The algorithm minimises the sum of the model structure, anisotropy, and data-model misfit, and returns the maximum and minimum horizontal resistivity and the anisotropy strike. For the structure penalty values we used the roughness penalty (Constable et al., 1987; Pek and Santos, 2006). For the anisotropy penalty we used the $\ell 2$-norm of the anisotropy. The MTpy software (Krieger and Peacock, 2014) was used to generate input files and visualise the outputs.

Error floors of 3 % were set for each of the off-diagonal impedence tensor elements. The Z_{xy} and Z_{yx} error values were then used, respectively, as absolute error floors for the Z_{xx} and Z_{yy} elements. Setting the error floors in this way has the effect of increasing the relative error on the diagonal components over the 1D part of the impedance tensor (periods of < 1 s), where these components are close to zero, allowing the inversion to model these components as zero without causing large misfits. At longer periods, where the diagonal components are more similar in magnitude to the off-diagonal components, the relative errors become smaller and the inversion is forced to match the diagonal components more closely.

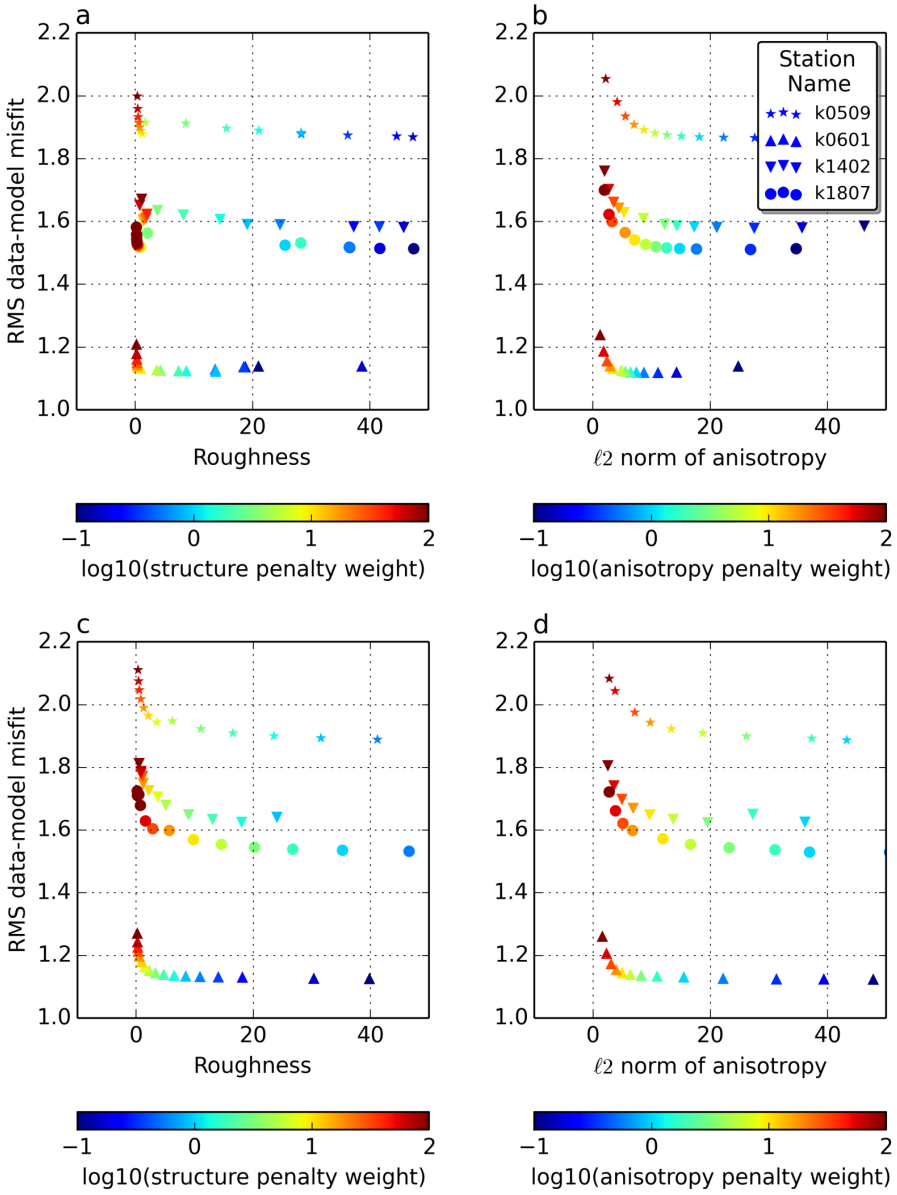

Figure 2.5: Data-model misfit vs. model roughness and data-model misfit vs. anisotropy for four stations, coloured by penalty weight. (a) Misfit vs roughness for an anisotropy penalty weight of 10^{-1}, (b) Misfit vs anisotropy for a roughness penalty weight of 10^{-1}, (c) Misfit vs roughness for an anisotropy penalty weight of $10^{0.75}$, (d) Misfit vs anisotropy for a roughness penalty weight of $10^{0.75}$. Station locations are shown in Figure 2.6.

The inversions were carried out at several different strike angles to test for any dependence on rotation angle. These tests showed that rotating the data to 45 ° from strike prior to inversion produces the best fits to the data and most consistent results between stations. Therefore, the inversions presented here were performed using the data rotated to 45 ° from strike.

In the inversions, penalty weights can be chosen for both the model roughness and the anisotropy, with higher penalty weights corresponding to smoother and less anisotropic models and (in general) poorer fits to the data, and lower weights corresponding to rougher and more anisotropic models (Pek and Santos, 2006). The aim in running the inversions is to find the optimal trade-off between data-model misfit and model roughness. Initial models were run over model structure and anisotropy penalty weights ranging, in log space, from 0.1 to 1000 for the structure penalty, and 0.1 to 100 for the anisotropy penalty, at each station. In order to select the optimal penalty weights, we followed the approach of Pek and Santos (2006) of plotting L-curves, or plots of data-model misfit vs roughness and anisotropy. Example L-curves are shown in Figure 2.5. The L-curves show misfit vs roughness penalty for two fixed anisotropy penalty weights (Figures 2.5a and c) and misfit vs anisotropy penalty for two fixed structure penalty weights (Figures 2.5b and d) at four stations. At each station, as the structure or anisotropy penalty weight is decreased, both anisotropy and roughness increase while the misfit decreases, with the slope becoming smaller at lower penalty weights. At low penalty weights (<1), the data-model misfit approaches the lowest possible value at each station but the models are highly anisotropic, very rough, or both. At high penalty weights, the models are smoother and less anisotropic, but the data-model misfit is high.

We selected the optimal models based on the L-curves together with comparison of the misfit values at each station compared to the lowest misfit achieved, and visual inspection of the inversion outputs. We have selected penalty weights of $10^{0.75} \approx 5.6$ for both roughness and anisotropy. These values correspond to the green-yellow colours on Figures 2.5b and d. With these penalty weights, the median data-model misfit is within 10 % of the minimum value achieved at all but one station, and within 15 % of the minimum value at all stations.

2.6.2 Results

Measured and modelled resistivity and phase, and measured induction vectors are shown for four stations in Figure 2.6. Also shown is a map of the root-mean-square (RMS) data-model misfit at each station, where the misfit is defined as the ratio of the difference between the data and the model response to the data error. In general, the fit is very good at periods less than 1 s, where the structure is 1D and isotropic. Slightly larger discrepancies between the data and the model begin to occur at periods greater than 1 s, although the fit is still good, with a median RMS value of 1.7 over the period range 1 to 100 s. The misfit increases slightly to 2.2 at periods greater than 100 s. The median RMS error across all periods is 1.7.

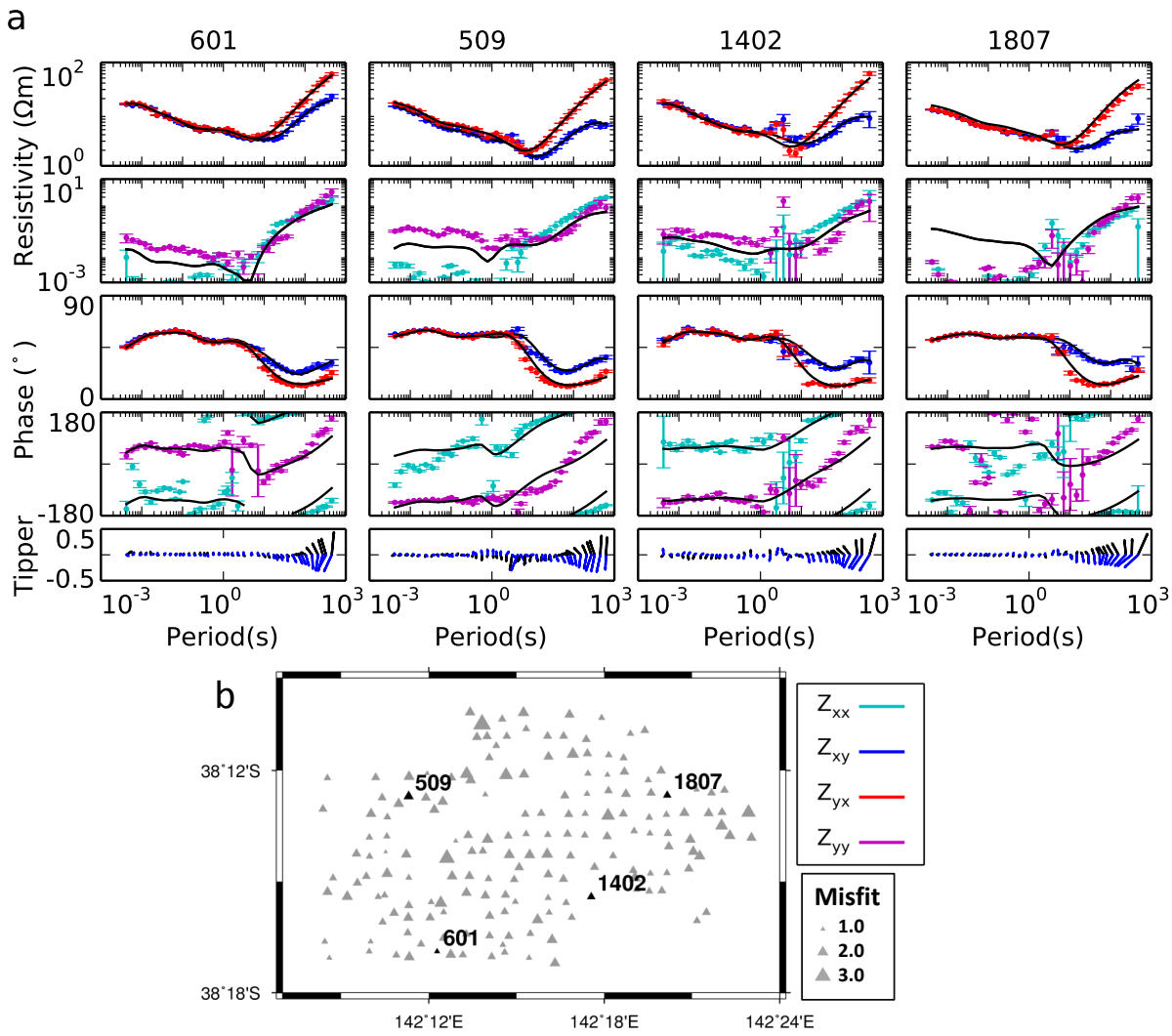

Figure 2.6: (a) Resistivity and phase vs. period at four stations, overlain by the model responses (black lines). Induction vectors (tipper), which were not used in the inversions, are also shown. Data are shown unrotated, with the model responses rotated back to the original data rotation angle for comparison with the data. The Z_{yx} phase values have had 180 ° added to enable comparison with the Z_{xy} phase values. (b) Median data-model misfit at each station, with station locations labelled. Symbol diameter is proportional to RMS misfit.

Two profiles containing examples of the 1D inversion models are shown in Figure 2.7. For comparison, the top depths of the Dilwyn Formation, Eumeralla Formation, Crayfish Group, and Basement are plotted as horizontal lines.

The inversions show similar characteristics in the top 8 km, with the upper 2 to 3 km being isotropic and conductive (1 to 10 Ωm). The strike angle of maximum conductivity is generally quite variable near the surface, but this stabilises below about 2 km at about 160 ° east of north. Deeper than 4 km, the models are in general resistive (approximately 1000 Ωm), although in many models an anisotropic layer (minimum and maximum resistivities equal to 1 and 100 Ωm) occurs at some point between 4

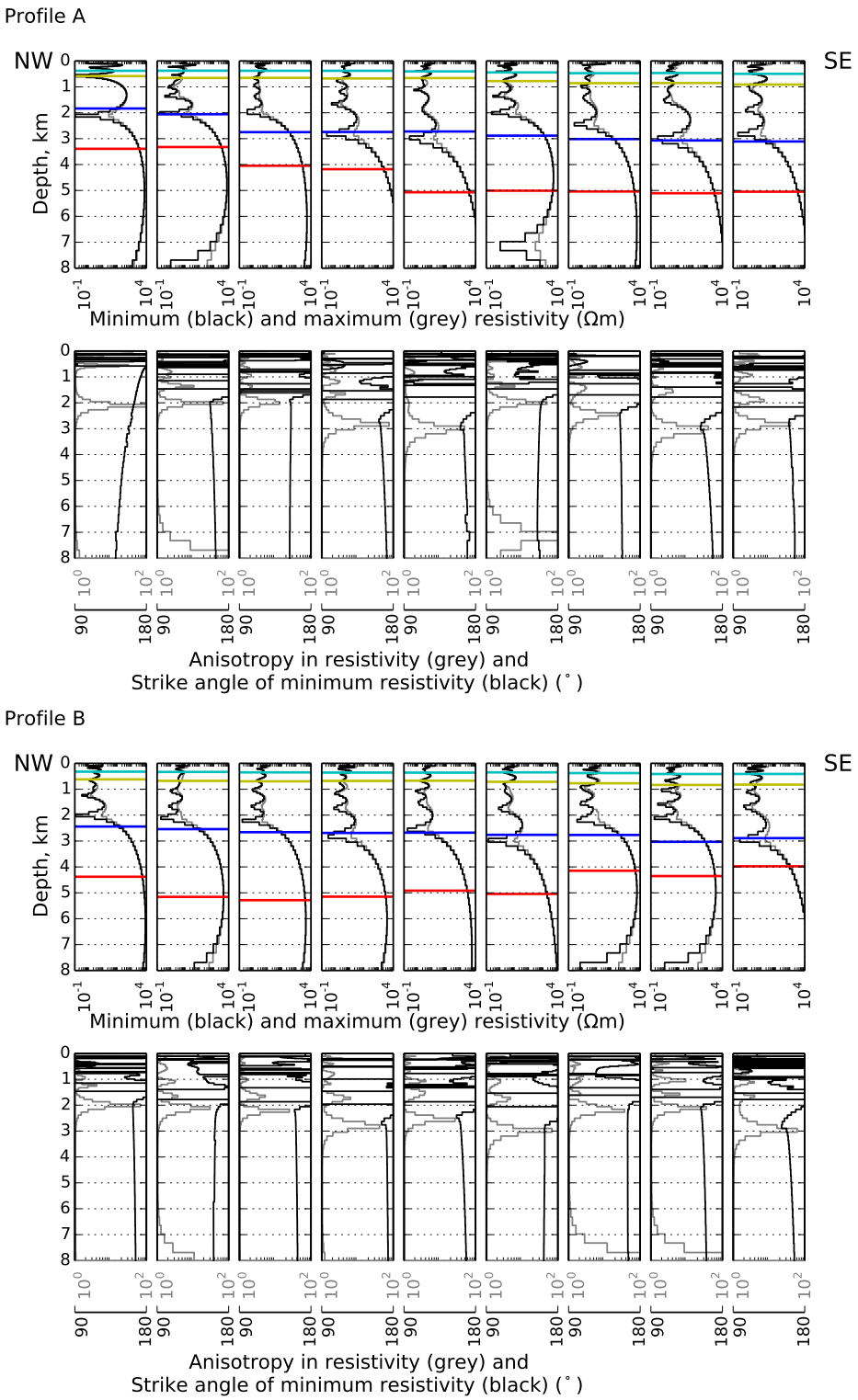

Figure 2.7: Diagram showing the minimum and maximum resistivity, anisotropy ratio and anisotropy strike from unconstrained 1D anisotropic inversions (Section 2.6) along two profiles. For comparison, the following stratigraphic horizons are shown as horizontal lines: top Dilwyn Formation (cyan), top Eumeralla Formation (yellow), top Crayfish Group (blue), and top Basement (red). Profile locations shown in Figure 2.1. Stratigraphic horizon interpretations from Hot Rock Ltd. (2009).

and 20 km depth. However a striking feature that occurs in almost every model is an anisotropic layer at a depth between 2 and 3 km. This feature is conductive (minimum and maximum resistivity of approximately 1 and 10 Ωm), and has a consistent anisotropy strike of about 160 °, approximately parallel with the induction vectors (Figure 2.2).

There is reasonable consistency in the depth and anisotropy of this layer between adjacent stations. The top of this layer corresponds approximately with the top of the Crayfish Group horizon at most stations. This suggests that the maximum anisotropy occurs within the upper part of the Crayfish Group. The low resistivity at this depth is consistent with low resistivities measured on core samples within the Pretty Hill Formation of the Crayfish Group (Alexander, 1992).

2.7 Constrained 1D anisotropic inversions

In order to investigate the sensitivity of the depth and characteristics of the anisotropy identified in Section 2.6.2, constrained 1D anisotropic inversions were performed at each station. The constraints were incorporated by providing an *a priori* model to the inversion.

Two sets of constrained inversions were performed, each incorporating anisotropy at different depths. In the *a priori* model for the first set of inversions, a 1 km thick anisotropic layer was put at the top of the Crayfish Group. This *a priori* model is similar to the results of the unconstrained inversions, the goal being to see if the consistency in the depth of the layer can be improved. In the *a priori* model for the second set of constrained inversions, a 1 km thick anisotropic layer was put at the top of basement.

2.7.1 Anisotropy within the Crayfish Group

The *a priori* model for the first set of constrained inversions consists of an upper, conductive isotropic section with resistivity ranging from 1.5 to 12 Ωm, determined from the well logs (Figure 2.8). This upper section is followed by a 1 km thick anisotropic layer (1 and 10 Ωm) with an anisotropy strike of 160 ° east of north, starting at the top of the Crayfish Group, followed by two more resistive, isotropic layers (30 then 1000 Ωm).

The inversion results are shown in Figure 2.9. The fit is very similar to the unconstrained inversions and the inversions also have a median RMS misfit of 1.7. At most stations, the inversions have closely followed the *a priori* model and placed the anisotropic layer immediately below the top of the Crayfish Group. At most stations this has resulted in a slight deepening of the anisotropic layer from the unconstrained inversions (Figure 2.7).

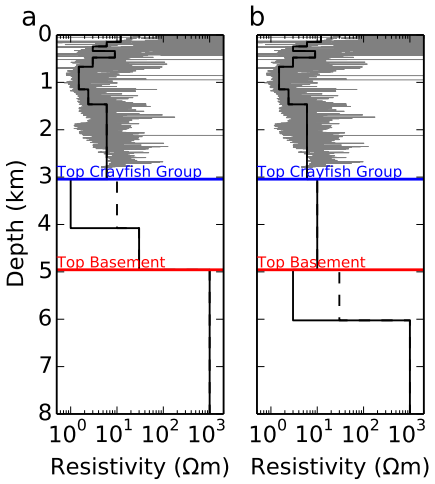

Figure 2.8: Diagram showing the *a priori* models used in the constrained inversions, (a) *a priori* model for first set of constrained inversions with anisotropy within the Crayfish Group, (b) *a priori* model for second set of constrained inversions with anisotropy within Basement. The top 1.5 km is the same for both sets of inversions and is based on the deep resistivity logs, which are shown for comparison in grey. Stratigraphic horizon interpretations from Hot Rock Ltd. (2009).

2.7.2 Anisotropy within basement

The *a priori* model for the second set of inversions was the same as for those in Section 2.7.1 except that an anisotropic layer was put at the top of Basement instead of within the sediments, and was slightly more resistive (3 and 30 Ωm) to reflect the slightly higher resistivities at this depth in the unconstrained inversions. The results are presented in Figure 2.10.

The median misfit is 1.7, the same as the misfit for both previous sets of inversions. However, while the inversion does follow the *a priori* model at most stations, it places an additional anisotropic layer at depths between 1.5 and 2.5 km, suggesting that, regardless of whether there is anisotropy within basement, at least part of the resistivity and phase splits in the data result from structures at around 2 km depth.

2.7.3 Comparison with well data

Four of the seven wells with resistivity logs in the Koroit region (Section 2.4.2) penetrate the Crayfish Group. The resistivity logs are presented with the nearest inversion result from the first set of constrained inversions (Section 2.7.1) in Figure 2.11.

There is a reasonable agreement between the well data and the inversion results, although there are discrepancies at some wells, particularly in Killara 1. As mentioned in Section 2.4, in three of the wells, there is a decrease in resistivity at the top of the Crayfish Group. However, the depth of this decrease does not exactly coincide with the drop in resistivity at the anisotropic layer in the corresponding inversions. This discrepancy may reflect an inability of the inversions to resolve in detail the shallow

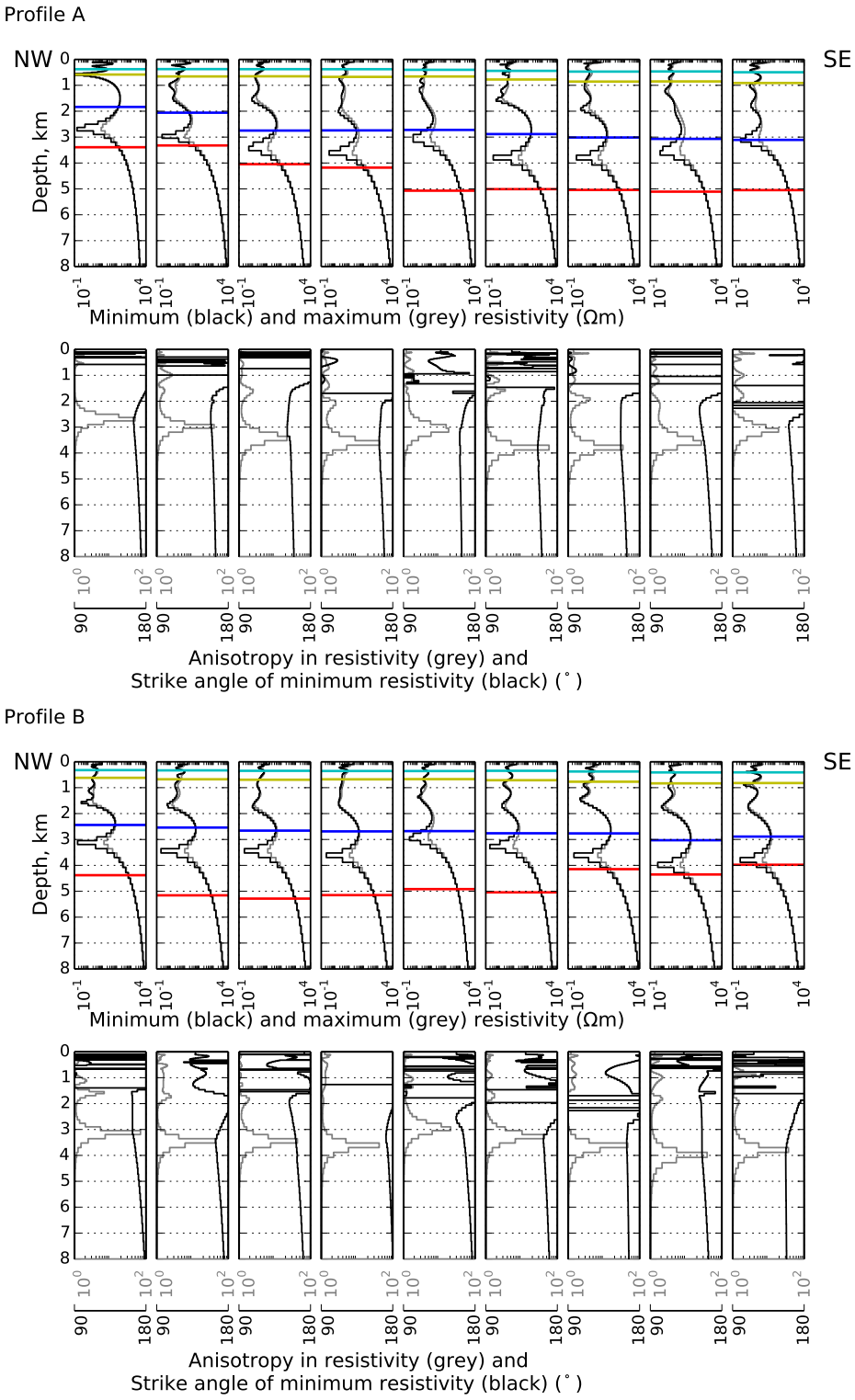

Figure 2.9: Diagram showing the minimum and maximum resistivity, anisotropy ratio and anisotropy strike from the first group of constrained 1D anisotropic inversions (Section 2.7.1; anisotropy within the Crayfish Group) along two profiles. The following stratigraphic horizons are shown as horizontal lines: top Dilwyn Formation (cyan), top Eumeralla Formation (yellow), top Crayfish Group (blue), and top Basement (red). Profile locations shown in Figure 2.1. Stratigraphic horizon interpretations from Hot Rock Ltd. (2009).

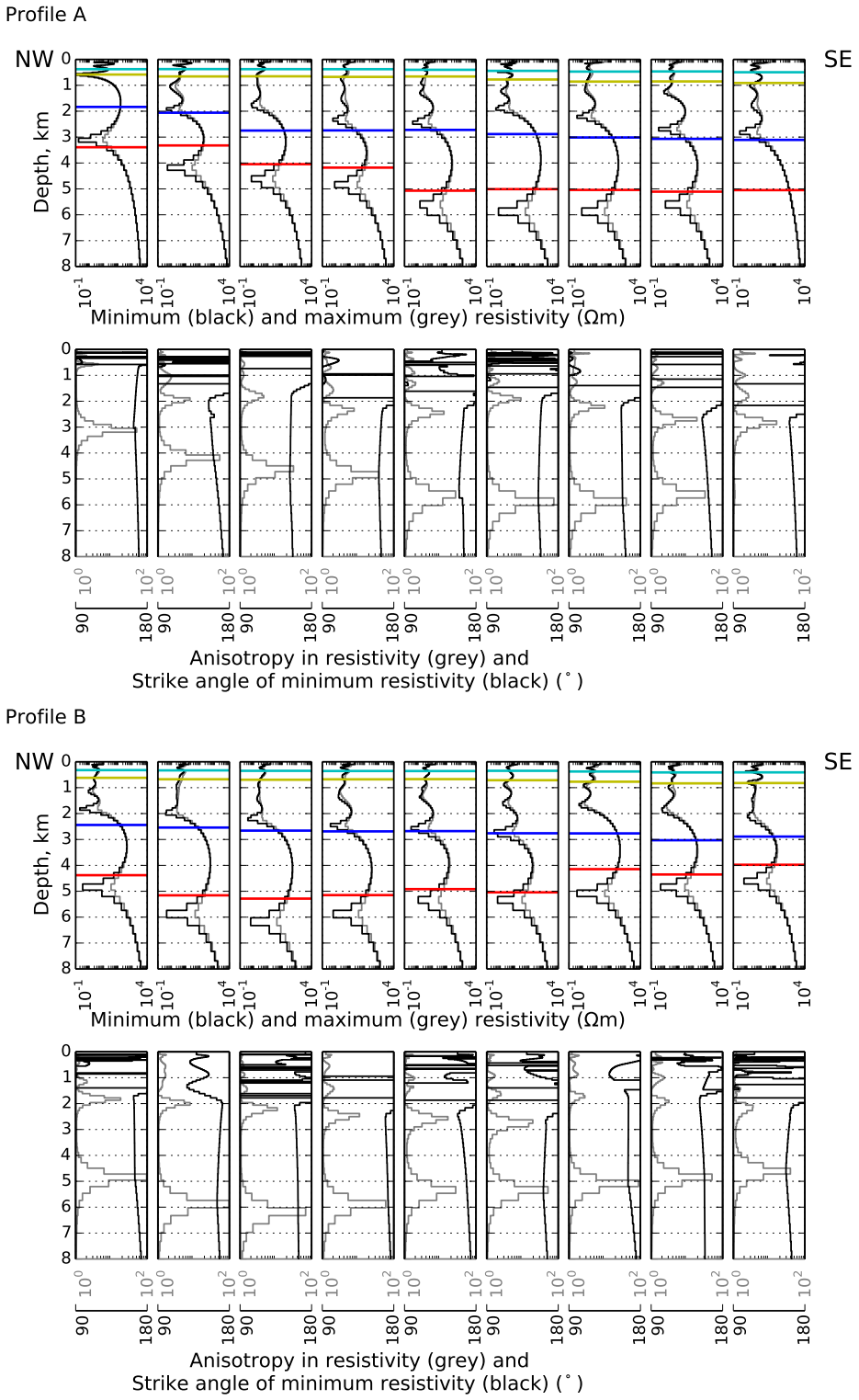

Figure 2.10: Diagram showing the minimum and maximum resistivity, anisotropy ratio and anisotropy strike from the second group of constrained 1D anisotropic inversions (Section 2.7.2; anisotropy within Basement) along two profiles. The following stratigraphic horizons are shown as horizontal lines: top Dilwyn Formation (cyan), top Eumeralla Formation (yellow), top Crayfish Group (blue), and top Basement (red). Profile locations shown in Figure 2.1. Stratigraphic horizon interpretations from Hot Rock Ltd. (2009).

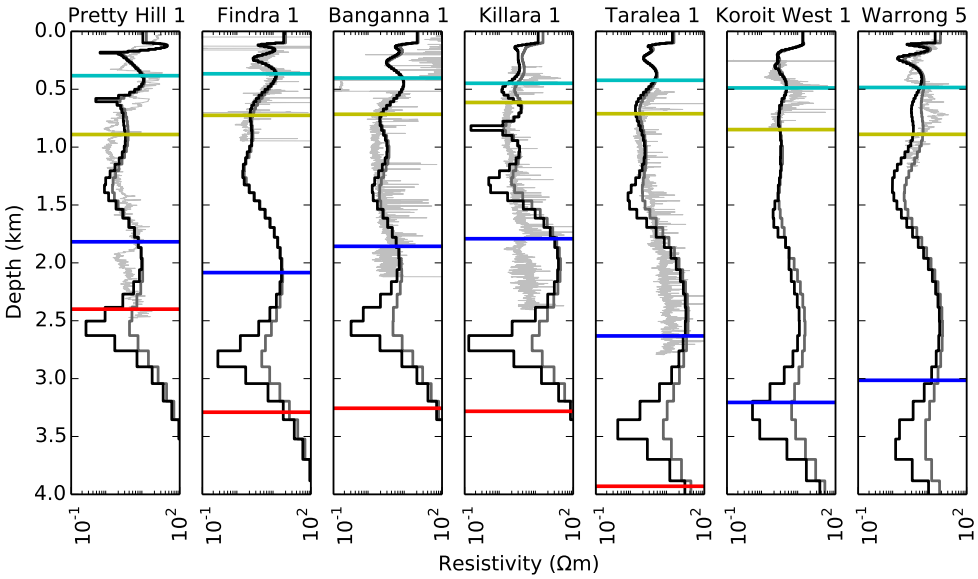

Figure 2.11: Diagram comparing deep resistivity logs (light grey) with minimum (black) and maximum (dark grey) resistivities obtained from the first set of constrained inversions (Section 2.7.1). Four stratigraphic horizons are also shown: top Dilwyn Formation (cyan), top Eumeralla Formation (yellow), top Crayfish Group (blue), and top Basement (red).

resistivity structure, or alternatively it may reflect the fact that, with the exception of Findra 1, the stations are located 500 m or more away from the wells and are therefore sampling different parts of the subsurface. Also, the total volume of rock sampled by MT becomes greater with depth, but with the well logs it stays the same. This may explain some of the discrepancies between the inversions and the well logs at greater depths.

2.7.4 Map representation of inversion results

An alternative way of visualising the inversions is as a map showing key characteristics of the inversion results. Figure 2.12a shows the depth and anisotropy value taken from each inversion at the point of maximum anisotropy within the sedimentary sequence, excluding the top 1 km, where the strike angle is extremely variable. The depth values have been gridded using linear interpolation and plotted as a contour map. The anisotropy values are plotted as bars with the length of the rectangle representing the magnitude of the anisotropy and the orientation representing the anisotropy strike. Figures 2.12b and c show the depths of the top of the Crayfish Group and the top Basement from interpretation of seismic reflection data.

The depth of maximum anisotropy varies across the area, and is generally located between the top of the Crayfish Group and Basement (Figures 2.12b and c). The point of maximum anisotropy is shallowest in the northwest (approximately 2.5 km) and

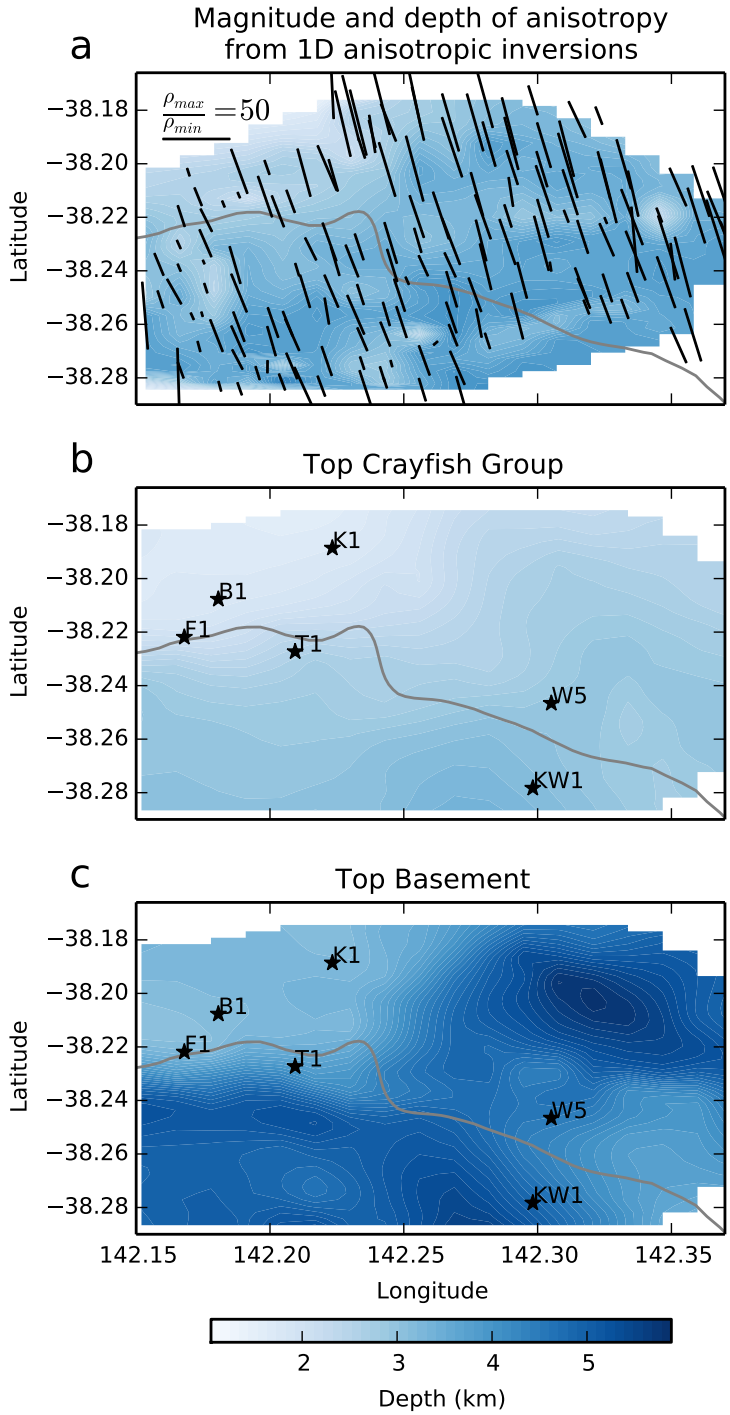

Figure 2.12: (a) Results of constrained inversions described in Section 2.7.1 displayed as a map. Colours represent depth of maximum anisotropy within the sedimentary sequence gridded using linear interpolation, bars represent the magnitude of anisotropy, ρ_{max}/ρ_{min}. Interpreted depth of (b) top Crayfish Group and (c) top Basement after Hot Rock Ltd. (2009). The Tyrendarra North Fault is shown in grey. Wells (black stars) are T1 = Taralea 1, F1 = Findra 1, KW1 = Koroit West 1, B1 = Banganna 1, K1 = Killara 1, W5 = Warrong 5.

deepest in the south and east (approximately 3.5 km). The magnitude of maximum anisotropy is also variable, increasing from approximately 10 in the southwest to around 30 in the northeast. In contrast, the anisotropy strike is very consistent at around 160 °.

2.8 Discussion

We have presented 1D anisotropic inversions of MT data collected from the Koroit region of the Otway Basin, Victoria. These inversions delineate a persistent anisotropic layer at approximately 2.5 to 3.5 km depth, with an anisotropy strike of about 160 °. However, while this interpretation produces a very good fit to the data, other interpretations (e.g., in terms of 2D structures) may be equally valid. In this section, we first discuss other evidence from the MT data and the regional geology to support a 1D anisotropic interpretation of the data. We then interpret the results in terms of fractures, permeability and the current stress field.

2.8.1 Evidence for anisotropy

Anisotropy in MT data can be indistinguishable from 2D isotropic structure based solely on the impedance tensor at an individual station. Induction vectors, phase tensors, and the regional geology can be examined to resolve this ambiguity.

Two major faults have been mapped in the Koroit region, the Tyrendarra North Fault and the Yarramyljup Fault (Figure 2.1, Vandenberg, 2000; Tassone, 2014). The Tyrendarra North Fault changes orientation at a longitude of approximately 142.25 °, from about 80 ° west of this point, to 120 ° further east (Figure 2.1). This fault does not align with the anisotropy strike, and furthermore there is no obvious response to it in either the induction vectors or the phase tensors (Figure 2.2). The Yarramyljup Fault, which strikes at approximately 170°, is mapped approximately 10 km west of the Koroit region (Figure 2.1, Vandenberg, 2000). While the orientation of this fault is consistent with the anisotropy strike, the induction vectors and the phase tensors do not appear to show any response to it. Consistent with this, MT data collected across the Yarramyljup Fault further north do not show any obvious conductivity anomaly associated with the fault itself, although there is a change in the phase tensors across the fault (Robertson et al., 2015).

The presence of an anisotropic layer is also consistent with the behaviour of the phase tensors. Heise et al. (2006) analysed the behaviour of phase tensors for different synthetic 1D anisotropic models. The case of an anisotropic layer embedded within an isotropic background was considered. The conductivity in the y direction (i.e., perpendicular to anisotropy strike) was set at a constant value of 1000 Ωm. An anistropic layer was created by reducing the conductivity in the x direction (parallel to anisotropy strike) to 20 Ωm from 15 to 20 km depth. Because phase tensors respond to lateral or vertical changes in resistivity, not absolute values, the Z_{yx} phase for this model does not change, remaining at 45 °. The Z_{xy} phase responds, in turn, to the changes in x

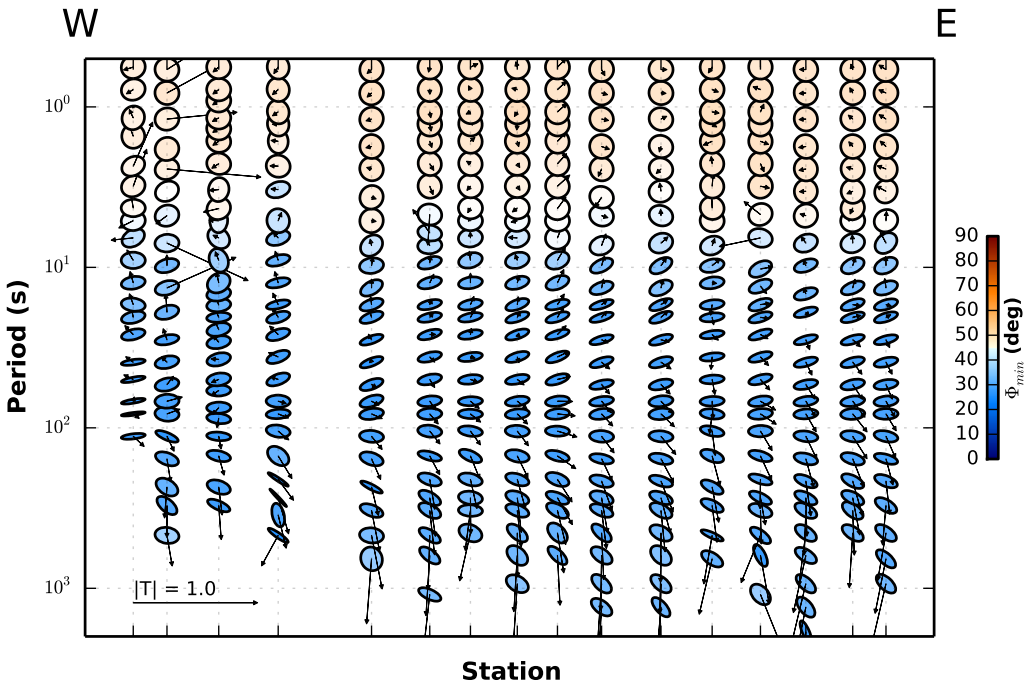

Figure 2.13: East-northeast oriented pseudosection showing phase tensor ellipses and real induction vectors plotted using the Parkinson convention (Parkinson, 1959). Ellipses are coloured by the minimum phase, Φ_{min}. Profile location shown in Figure 2.1.

direction resistivity at the top and bottom boundary of the layer, first increasing to greater than 45 °, then dropping to less than 45 ° (Heise et al., 2006). The result is that, at periods corresponding to the top of the layer, the major axis of the ellipse is perpendicular to the anisotropy strike, and then at periods corresponding to the bottom of the layer, the major axis becomes oriented parallel to the anisotropy strike.

Figure 2.13 shows an approximately east-west pseudosection of phase tensors and induction vectors for the Koroit dataset. The phase tensors show a similar response to the synthetic example of Heise et al. (2006). The major axes of the ellipses are oriented perpendicular to the anisotropy strike at periods of about 10 to 50 s, but by periods of about 200 s, the ellipses have changed orientation to about 135 °, approaching the anisotropy strike.

A final observation that supports a 1D anisotropic interpretation is the orientation of the induction vectors compared to the anisotropy strike. The anisotropy strike defined in Section 2.7 is approximately parallel to many of the induction vectors at 12.5 s (Section 2.4), while in a 2D isotropic case, the induction vectors should be oriented perpendicular to geoelectric strike. This suggests that the phase splits are a result of anisotropy, not larger scale heterogeneity.

2.8.2 Fractures, permeability and the current stress field

Electrical anisotropy in the upper crust often results from the mixing of two materials with different electrical conductivities (Wannamaker, 2005). Given the shallow sedimentary setting of this dataset, one interpretation of the anisotropy delineated in Sections 2.6 and 2.7 is fractures filled with an electrically conductive material. Because many fractures in the crust are smaller than the resolution of MT at 2.5 to 3.5 km depth, they are unlikely to be individually resolved, but their presence could be observed as bulk anisotropy.

Likely fracture fill materials in a shallow sedimentary environment include clay, fluids, or a combination of both. In the Otway Basin, the fluids at about 2 km depth are saline (e.g., Bain, 1962; Buckingham, 1992), and therefore electrically conductive. Alternatively, Bailey et al. (2014) noted that the electrically conductive mineral siderite was present in some (but not all) fractures within core samples from the Penola Trough in the western Otway Basin, resulting in them appearing as electrically conductive on image logs. It is possible that siderite is also present in some fractures in the Koroit region. However, structural and stress field data from the Otway Basin are consistent with at least some of the fractures being fluid-filled, as discussed below.

The presence of fluid-filled fractures is consistent with permeability data from the Otway Basin. Permeability data from wells in the Otway Basin both within the Koroit region and elsewhere show that the Crayfish Group is highly permeable (e.g., Alexander, 1992; Morton et al., 2002; Geoscience Australia, 2014). Likewise, in Section 2.7, the point of maximum anisotropy in the sedimentary part of the sequence is within the Crayfish Group and is the most electrically conductive depth interval. This would be expected if the anisotropy is due to fluid-filled fractures: if a medium has connected pathways for fluid flow and the fluid is electrically conductive, the pathways will also be open for electrical current flow.

Dip-meter data in the Killara 1 well were analysed by 3D-Geo (2009). Above the Crayfish Group, the dip is very consistent, likely reflecting the bedding plane dip (3D-Geo, 2009). However, within the Crayfish Group the dip becomes highly variable. 3D-Geo (2009) interpreted this to result from fracturing within the Crayfish Group disturbing the measured dip.

An interpretation of the MT inversion results in terms of fluid-filled fractures is also consistent with the orientation and nature of mapped faults and the current stress field in the Otway Basin. Bahr (1997) showed, by modelling the electrical connectivity of random resistor networks, that networks are more likely to exhibit strong anisotropy in the vicinity of their percolation threshold. In a natural fault network, the fractures that are most optimally oriented for reactivation in a given stress field are likely to be closest to their percolation threshold, with the direction of maximum electrical (and hydraulic) conductivity in the direction of these fractures. Tassone (2014) determined the most likely current stress regime in the central Otway Basin to be strike slip, i.e, the maximum and minimum stress σ_1 and σ_3 are both horizontal. The maximum horizontal stress direction was determined to be approximately 135 °, consistent with previous studies (e.g., Hillis et al., 1995; Nelson et al., 2006).

Bailey et al. (2014) analysed the conditions for reactivation of existing faults in the Penola Trough, western Otway Basin, South Australia. The stress field in the Penola Trough is strike-slip with σ_1 oriented at about 125 °. The absolute stress magnitudes are similar to the central Otway Basin (Nelson et al., 2006; Bailey et al., 2014; Tassone, 2014) where the Koroit MT data are located. Bailey et al. (2014) generated fracture reactivation susceptibility plots for this stress field for a depth of 3 km. These plots showed that in a strike-slip regime faults dipping at greater than about 50 ° and striking between 90 and 165 ° were most favourably oriented for reactivation. In the central Otway Basin, σ_1 is oriented at 135 °, therefore favourable orientations should fall within the range 100 to 175 °.

As discussed in Section 2.8.1, there are two major faults in the Koroit region, the Tyrendarra North Fault, and the Yarramyljup Fault (Figure 2.1). The Tyrendarra North Fault is oriented at 120 ° in the east of the study area, and is therefore favourably oriented for reactivation, but not in the west where it is oriented at 80 °. The Yarramyljup Fault is oriented at about 170 ° and is therefore favourably oriented for reactivation. While the Yarramyljup Fault itself does not appear to influence the MT data (Section 2.8.1), the basement structural fabric east of this fault (i.e., in the Koroit region) is believed to also follow this orientation (Vandenberg, 2000). North-northwest striking structures have also been mapped using 2D seismic data in the Koroit area (3D-Geo, 2009).

North and northeast of Koroit, Clark et al. (2011) identified several large neotectonic fault scarp like features (10 to 100 km long) oriented at approximately 160 to 180 °. Tassone (2014) noted that many of these features coincide with basement lineaments, and suggested that basement structures are the primary control on neotectonic faulting. While no neotectonic features have been mapped within the Koroit region, the available information on the structure and current stress field suggests that north-northwest oriented structures are likely to be present and are the most favourably oriented for reactivation.

If the results of 1D inversions are interpreted in terms of fluid-filled fractures, oriented favourably for reactivation in the current stress field, the results of our 1D anisotropic inversions suggest that structural permeability is greatest in a north-northwest – south-southeast direction. They also suggest that either the fracturing is most intense, and/or fractures are most open, in the northeast, decreasing to the southwest, and that high structural permeabilities occur at a deeper level in the south and east than in the northwest of the Koroit region.

2.9 Conclusion

Using 1D anisotropic inversions, we have delineated a persistent anisotropic layer located at 2.5 to 3.5 km depth in sediments of the central Otway Basin, Victoria. This layer can be interpreted in terms of fluid-filled fractures oriented favourably for reactivation in the current stress field. The anisotropy and depth of this layer varies spatially: it is deeper in the south and east of the Koroit region than in the northwest, and

anisotropy becomes stronger from east to west. In unconstrained inversions, the depth of this layer is approximately coincident with the upper part of the Crayfish Group, but the depth fluctuates in places. By using an *a priori* model we have improved the lateral consistency of the depth of this layer with no change in the data-model misfit.

An interpretation of the anisotropy in terms of fluid-filled fractures is consistent with borehole permeability measurements, which show high permeabilities occur in the Crayfish Group and a dip-meter log in Killara 1, which suggests that the Crayfish Group is more fractured than shallower stratigraphic units. This interpretation is also consistent with stress field and structural data from the surrounding region, which suggests that there are north-northwest striking faults in the Koroit region, and this orientation is favourable for reactivation in the current stress field.

CHAPTER

THREE

THE RESISTIVITY STRUCTURE OF THE PENOLA TROUGH, OTWAY BASIN FROM MAGNETOTELLURIC DATA

Alison Kirkby[1,2], Graham Heinson[1], and Simon Holford[3]

[1] Electrical Earth Imaging Group, School of Physical Sciences, University of Adelaide, Adelaide, SA 5000, Australia
[2] Geoscience Australia, Canberra, ACT 2601, Australia
[3] Australian School of Petroleum, University of Adelaide, Adelaide, SA 5000, Australia

Accepted on August 15th, 2016 as:
Kirkby, A.L., Heinson, G., and Holford, S. The resistivity structure of the Penola Trough, Otway Basin, from magnetotelluric data. Australian Journal of Earth Sciences

Statement of Authorship

Title of Paper	The resistivity structure of the Penola Trough, Otway Basin from magnetotelluric data
Publication Status	☐ Published ☑ Accepted for Publication ☐ Submitted for Publication ☐ Unpublished and Unsubmitted work written in manuscript style
Publication Details	Kirkby, A.L., Heinson, G., and Holford, S. The resistivity structure of the Penola Trough, Otway Basin from magnetotelluric data. Australian Journal of Earth Sciences.

Principal Author

Name of Principal Author (Candidate)	Alison Kirkby
Contribution to the Paper	Analysed and modelled data, wrote the manuscript
Overall percentage (%)	90%
Certification:	This paper reports on original research I conducted during the period of my Higher Degree by Research candidature and is not subject to any obligations or contractual agreements with a third party that would constrain its inclusion in this thesis. I am the primary author of this paper.
Signature	Date 10/8/16

Co-Author Contributions

By signing the Statement of Authorship, each author certifies that:

i. the candidate's stated contribution to the publication is accurate (as detailed above);

ii. permission is granted for the candidate in include the publication in the thesis; and

iii. the sum of all co-author contributions is equal to 100% less the candidate's stated contribution.

Name of Co-Author	Graham Heinson
Contribution to the Paper	Provided supervision of work, aided in MT data interpretation and critical analysis
Signature	Date 8TH AUG 2016

Name of Co-Author	Simon Holford
Contribution to the Paper	Aided in seismic data interpretation, contributed to geological interpretation and manuscript evaluation
Signature	Date 10/8/16

SUMMARY

We present inversion results for a 100 site, broadband magnetotelluric (MT) survey in the Penola Trough, Otway Basin, South Australia. The Penola Trough is host to several petroleum reservoirs and has more recently been a target for unconventional geothermal exploration. We present two interpretations of the MT data. A 1D anisotropic interpretation, where anisotropy is determined within the Otway Basin sequence and basement in the northeast Penola Trough, fits the impedance tensor well. However, the anisotropy strike is inconsistent with the known orientation of electrically conductive fractures in the Penola Trough. On the other hand, a 3D interpretation, which incorporates lateral variations in resistivity, requires no anisotropy yet it matches the data equally well. Both the 1D and the 3D inversions resolve several layers within the Otway Basin sequence, which correspond to stratigraphic units defined in wells and in the coincident HaselgroveBalnaves 3D seismic survey. These include the Eumeralla and Dilwyn Formations, which are poorly resolved in the seismic data. The basin architecture that is defined in the 3D inversion, in particular the depth to basement, is consistent with previous interpretations based on seismic reflection data that show that the Otway Basin thins in the northeast Penola Trough. This does not occur in the anisotropic model. We therefore conclude the subsurface resistivity appears to be isotropic in the Penola Trough. This contrasts with the anisotropic resistivity structure determined in a previous study in the Koroit region, eastern Otway Basin. The difference in the MT responses between the two regions is supported by resistivity and permeability information from well logs and may reflect differences in the orientation of subsurface fractures, or differences in the present day stress field, between the two regions.

3.1 Introduction

The seismic reflection method is one of the most widely used techniques for mapping sedimentary basin structure, as it can precisely locate structural boundaries. It is also sensitive to changes in physical properties that affect the acoustic velocity, such as porosity (e.g. Pramanik et al., 2004). In addition to mapping the stratigraphy, 3D seismic reflection data can be used to map fractures and faults through the calculation of seismic attributes (e.g. Backé et al., 2011; Bailey et al., 2014). However, seismic reflection data provide little information on the nature of the fracture fill material and its connectedness. Increasingly, it is being recognised that the MT method may provide such information and thus complement seismic reflection data and interpretations (e.g. Jones, 1987; MacGregor et al., 2001).

The magnetotelluric (MT) method is less routinely applied to exploration of sedimentary basins as it cannot achieve the level of detail possible with seismic reflection. How-

ever, recently MT data have been collected over some Australian sedimentary basins to assist with unconventional geothermal exploration (e.g. Peacock, 2012; Kirkby et al., 2015; Didana, 2016). The data show similar characteristics in these different areas. At periods less than about 1 – 10 s (~3 km or less), they are predominantly 1D and generally show decreasing apparent resistivity with depth, reflecting increasing temperature, and often, increasing salinity. By 10 – 20 s, the apparent resistivity begins to increase again, responding to reduced porosity. The data sometimes show phase splits, which have been interpreted in terms of 2D or 3D basin structure (e.g. Peacock, 2012) or alternatively, anisotropy (e.g. Kirkby et al., 2015). However, in other areas (e.g., the Cooper Basin; Didana, 2016), the geoelectric structure is close to 1D at periods up to 100 s.

In the eastern Otway Basin, phase splits at periods >10 s were interpreted as resulting from macro-scale resistivity anisotropy due to preferentially aligned fractures and faults (Kirkby et al., 2015). The dominant orientation of the minimum resistivity axis, north-northwest, was in agreement with mapped structures in the area, including the Yarrumyljup Fault, neotectonic features mapped 100 km to the northeast (Clark et al. 2011), and the basement fabric (Vandenberg, 2000). In the present stress field, faults with this orientation are oriented favourably for reactivation (Tassone, 2014; Bailey et al., 2014; Kirkby et al., 2015).

The Haselgove – Balnaves 3D seismic survey has been used to map the structure of the Penola Trough, western Otway Basin (Boult et al., 2002a,b; Lyon et al., 2005a,b; Bailey et al., 2014). In addition to defining the basin-scale structure, Bailey et al. (2014) used the seismic data to map fractures on scales smaller than seismic amplitude resolution through the calculation of seismic attributes. Image logs were used to map the orientation of electrically conductive fractures in wells. Fractures on all scales had consistent orientations following dominant east – west and northwest – southeast trends. Both these trends are favourable orientations for reactivation in the present day stress field (Bailey et al., 2014).

We interpret new MT data collected in the Penola Trough to coincide with the Haselgrove Balnaves 3D seismic survey, where well image logs and seismic data indicate the presence of electrically conductive fractures. There are very few studies that have compared terrestrial 3D reflection seismic and MT data, particularly in relation to fracture detection in sedimentary basins, and so this study provides an opportunity to evaluate the merits of MT in elucidating basin geometry and structure. Given that MT data are relatively inexpensive to collect, the MT method may have considerable potential in frontier, poorly explored regions. We present two interpretations of the MT data. The first follows the method of Kirkby et al. (2015) by incorporating anisotropy within the Otway Basin sequence. The second isotropic interpretation incorporates lateral variations in conductivity. The results are compared to seismic interpretations and well logs to determine the resistivity characteristics of the Otway Basin in this area.

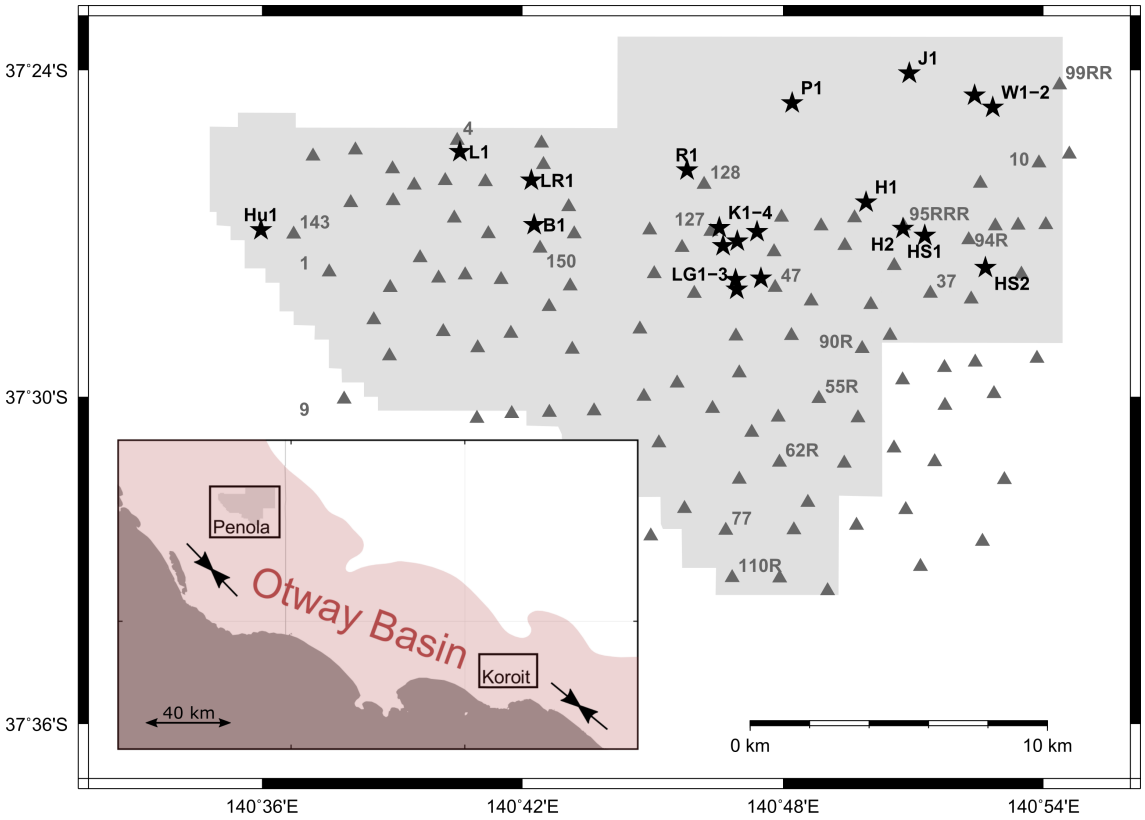

Figure 3.1: Map showing key locations for this study. Main map: Haselgrove–Balnaves 3D seismic survey (light grey), MT station locations (dark grey triangles) with stations discussed in the paper labelled, wells (black stars); Hu1 = Hungerford 1, L1 = Laira 1, LR1 = Limestone Ridge 1, B1 = Balnaves 1, R1 = Redman 1, K1-4 = Katnook 1-4, LG1-3 = Ladbroke Grove 1-3, P1 = Pyrus 1, J1 = Jolly 1, W1-2 = Wynn 1-2, H1 = Haselgrove 1, H2 = Haselgrove 2, HS1 = Haselgrove South 1, HS2 = Haselgrove South 2. Inset: The location of the Koroit and Penola surveys, Otway Basin (pink) including the offshore portion (grey with pink overlay). Black arrows indicate maximum horizontal stress.

3.2 The Otway Basin

3.2.1 Tectonics and structure

The broadly northwest trending Otway Basin covers parts of southern Victoria, South Australia and Tasmania, and extends offshore (Figure 3.1). The basin developed as a result of Jurassic to Cretaceous rifting of the Australian continent from Antarctica (Perincek and Cockshell, 1995). Sedimentation began in the Late Jurassic, with the deposition of the Casterton Formation, followed by the Crayfish Group in the Berriasian to Barremian (Krassay et al., 2004). Deposition of the Crayfish Group was followed by a period of uplift, tilting and erosion in the mid-Cretaceous, leaving an unconformity between the Crayfish Group and the overlying sediments (Jensen-Schmidt et al., 2002). Deposition of the Crayfish Group was concentrated in a series of west to northwest trending depocentres which include the Penola Trough, a northwest –

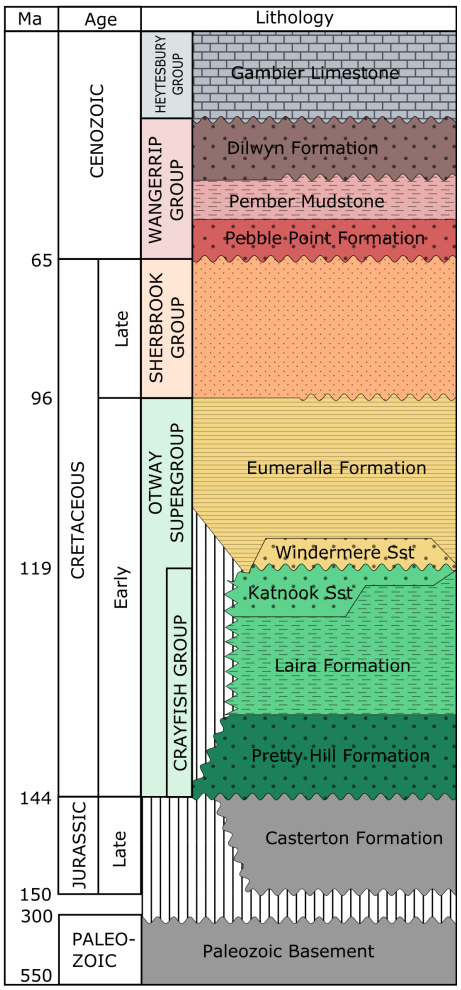

Figure 3.2: Otway Basin stratigraphy in the Penola Trough showing the stratigraphic units discussed in this paper and their ages, modified after Boult (2002).

southeast trending half graben in the western Otway Basin (Perincek and Cockshell, 1995; Jensen-Schmidt et al., 2002).

3.2.2 Penola Trough stratigraphy

In South Australia, the Crayfish Group has been divided into the Pretty Hill Formation, and the overlying Laira Formation and Katnook Sandstone (Figure 3.2, Boult et al., 2002b). The Pretty Hill Formation and Katnook Sandstone are important reservoir formations due to their high porosity and permeability (Morton et al., 2002). Both consist primarily of sandstone deposited in braided fluvial environments. They are separated by the low permeability Laira Formation, which comprises mainly siltstone and claystone (Boult et al., 2002b). The thickness of the Crayfish Group ranges from 2 – 5 km in the Penola Trough, and is strongly fault controlled due to sedimentation being concentrated in depocentres during a period of active rifting (Jensen-Schmidt et al., 2002).

Overlying the Crayfish Group units is the Eumeralla Formation, which consists primarily of claystone and other fine-grained floodplain sediments (Figure 3.2, Jensen-Schmidt et al., 2002). The Eumeralla Formation is 0.7 – 1.3 km thick based on wells that intersect it (Figure 3.7). The thickness and facies within the Eumeralla Formation are less diverse than the Crayfish Group and are not strongly structurally controlled (Boult et al., 2002b). The Sherbrook Group unconformably overlies the Eumeralla Formation. It is a post-rift sequence that was deposited during continental breakup between the Australian and Antarctic plate, which contains mainly lacustrine to deltaic units (Boult et al., 2002b; Jensen-Schmidt et al., 2002).

The stratigraphic units overlying the Sherbrook Group are formally part of the Gambier Basin in South Australia (Figure 3.2, Boult et al., 2002b). In the Penola Trough, these include the Wangerrip Group, which contains the Pebble Point Formation, the Pember Mudstone, and the Dilwyn Formation, which, in the Penola Trough, comprises primarily clean sandstone (Boult et al., 2002b). Overlying these units in the Penola Trough area is the Gambier Limestone (Boult et al., 2002b).

3.3 The magnetotelluric method

The MT method measures time variations in orthogonal components of the Earth's electrical (**E**) and magnetic (**B**) fields (Tikhonov, 1950; Cagniard, 1953). The impedance tensor **Z** is related to the horizontal components of the **E** and **B** fields through the relationship $\mathbf{E} = \mathbf{ZB}$.

Electromagnetic waves diffuse as they pass through the Earth with the depth of penetration related to the period of the inducing magnetic field. The electromagnetic skin depth d is given by $d = \sqrt{T\rho_{app}/\pi\mu_0} \approx 500\sqrt{T\rho_{app}}$, where μ_0 is the magnetic permeability, T is the period, and ρ_{app} is the apparent resistivity, or resistivity of an equivalent uniform half-space. The apparent resistivity is related to **Z** through

$$\rho_{app,\ ij} = \frac{T}{2\pi\mu_0}|Z_{ij}|^2 \tag{3.1}$$

where Z_{ij} represents the elements of the impedence tensor **Z**.

The MT phase tensor Φ is defined as $\mathbf{\Phi} = Re(\mathbf{Z})^{-1}Im(\mathbf{Z})$ and can be depicted as an ellipse (Bibby, 1986; Caldwell et al., 2004). If the geoelectric structure is 1D, the ellipse is a circle. If it is 2D (or 1D with anisotropy, where anisotropy varies with depth) the orientation of the major axis of the ellipse is either parallel or perpendicular to the geoelectric strike (Bibby, 1986; Caldwell et al., 2004).

3.3.1 Resistivity anisotropy and heterogeneity in the upper crust

Fractures spaced less than 1 to 2 km apart are unlikely to be individually resolved by MT at depths greater than a few kilometres. However, if the fractures are filled with an electrically conductive material they may reduce the conductivity in one direction

(Wannamaker, 2005). In this case, the subsurface may appear anisotropic, not from anisotropy in the rocks themselves but on a larger scale (macro-anisotropy) as a result of fractures and faults.

Resistivity anisotropy can be indistinguishable from 2D and 3D structure based on the impedance tensor alone (e.g. Heise et al., 2006). Heise et al. (2006) showed that identical responses can be produced near the boundary between a buried resistive and conductive body, and an anisotropic half space beneath an isotropic layer. In order to differentiate between them it is often necessary to exclude one based on other data, such as induction vectors, arrays of MT sites, or other types of data (Martí, 2014).

3.4 Data

3.4.1 Magnetotelluric data

Magnetotelluric data were collected at 100 sites within the Penola Trough, Otway Basin, for this study. The data were collected by Quantec Geoscience, over a period range of 0.004 to 1000 s. Sites were collected on a grid with an average spacing of 1.5 – 2 km.

Data are presented as phase tensor ellipses for a period of 12 s and as resistivity and phase as a function of period for four representative stations (Figure 3.3). For comparison, the Koroit data are shown in Figure 3.4. From periods of 0.004 to 10 s, the Z_{XY} and Z_{YX} apparent resistivity and phase values are almost the same, indicating 1D geoelectric structure. Likewise, the induction vectors at 1 s have a magnitude < 0.1 in most areas, indicating little lateral variation in conductivity.

The notable exception to this is a northeast striking corridor down the centre of the survey (Figure 3.3). Here, the induction vectors appear to be sensitive to a 275 kV overhead power transmission line. The magnitude of the induction vectors shows a clear relationship with proximity to the line, with stations within about 2 km of the transmission line most strongly affected. The phase tensors, on the other hand, do not appear to be strongly affected by the power line, indicating that the effect is mostly in the vertical magnetic field, but not in the horizontal electric fields.

At a period of 10 to 20 s, the Z_{XY} and Z_{YX} apparent resistivity and phase values split, particularly in the northeast corner, indicating some 2D or 3D structure and/or anisotropy. Geoelectric strike varies across the Penola Trough; in the west, ellipses indicate a strike of either 0 or 90° east of north which is consistent with the strike of 90° mapped in the 3D seismic data. In the east, the long axes of the ellipses rotate to an angle of around 135° east of north. Likewise, major structures in this area strike at around 135° (e.g. Boult et al., 2002a; Lyon et al., 2005a,b; Bailey et al., 2014).

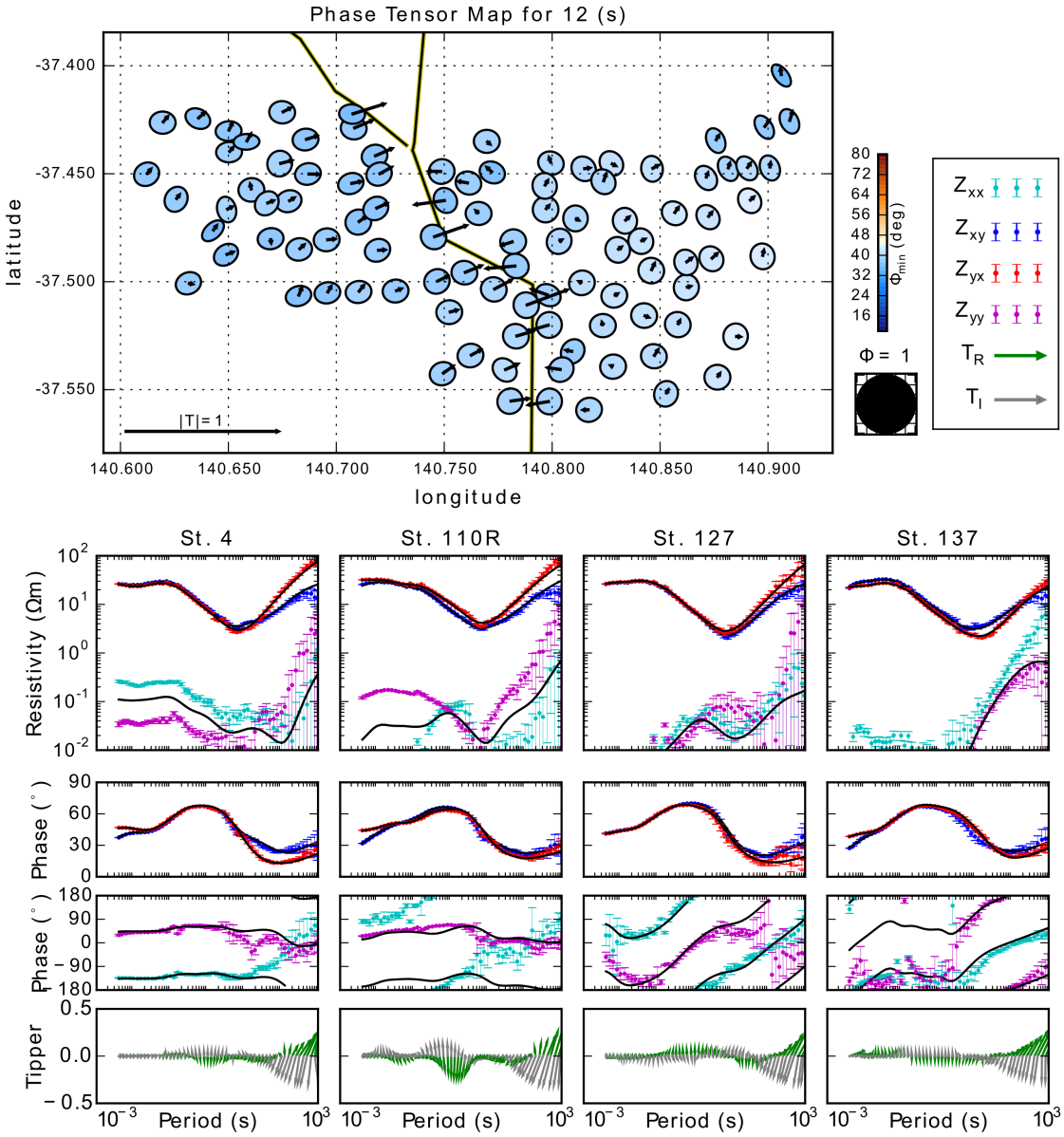

Figure 3.3: Magnetotelluric data from the Penola Trough shown as phase tensor ellipses and all components of resistivity, phase and tipper as a function of period for four example stations. Phase tensor ellipses shown with real induction vectors (plotted using the Parkinson convention) at a period of 12 s, coloured by the minimum phase Φ_{min}. High voltage power lines shown as a yellow and black line. The Z_{YX} phase angles in the examples have had 180° added to put them in the same quadrant as the Z_{XY} phases. Responses from the 1D anisotropic inversion results shown in black. Station locations shown in Figure 3.1.

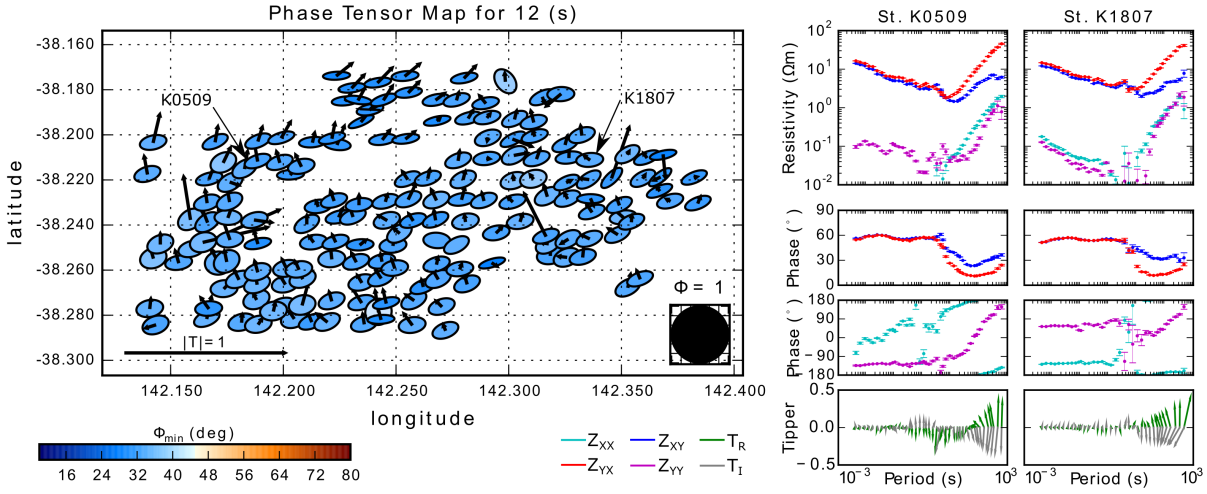

Figure 3.4: Magnetotelluric data from the Koroit region of the Otway Basin shown as phase tensor ellipses and induction vectors (plotted using the Parkinson convention) at a period of 12 s, coloured by the minimum phase Φ_{min}, and all components of resistivity, phase and tipper as a function of period for two example stations.

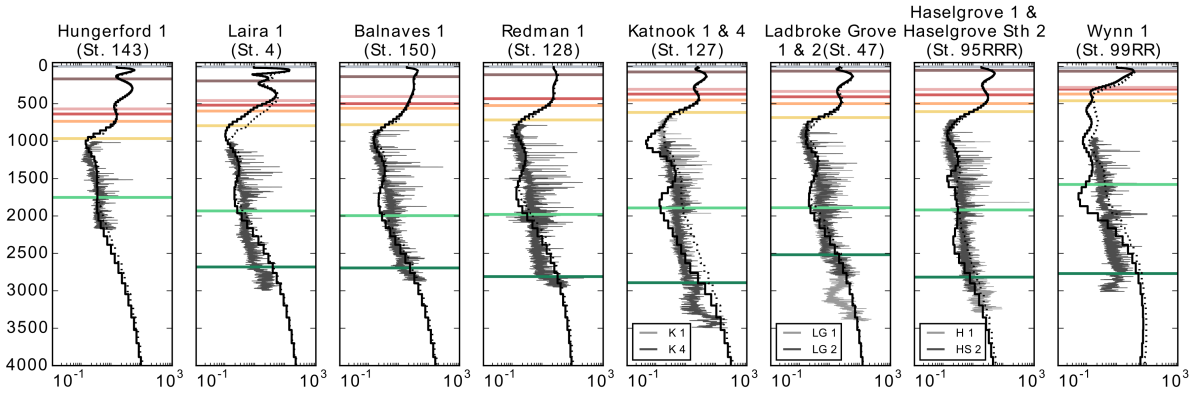

Figure 3.5: Resistivity logs for representative wells in the Penola Trough and 1D anisotropic inversion models from the nearest station to each well. Where wells are close together (< 1 km; e.g. Katnook 1–4) one or two representative wells from that region are shown. Resistivity logs shown in grey, minimum and maximum resistivity from the inversions shown in black as solid and dotted lines. Horizontal bars represent the top of various stratigraphic units with the colours indicated in Figure 3.2.

3.4.2 Resistivity logs

There are sixteen petroleum wells with open file resistivity logs in the Penola Trough (Figure 3.5). The logs start at depths > 650 m, so there is no well-log data for the sedimentary sequence above the Eumeralla Formation. The resistivity of the Eumeralla Formation is very consistent across the Penola Trough. The upper 200 m of the Eumeralla Formation is characterised by a decrease in resistivity from 3 to 1.5 Ωm, followed by an increase to around 4 – 5 Ωm at the base of the Eumeralla Formation. Resistivity continues to increase through the upper Crayfish Group units to 10 Ωm at the top of the Pretty Hill Formation. The well-log resistivity within the Pretty Hill Formation varies across the Penola Trough. In the western and central Penola Trough (e.g. the Laira, Limstone Ridge, Balnaves, Katnook and Ladbroke Grove wells), resistivity continues to increase gradually with depth through the Pretty Hill Formation. Further east in the Haselgrove and Haselgrove South wells, the increase is more moderate. In the northeast Penola Trough, Wynn 001 shows a decrease in the resistivity in the upper part of the Pretty Hill Formation, to 5 Ωm.

3.4.3 Seismic reflection data

The Haselgrove and Balnaves 3D seismic surveys were collected in 1995 and 2000 respectively and have now been merged. The surveys cover a combined area of 330 km^2 with a horizontal resolution of 20 m, and extend to 5.1 ms two-way travel-time (TWT). The vertical resolution varies with depth. At 250 ms (530 m), the dominant frequency is 20 Hz and the velocity is 2100 ms^{-1} based on check shot surveys from the Penola Trough, which gives a vertical resolution of 13 m. At 1000 ms (2900 m) the velocity is 3850 ms^{-1} and the dominant frequency is 15 Hz giving a vertical resolution of 32 m.

We have interpreted five stratigraphic horizons corresponding to stratigraphic boundaries; a strong positive reflector near the top of the Pebble Point Formation (herein referred to as the intra-Wangerrip reflector), the top Sherbrook Group, top Eumeralla Formation, top Crayfish Group and top Pretty Hill Formation (Figure 3.6). The intra-Wangerrip reflector, Crayfish Group, and in most areas, the Pretty Hill Formation, are associated with strong reflectors. The Eumeralla Formation and Sherbrook Group horizons are generally associated with a weaker and less continuous seismic signature and so the level of confidence on these horizons is lower.

The interpretations were tied to all wells in the area where stratigraphic markers were available. The markers were converted to depth using the check shot survey from the nearest well with check shot data. The horizons were then converted from TWT, (s) to depth, D (km) using the following relationship, derived by fitting a best fit curve to all available check shot data in the Penola Trough:

$$D = 1.174 \times TWT^{1.317} \tag{3.2}$$

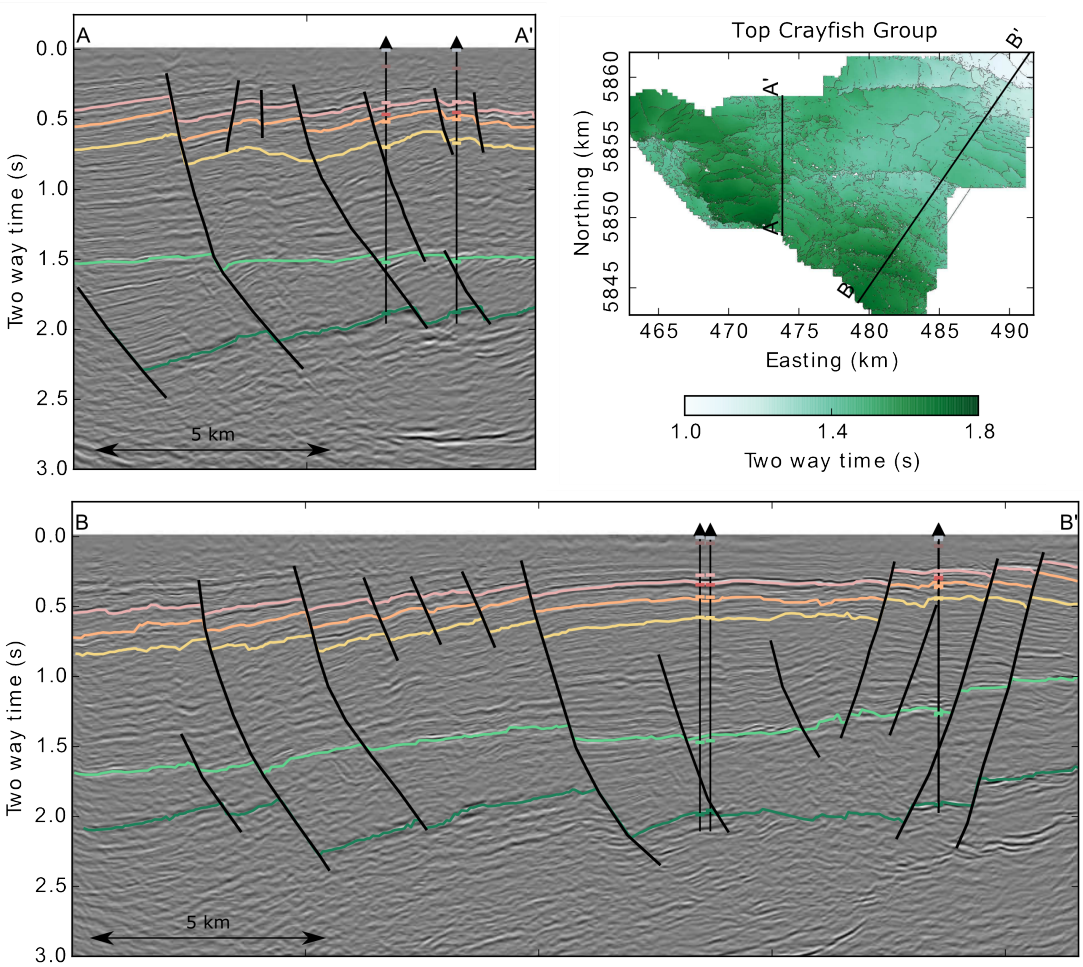

Figure 3.6: Interpretation of the HaselgroveBalnaves 3D seismic survey for five stratigraphic horizons in the Penola Trough. Top and bottom left: interpretation along two profiles, bottom right: the top Crayfish Group horizon as a map showing the profile locations. The colours of each interpreted horizon corresponds to the colours indicated in Figure 3.2.

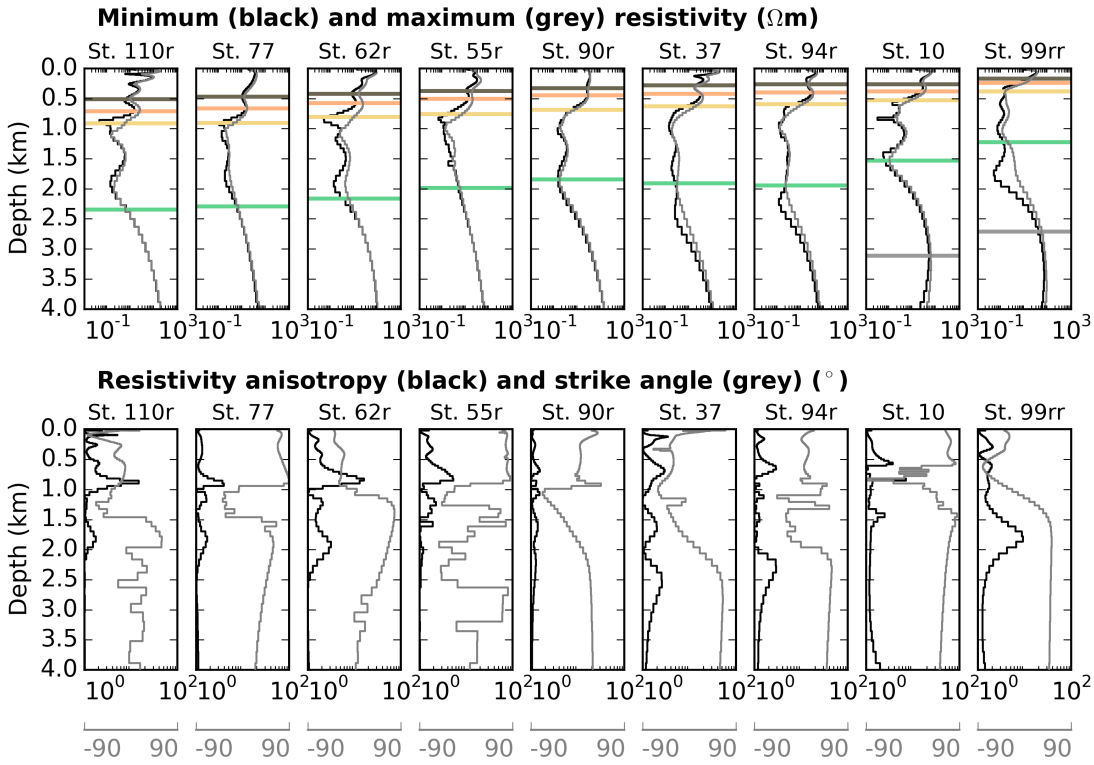

Figure 3.7: Example 1D inversion models from the Penola region selected along a northeast – southwest profile (station locations shown in Figure 3.1). Top row: minimum and maximum resistivity, with stratigraphic horizons indicated in the colours given in Figure 3.2. Bottom row: resistivity anisotropy factor (maximum/minimum resistivity) and the strike angle of the minimum resistivity.

3.5 1D anisotropic inversions

In order to assess whether the Penola MT data are consistent with anisotropic resistivity, 1D anisotropic inversions were carried out at each station using the inversion code of Pek and Santos (2006) (Figure 3.7).

In the inversions, model roughness anisotropy penalty weights can be selected. Higher penalty weights correspond to smoother and less anisotropic models and (in general) poorer fits to the data, while lower weights corresponding to rougher and more anisotropic models (Pek and Santos, 2006). Kirkby et al. (2015) used values of $10^{0.75} \approx 5.6$ for both the anisotropy and roughness penalty weights for the Koroit data. These values were determined by L-curve analysis of several sets of inversions.

To allow as direct a comparison as possible, the same anisotropy penalty weight was used for the Penola data as the Koroit data, however the structure penalty weight was increased to $10^{1.25} \approx 18$. The reason for this is that with lower penalty weights, the modelled resistivity showed strong fluctuations in the top 500 m at some stations. Increasing the structure penalty weight reduced the variability in these upper layers, whilst only increasing the median misfit by about 1 %.

Error floors of 1 % were applied to the real and imaginary Z_{XY} and Z_{YX} components, and these absolute errors were then used as error floors for the Z_{XX} and Z_{YY} components respectively. These error floors are lower than the 3 % error floors applied at Koroit, however error floors of 3 % resulted in RMS misfit values (where misfit is defined as the ratio of the difference between the data and the model response, and the data error) of less than 1. With the 1 % error floors, the median RMS misfit at each station ranges from 0.7 to 5.8, with a median of 1.55 for all stations. The wide range in misfit is a consequence of applying the same error floors and penalty weights at every station. However, at >80 % of the stations, the misfit falls between 1.0 and 3.0, with eight stations having a misfit >3.0 and seven having a misfit <1.0. This is a reasonable compromise to allow all the stations to be treated consistently. The models and their responses for some example stations are shown in Figures 3.7 and 3.3.

The 1D inversions generally match the resistivity logs well (Figure 3.5). The small differences that do exist are to be expected because MT is sampling a much larger volume than the well (a radius of several kilometres, by a depth of 3 km) so the resistivity values represented by the models correspond to resistivity averaged over a wider area.

At most stations there is very little anisotropy defined by the inversions (Figures 3.5 and 3.7). The exception to this is in the northeast Penola Trough, where the inversions have put some anisotropy within the Crayfish Group. The anisotropy strike is approximately northeast - southwest. This is 90° from the dominant orientation of open fractures identified by Bailey et al. (2014).

3.6 3D inversions

One dimensional anisotropic inversions have shown that the Penola MT data can be interpreted in terms of a primarily 1D isotropic model, with minor anisotropy in the northeast Penola Trough. However, the anisotropy strike is inconsistent with the orientation of fractures mapped in seismic data and in well logs. An alternative interpretation is a 3D, isotropic model. We have carried out 3D inversions on the data using the ModEM 3D MT inversion software (Egbert and Kelbert, 2012; Kelbert et al., 2014).

ModEM penalises differences from a prior model and the RMS misfit between the data and the model response. We used a 100 Ωm half space as the prior model, to avoid adding any structure that could bias the results.

We constructed a starting model from 1D Occam inversions (Constable et al., 1987; Key, 2009) on the Z_{YX} mode (associated with higher resistivities in this dataset) following rotation of each station to local strike. The strike was defined at each station by the mean orientation of the major axis of the phase tensor ellipse between 12.5 and 50 s. This strike orientation is consistent with the orientation of faults interpreted by Bailey et al. (2014) for the Penola Trough. The Occam 1D code was used rather than the 1D anisotropic inversions (Section 5), because it produced smoother results with greater consistency between stations. Eight stations were taken out in generation of

the starting model, as they produced 1D inversion results that were strongly different from the neighbouring stations. Linear interpolation was applied to determine resistivity between the stations, followed by a median filter with a kernel size of five in the two horizontal directions and three in the vertical direction, to smooth the linear interpolation.

The model grid has a cell size of 250 × 250 m in the horizontal directions. The vertical cell size is 20 m at the top of the model, increasing to 900 m at 12 km depth. Nine padding cells were added to each side in each horizontal direction, and six in the vertical direction, to take the model extent to 71.5 km (N–S), 80.5 km (E–W), and 274 km (vertical). The effect of the bathymetry was tested using larger model grids and was found to be negligible for this survey.

Error floors of 1 % of $\sqrt{(Z_{XY} \times Z_{YX})}$ were applied. With these error floors, the starting model had an RMS misfit of 5.3. Modelling was carried out in three stages. Initially, the model was run using the four components of the impedance tensor subsampled to every second frequency. It was then restarted using all impedance tensor data to fit the finer detail, achieving minimum RMS data-model misfit of 1.6. The model was then restarted with the vertical magnetic field (tipper) data added. Absolute error floors of 0.01 were set for the tipper magnitudes, with all tipper data from stations visibly affected by the power lines excluded from the inversion. This increased the RMS to 2.8. After 30 further iterations the final model reached an RMS misfit of 1.8. Many features from the 1D anisotropic inversion models are present in the 3D inversion, however there are a few differences. One of the more obvious differences is in the northeast Penola Trough, where the basement has shallowed considerably compared to the 1D inversions. The shallowing of basement also occurs in the top basement horizon mapped by Jensen-Schmidt et al. (2002).

Both the 1D anisotropic inversions and the 3D inversions display layering in the shallow (<4 km) resistivity structure that correlates with the seismic horizons and well markers (Figures 3.6 and 3.8). The shallowest of these is a more resistive (30 m) layer above the intra-Wangerrip reflector, which, on comparison with well markers, corresponds to the Dilwyn Formation, an important aquifer in the region (Telfer, 1993) (Figures 3.7 and 3.8). This layer was not easily mapped in the 3D seismic data. The comparatively resistive nature of this layer is consistent with the clean sandstone composition of the Dilwyn Formation (Boult et al., 2002b), and the relatively fresh groundwater present at this depth (500-670 ppm total dissolved solids (Telfer, 1993) which equates to a resistivity of 7 – 10 Ωm at 25°).

Below the intra-Wangerrip Group reflector the resistivity is variable but generally lower (10 Ωm). The underlying Sherbrook Group is also associated with variable resistivity. On the other hand, the Eumeralla Formation corresponds to a strong decrease in resistivity, and is associated with highly conductive layer that can be mapped across the Penola Trough. The resistivity reaches a minimum about 200 m below the top of the unit then increases with depth, consistent with the well logs (Section 3.4.3). The resistivity of the Eumeralla Formation varies from around 1 – 3 Ωm in most places.

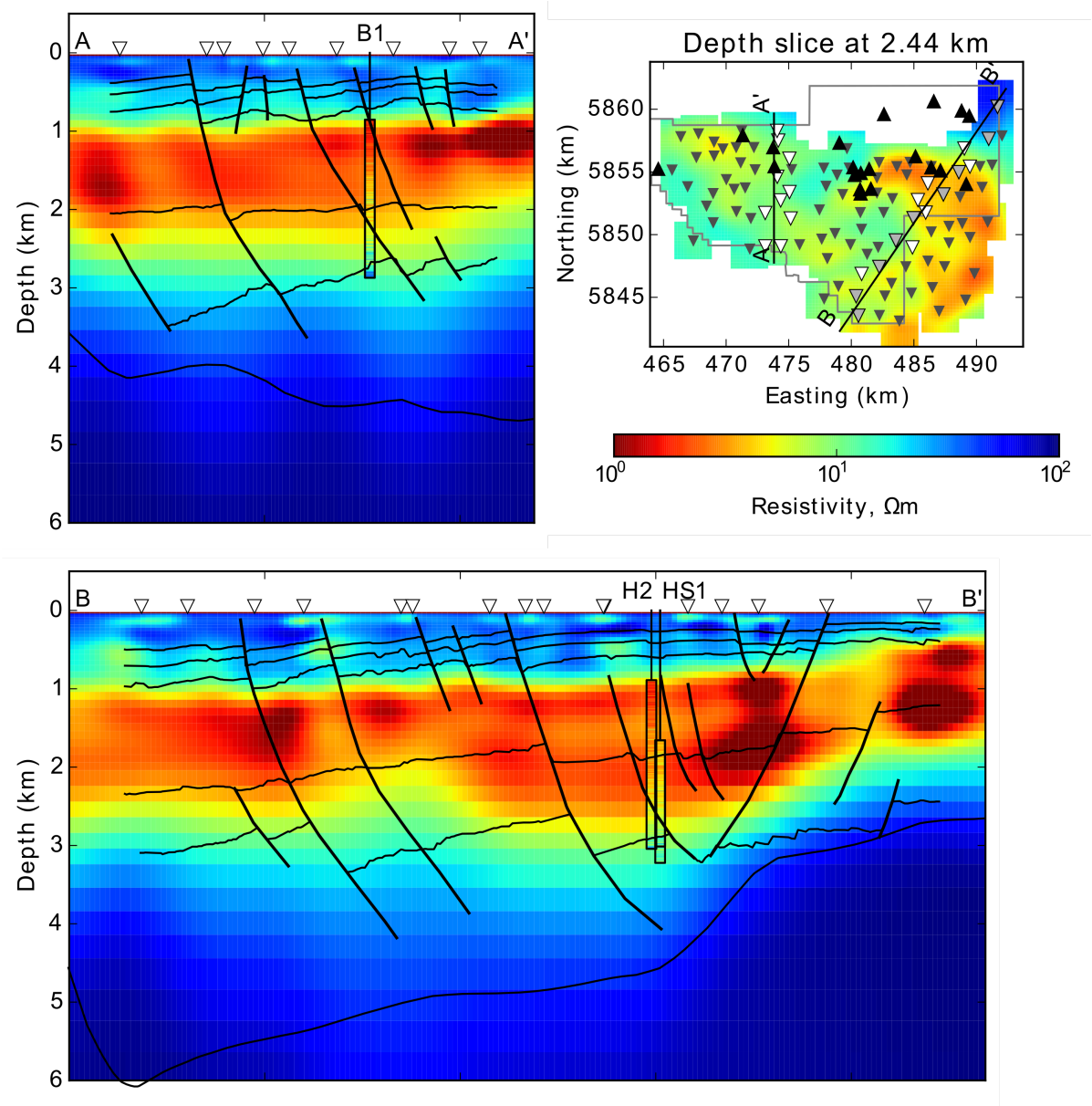

Figure 3.8: Results of 3D inversion of the Penola MT dataset along two profiles, with locations indicated on a depth slice at 2.44 km. Profile B–B' here is parallel to, but 1 km east of B–B' in Figure 3.6 to allow the stations in the northeast corner of the model to be shown. Stratigraphic horizon interpretations indicated as black lines; the basement horizon is taken from Jensen-Schmidt et al. (2002); all other horizons have been interpreted from the HaselgroveBalnaves survey (Figure 3.6). Stations shown on the cross sections indicated as white triangles; stations shown on both the cross sections and in Figure 3.7 indicated as grey triangles. Resistivity logs from wells within 2 km of the profiles are shown where available on the same colour scale as the resistivity models.

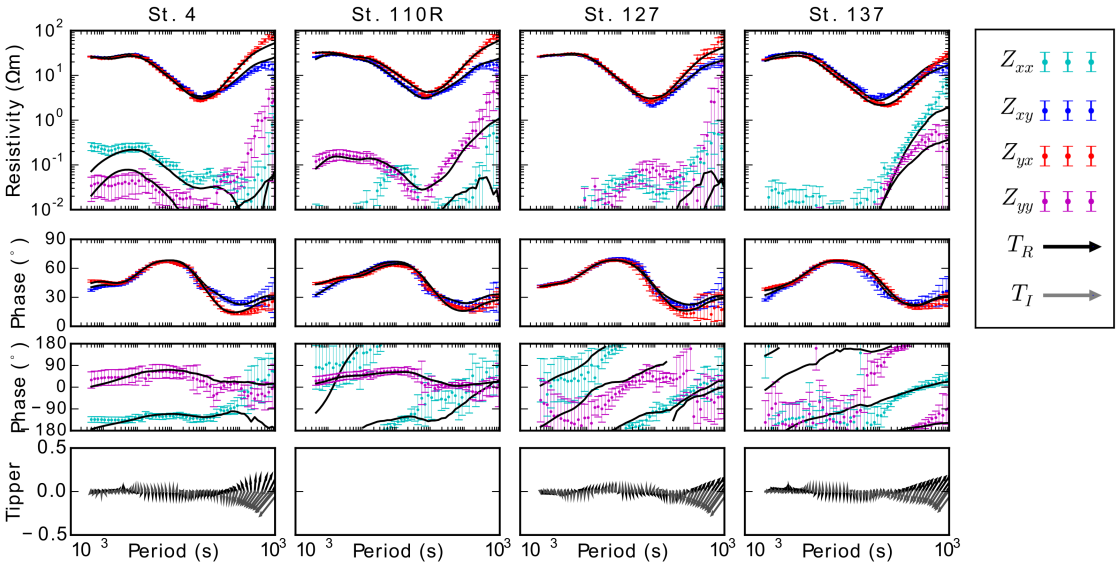

Figure 3.9: Model responses to the 3D inversion model shown in Figure 3.8. Resistivity and phase responses shown in black over the input data; real and imaginary tipper responses shown in black and grey (the input data are shown in Figure 3.3). No tipper responses shown for Station 110R as tipper data was excluded from the inversion for this station due to its proximity to the power lines. Station locations shown in Figure 3.1.

The Crayfish Group shows a less consistent resistivity signal, but is generally associated with lower resistivities in the northeast Penola Trough than in the southwest. The top of the Pretty Hill Formation shows slightly better correlation with the resistivity model, being associated with resistivities of 20 Ωm in the inversion.

3.7 Discussion

We have presented two interpretations of an MT dataset in the Penola Trough region of the Otway Basin, South Australia: a 3D interpretation, in which the basin shallows in the northeast, and a 1D anisotropic inversion, in which there is minor anisotropy at 2 – 3 km depth. The top basement horizon mapped in seismic data by Jensen-Schmidt et al. (2002) shows shallowing in the northeast Penola Trough, the amount by which is consistent with the 3D inversions, but not the 1D inversions. Furthermore, the orientation of open fractures in the Penola Trough is thought to be northwest – southeast, 90° from the anisotropy strike determined from 1D anisotropic inversions. Therefore, we conclude that the most likely model for the Penola Trough is an isotropic one. This contrasts with the Koroit study where 1D anisotropic inversions delineated strong anisotropy in the Otway Basin sequence with an orientation that was consistent known fracture orientations. We first discuss supporting evidence for, and possible reasons for, these differences. We then compare the layering in the 3D model to stratigraphic boundaries defined in well logs and seismic, highlighting the new information the resistivity model provides.

3.7.1 Differences in the MT data and inversion results between Penola and Koroit

The results presented here contrast with the anisotropic resistivity determined in the eastern Otway Basin, where 1D anisotropic inversions were used to delineate strong resistivity anisotropy in the Crayfish Group with an anisotropy strike of north-northwest (Kirkby et al., 2015). A 3D inversion was not attempted in the Koroit study and thus cannot be directly compared to the Penola results. However, the anisotropy strike delineated by 1D anisotropic inversion was found to be consistent with structural trends in the basement, which are believed to control neotectonic faulting in the region (Vandenberg, 2000; Tassone, 2014).

In contrast, 1D anisotropic inversions in the Penola Trough reveal a predominantly isotropic subsurface, with anisotropy only in the northeast Penola Trough. However, the northeast orientation of the minimum resistivity contrasts with dominant conductive fracture orientations of northwest – southeast in this area (Bailey et al., 2014). The differences in our interpretation of the MT inversion results described above between Koroit and Penola are supported by differences in well log data. The logs show resistivities of around 5 Ωm immediately above the Crayfish Group in both areas. However, at Koroit, the logs indicate a drop in resistivity in the upper Crayfish Group to 2.5 Ωm (Kirkby et al., 2015). This is not present at Penola, with resistivity increasing through the Crayfish Group. A drop in resistivity would be expected at Koroit based on the MT results, given that the anisotropic layer defined in the inversions was characterised by a reduction of the minimum resistivity in the upper Crayfish Group but little change in the maximum resistivity. The resistivity logs, which measure an average resistivity in all directions around the well, would therefore also be expected to show a decrease.

The Crayfish Group is also less permeable in the Penola Trough than Koroit, with well formation tests in the PEPS-SA database (DSD-SA, 2015) indicating a maximum permeability of 72 mD within the Crayfish Group and median of 3.4 mD. This can be compared to permeability as measured in Pretty Hill 1 in Koroit, which is higher within the Crayfish Group than any other rock unit, with a median of 600 mD. An explanation for these differences in resistivity and permeability may be in differences in the orientation of the pre-existing fractures in each region and their relationship to the present day stress field. Changes in the mean aperture of faults by amounts as small as 0.1 mm or less can produce large changes in resistivity by pushing them over their percolation threshold (Kirkby et al., 2016).

The orientation of the maximum horizontal stress, SH_{max}, in the Otway Basin, is rotated by 10° from the western Otway Basin (South Australia) to the central Otway Basin in Victoria (Nelson et al., 2006), and the orientation of open fractures also changes slightly, from northwest to north-northwest. The stress regime in the Otway Basin is thought to be strike-slip i.e. $SH_{max} < Sv < Sh_{min}$ (Nelson et al., 2006). However, both the Sh_{min} and SH_{max} gradient (minimum and maximum horizontal stress as a function of depth), and as a result, the differential stress, are observed to increase from the western to eastern Otway Basin whilst the vertical stress remains largely similar, although we note that there is no stress data within the Koroit region

itself (Nelson et al., 2006; Tassone, 2014). This change in stress coincides with an increase in the intensity of measured neotectonic deformation from east to west (Clark et al., 2011; Holford et al., 2014; Tassone, 2014). Hermanrud and Bols (2002) showed that lower differential stresses are associated with a greater range of fractures being oriented favourably for reactivation. The more isotropic stress state in the Penola Trough may therefore result in a wider range of fractures being open, resulting in isotropic resistivity characteristics. More anisotropic stress conditions in the Koroit region could result in a smaller range of fractures being open, which is consistent with the anisotropic resistivity determined in this area. However, direct constraints on stress magnitudes in the Koroit region are required in order to test this notion further.

It is noted that while the resistivity, permeability and fracture distribution determined by MT for the Penola Trough and Koroit regions of the Otway Basin is consistent with existing data, the MT alone is not sufficient to distinguish between anisotropic and isotropic models. This demonstrates the importance of interpreting MT data in conjunction with other available data. It can be impossible to distinguish between a 1D anisotropic and 2D isotropic subsurface based on the impedance tensor at one site alone (Section 3.3.1; Heise et al., 2006; Martí, 2014). Even when arrays of measurements are available there can still be ambiguity, and this is the case in both Penola and Koroit. As we have shown, data such as reflection seismic and well resistivity logs can assist with choosing between different resistivity models that are obtained from inversion of MT data.

3.7.2 Magnetotellurics: a tool for subsurface mapping in sedimentary basins

Three dimensional inversion of MT data has been effective in mapping key stratigraphic units in the Penola Trough. Some of these (e.g. the Eumeralla Formation) are resolved poorly in 3D seismic, but clearly in the resistivity model. The resistivity model also appears to be consistent with the depth to basement interpretation of Jensen-Schmidt et al. (2002) based on seismic data. This shows that MT may have merit in delineating the basement in areas where there is no seismic, or where the basement horizon is poorly resolved in seismic data. At the other end of the scale, the resistivity model in some parts of the Penola Trough has also been successful in mapping layering at depths shallower than were resolved by the seismic data (e.g. Dilwyn Formation).

These results show that MT can be a useful complementary technique to seismic reflection in sedimentary basins that can assist with defining the distribution of different lithologies in cases where they have poor reflectivity or are simply too deep to be mapped with seismic data. Even in highly reflective layers that are mapped easily by seismic reflection data, the MT data provides information on their resistivity, which can be useful in inferring lithological information.

Moreover, that the MT results agree well with some key seismic horizons demonstrates the utility of broadband MT as a low cost alternative (or addition) to seismic reflection data for mapping sedimentary basin structure in poorly explored regions.

3.8 Conclusions

Our conclusions are as follows:

1. Based on integration of MT results, seismic reflection and well data, an isotropic resistivity structure has been determined for the Penola Trough region of the Otway Basin. An isotropic resistivity model contrasts with the anisotropic interpretation of MT data determined for the eastern Otway Basin by Kirkby et al. (2015).

2. Three dimensional inversion of MT data has been shown to be effective in mapping key stratigraphic horizons in the Penola Trough including some that are poorly resolved in 3D seismic. This demonstrates the use of MT as an alternative, or complementary, technique to seismic in exploring sedimentary basins.

3. As shown by previous authors (e.g. Heise et al., 2006; Martí, 2014), there is inherent ambiguity in MT data when distinguishing between 1D anisotropic and 2D isotropic models. The Penola data demonstrates that even when arrays of measurements are available there still can be ambiguity. It is necessary to interpret MT in context of other measurements to obtain a consistent interpretation.

CHAPTER

FOUR

RELATING PERMEABILITY AND ELECTRICAL RESISTIVITY IN FRACTURES USING RANDOM RESISTOR NETWORK MODELS

Alison Kirkby[1,2], Graham Heinson[1], and Lars Krieger[1]

[1] Electrical Earth Imaging Group, School of Physical Sciences, University of Adelaide, Adelaide, SA 5000, Australia
[2] Geoscience Australia, Canberra, ACT 2601, Australia

Published on March 15th, 2016 as:
Kirkby, A.L., Heinson, G., and Krieger, L., 2016. Relating permeability and electrical resistivity in fractures using random resistor network models. Journal of Geophysical Research: Solid Earth, v. 121, pp. 1546-1564.

Statement of Authorship

Title of Paper	Relating permeability and electrical resistivity in fractures using random resistor network models
Publication Status	☑ Published ☐ Accepted for Publication ☐ Submitted for Publication ☐ Unpublished and Unsubmitted work written in manuscript style
Publication Details	Kirkby, A.L., Heinson, G., and Krieger, L., 2016. Relating permeability and electrical resistivity in fractures using random resistor network models. Journal of Geophysical Research: Solid Earth, v. 121, pp. 1546-1564.

Principal Author

Name of Principal Author (Candidate)	Alison Kirkby
Contribution to the Paper	Developed conceptual framework, modelling technique, and wrote the modelling code, carried out the modelling and wrote the manuscript
Overall percentage (%)	90%
Certification:	This paper reports on original research I conducted during the period of my Higher Degree by Research candidature and is not subject to any obligations or contractual agreements with a third party that would constrain its inclusion in this thesis. I am the primary author of this paper.
Signature	Date: 8/Aug/2016

Co-Author Contributions

By signing the Statement of Authorship, each author certifies that:

i. the candidate's stated contribution to the publication is accurate (as detailed above);

ii. permission is granted for the candidate in include the publication in the thesis; and

iii. the sum of all co-author contributions is equal to 100% less the candidate's stated contribution.

Name of Co-Author	Graham Heinson
Contribution to the Paper	Contributed to development of technical concept and interpretation of results, aided with manuscript evaluation.
Signature	Date: 8TH AUG 2016

Name of Co-Author	Lars Krieger
Contribution to the Paper	Aided with modelling code development and manuscript evaluation.
Signature	Date: 09.08.2016

SUMMARY

We use random resistor network models to explore the relationship between electrical resistivity anisotropy and permeability in a fracture filled with an electrically conductive fluid. Fluid flow and current are controlled by both the distribution and the volume of pore space. Therefore the aperture distribution of fractures must be accurately modelled in order to realistically represent their hydraulic and electrical properties. We have constructed fracture surface pairs based on characteristics measured on rock samples. We use these to construct resistor networks with variable hydraulic and electrical resistance, to investigate the changes in both properties as a fault is opened. At small apertures, electrical conductivity and permeability increase moderately with aperture until the fault reaches its percolation threshold. Above this point, the permeability increases by four orders of magnitude over a change in mean aperture of less than 0.1 mm, while the resistivity decreases by up to a factor of 10 over this aperture change. Because permeability increases at a greater rate than matrix to fracture resistivity ratio, the percolation threshold can also be defined in terms of the matrix to fracture resistivity ratio, M. The value of M at the percolation threshold, M_{PT}, varies with the ratio of rock to fluid resistivity, the fault spacing, and the fault offset. However, M_{PT} is almost always less than 10. Greater M values are associated with fractures above their percolation threshold. Therefore, if such M values are observed over fluid-filled fractures, it is likely that they are open for fluid flow.

4.1 Introduction

Permeability in the crust comprises both primary permeability, from interconnected pore space present at the time of deposition of sedimentary rocks, and secondary permeability, resulting from, for example, fractures and faults. Primary permeability is often not preserved once a rock becomes compacted or is subjected to high temperatures, and therefore geothermal reservoirs often rely on secondary permeability in order to obtain adequate flow rates for commercial production (e.g., Barton et al., 1997; Barelli et al., 2000; Cumming, 2009; Muñoz, 2014). Unconventional oil and gas reservoirs are also often contained in low permeability rocks and therefore often rely on fractures for permeability. However, while larger faults (with lengths on the scale of several meters or more) can be detected using methods such as seismic reflection, they are not always permeable, and it can be difficult to determine their permeability without using drilling data (e.g., Backé et al., 2011; Bailey et al., 2014). Moreover, it is often the minor faults, and the damage zones around major faults, which are not easily imaged using geophysical methods, that provide much of the permeability (e.g., Caine et al., 1996). Therefore, characterizing the distribution of secondary permeability from the surface can be a challenge.

It has been shown that the introduction of an electrically conductive fluid into a natural fault network can produce changes in the bulk electrical conductivity that are measurable from the surface using the magnetotelluric (MT) method (Peacock et al., 2012, 2013; MacFarlane et al., 2014). Magnetotelluric data have also been used to infer, in a qualitative sense, the flow properties of natural fractures (e.g., Kirkby et al., 2015). In these examples, the electrical resistivity was interpreted to not only vary spatially but with orientation. In the Otway Basin, Australia, 1D anisotropic inversions of MT data showed the bulk (>100 m scale) resistivity to be lower in the north-northwest direction, with anisotropy ratios of up to 100 determined from the inversions (Kirkby et al., 2015). The anisotropy was interpreted to result from the presence of widespread, fluid-filled fractures and faults. MacFarlane et al. (2014) used an anisotropy ratio of 200 to model a fracture zone in an Enhanced Geothermal System (following injection of conductive fluids) in Paralana, South Australia.

Characterising the resistivity anisotropy of faults and fractures helps determine the amount by which the faults enhance the conductivity. When the conductivity enhancement can be attributed to fluids contained in the fractures it may be possible to use the resistivity to infer their permeability. This can be done in porous rocks by using models such as Archie's Law to infer porosity (Archie, 1942; Glover, 2010), and then obtaining permeability through models such as the Kozeny-Carman relationship (Kozeny, 1927; Carman, 1937). However, the amount and distribution of pore space in fractured, low porosity rocks is likely to be different to that in porous rocks, and both fluid flow and electrical conduction rely strongly on the distribution of pore space as well as the total volume (e.g., Brown, 1989). Therefore, relating resistivity and permeability directly may be more relevant for deducing the fluid flow properties of fractures and faults.

Brown (1989) discussed the analogy between electrical current and fluid flow. Current is described by Ohm's Law, which relates current to the potential difference between two points and the resistance of the medium. Likewise, fluid flow is described by Darcy's Law, with the flow rate controlled by a pressure difference between two points and the permeability of the medium. This similarity suggests the two processes can be compared to explore the relationship between the two properties (e.g., Brown, 1989; Bernabé, 1995).

Here we present modeling that utilizes the similarities between the flow of electrical current and fluids to provide a first step in better understanding the relationship between resistivity and permeability in fractured rocks. The modeling is carried out on single rough fractures, constructed based on characteristics measured on rock fracture surfaces. Fractures with different offsets, filled with fluids of different resistivities, in rocks with a range of different resistivities and permeabilities have been analyzed. Furthermore, the ability of a fracture to transmit fluid is directly related to its aperture, which is primarily controlled by the orientation and magnitude of the in-situ stress field, but also by rock strength, fracture plane orientation, roughness and the pore-fluid pressure (Jaeger and Cook, 1969; Barton et al., 1995). Therefore, each fracture is progressively opened to investigate the changes in resistivity and permeability as the aperture is increased. This work may help to improve our understanding of resistiv-

ity anomalies resulting from the presence of fluid-filled fractures, characterized using techniques such as MT. This method may also provide a proxy for experimental measurements of fracture permeability, which are time consuming, and therefore difficult to repeat sufficiently to produce results that apply generally.

4.2 Background

4.2.1 Resistor networks

Bahr (1997) proposed the use of random resistor networks to evaluate the bulk electrical conductivity of a medium. In this type of analysis, electrical current flow is assumed to occur through a network of resistors. Resistors within this network can be defined to be open (i.e., high electrical conductivity) or closed (low conductivity). An electrical potential gradient is applied across the network and used, together with the resistances in the network, to construct a matrix, which is then solved to determine the current passing through each resistor. The bulk resistivity is then calculated by summing the total current through the network and applying Ohm's Law to the whole network.

We extend the analysis of Bahr (1997) by considering resistors of variable resistance, and by considering fluid flow through the same network. In this case the resistors can be considered in terms of a network of flat plates with varying apertures, corresponding to varying hydraulic conductivity. The open resistors can be compared the open parts of a fracture, filled with an electrically conductive fluid, whilst the closed resistors can be compared to the background host rock and/or parts of the fault that are closed or cemented with electrically and hydraulically resistive cement. Importantly, the conductivity is controlled not only by the number and aperture of open bonds, but also on their position within the network.

A resistor network approach implies laminar fluid flow, and low resistivity fluids such that the electrical double layer (EDL), a layer that forms on the surface of an object when it is exposed to a solution, can be considered to have near-zero thickness. Laminar flow occurs when the Reynold's number, or the ratio of momentum to viscous forces is less than about 2000 (Reynolds, 1883; Drazin and Reid, 2004). Given a maximum local fault aperture of 6 mm as considered here, we therefore expect laminar fluid flow at velocities of < 0.3 ms^{-1} for a water temperature of 20° C and < 0.1 ms^{-1} for a water temperature of 100° C. Natural groundwater flow rates, which are generally less than 0.5 m year^{-1} (e.g., Garven, 1995) are well within these limits.

The thickness of the electrical double layer (EDL) is inversely related to the concentration and charge of ions in solution, and also decreases slightly with increasing temperature (Scholz, 2009). The electrical double layer thickness can be approximated by 1.5κ where κ is the Debye-Hückel length (Scholz, 2009). For a fluid at 20° C with a salinity of 30,000 ppm (e.g. seawater) corresponding to a resistivity of 0.23 Ωm, this equates to an EDL thickness of approximately 0.45 nm . For a low salinity of 100 ppm, the EDL thickness is about 2.5 nm and the resistivity 5.5 Ωm. For these EDL thicknesses applied to the scenarios considered in this work, we estimate that neglecting the EDL

would result in underestimation of local resistances by up to 6 % in the former case and up to 24 % in the latter. Therefore the results presented here are most accurate for fluids with higher salinities.

4.2.2 Hydraulic and electrical resistance

The resistance of the bonds can be calculated using an effective electrical and hydraulic resistance at each point within the fracture. In porous media, the hydraulic resistance is described by Darcy's Law:

$$Q = \frac{kA}{\mu}\nabla p \tag{4.1}$$

where Q is the volumetric flow rate, k is the permeability, μ is the viscosity, p is the pressure and A is the cross sectional area of the sample. The hydraulic resistance is given by

$$R_H = \frac{\mu \Delta x}{kA} \tag{4.2}$$

Where Δx is the length of the bond along the direction of fluid flow. Likewise, Ohm's law describes electric current I:

$$I = \frac{A}{\rho}\nabla v \tag{4.3}$$

where ρ is the resistivity of the medium and v is the electrical potential. The electrical resistance is equal to

$$R_E = \frac{\rho \Delta x}{A} \tag{4.4}$$

4.2.3 Electrical and hydraulic resistance in fractures

In fractures, fluid flow is commonly described by the parallel plate model, where two fracture surfaces are approximated as smooth plates with separation b and width l_y. The steady state solution of the Navier-Stokes equations for laminar fluid flow leads to a cubic dependence of fluid flow on aperture (e.g., Witherspoon et al., 1980; Brown, 1989):

$$Q = -l_y \frac{b^3}{12\mu}\nabla p \tag{4.5}$$

In a fracture with a variable aperture, this equation can be evaluated pointwise on a discretized grid. This is known as the local cubic law (Brown, 1987).

Using Darcys Law we obtain the permeability of the fracture as $b^2/12$ (Brown, 1987), and the local hydraulic resistance is

$$R_H = \frac{12\mu\Delta x}{l_y b^3} \tag{4.6}$$

In contrast, the electrical resistance R_E has a linear dependence on the aperture b. The current I conducted by the fluid is:

$$I = \frac{l_y b}{\rho_f}\nabla v \tag{4.7}$$

and therefore

$$R_E = \frac{\rho_f \Delta x}{l_y b} \tag{4.8}$$

where ρ_f is the resistivity of the fluid.

As noted by Brown (1989), Equations 4.6 and 4.8 have a similar form.

Brown (1989) used the above equations to model the electrical current and fluid flow through a single fracture. The modeling showed that fluid flow shows much stronger channeling in the fracture plane, resulting from the cubic dependence of fluid flow on aperture. Brown (1989) used the results to derive a relationship between the formation factor, defined as the ratio of the fractured rock to that of the pore fluid itself, and the permeability. It was shown that it is necessary to consider variations in aperture within the fracture, and not just the mean aperture, where the standard deviation of the fracture surface height is greater than about 20 % of the mean fracture aperture.

However, while the local parallel plate model provides an improved approximation to the current and fluid flow compared to a global parallel plate model, it is still limited in that it assumes that the faces of each fault segment are parallel and horizontal, and that each segment of the fault face is long compared to the aperture. In reality, fracture topography varies strongly within a fracture, with the aperture fluctuations comparable to (or often greater than) horizontal distance, and the two faces are not parallel (e.g., Brown and Scholz, 1985; Brown, 1995). To account for this, a modified parallel plate model can be used, based on the solution to the Navier-Stokes equations in a wedge, which also accounts for any additional distance in flow path resulting from sloping plates (Nicholl et al., 1999; Brush and Thomson, 2003). Brush and Thomson (2003) showed that this modified local cubic law provides a good approximation to the full Navier-Stokes solutions at low flow velocities such as those likely to be encountered in the subsurface.

4.2.4 Fracture surface topography

The aperture distribution within a fracture is an important control on the electrical current and fluid flow through that fracture. The aperture distribution also controls electrical current and fluid flow differently (Equations 4.6 and 4.8). Therefore, in order to explore the relationship between the two properties in fractures it is important to accurately represent the aperture distribution of these fractures.

Measurement on rock samples shows the topography of fracture surfaces follows a fractal distribution, i.e., height variations are self-similar across different scales (Mandelbrot, 1983; Brown, 1987). Fractures have been shown to have power spectral density functions of the form

$$G(f) \propto f^{-\alpha} \tag{4.9}$$

where G is the power spectral density, f is the spatial frequency and α is related to the fractal dimension D through

$$\alpha = \frac{7 - D}{2} \tag{4.10}$$

(Brown, 1987). Fractal dimension ranges from about 2.2 to 2.6 in rock fractures (e.g., Brown, 1995; Glover et al., 1998b; Matsuki et al., 2006; Ishibashi et al., 2015). Brown (1995) used this relationship to develop an algorithm for generating self-similar fracture surfaces, which uses the inverse Fourier transform to generate fractures with power spectral density functions described by Equations 4.9 and 4.10. The phase of each Fourier component was scaled by a random number between zero and one, in order to replicate the random phase spectra that has been observed in natural rock fractures (Brown, 1995).

The absolute amplitude of surface height variations, measured in terms of the standard deviation σ_h, scales with the length L of a profile across the fracture (Matsuki et al., 2006):

$$\sigma_h = \sigma_{h,ref} \left(\frac{L}{L_{ref}} \right)^{3-D} = sL^{3-D} \tag{4.11}$$

where L_{ref} and $\sigma_{h,ref}$ are the length and standard deviation of the heights for a reference fracture surface. These can be combined to give s, a fracture length-independent scaling factor:

$$s = \frac{\sigma_{h,ref}}{L_{ref}^{3-D}} \tag{4.12}$$

Figure 4.1 shows fractal dimension and scaling factor for some rock samples, calculated from measured fracture surface profiles (Brown, 1995; Matsuki et al., 2006; Ishibashi et al., 2015). Broadly, there is an inverse relationship between the two parameters. That is, in fracture surfaces with high fractal dimensions the standard deviation of the surface height overall tends to be smaller.

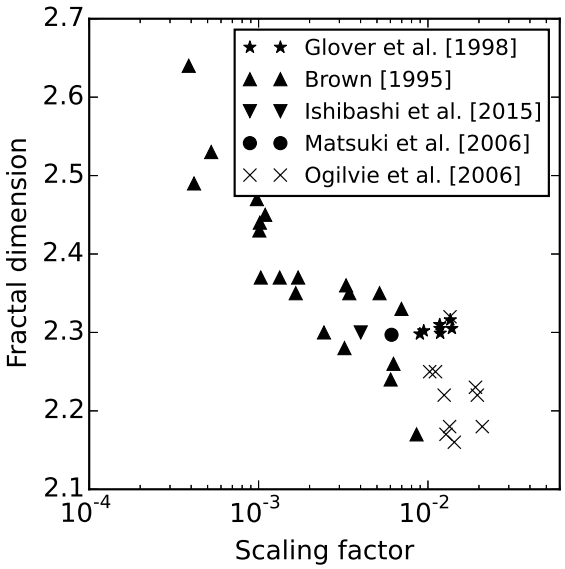

Figure 4.1: Fractal dimension as a function of scaling factor as defined by Equation 4.12 for measured samples.

Table 4.1: Mismatch frequency cutoff values measured in rock samples

Reference	Mismatch wavelength cutoff (mm)
Glover et al. (1997, 1998b,a)	0.25 – 1.11
Ogilvie et al. (2006)	2.3 – 8.0
Matsuki et al. (2006)	0.568
Ishibashi et al. (2015)	0.7

The degree of correlation between the two faces of a fracture increases with increasing wavelength (Brown, 1995). That is, opposing fracture surfaces tend to be well correlated on the broad scale and less correlated on the small scale. A cutoff frequency (or equivalently, cutoff wavelength) can be defined, above which the surface height variations are independent of each other. Table 4.1 summarises some cutoff frequency values measured in rock samples.

The shape of the cutoff has been treated differently by different authors. Brown (1995) applied a sharp cutoff, where the random numbers scaling the phase of each Fourier component of the two fracture surfaces are the same below the cutoff frequency and independent of each other above it. However, Glover et al. (1998b) and later Ogilvie et al. (2006) recognised that a sharp frequency cutoff is unrealistic for natural rock fractures, and modified the model to include a ramped cutoff. Below the cutoff, the phase of each fourier component is given by $2\pi R_3$ where $R_3 \epsilon [0, 1]$ is given by $R_3 = \gamma R_1 + (1 - \gamma) R_2$. The random number R_1 is identical for the two surfaces while R_2 is independent for each surface. The scaling coefficient γ is linearly related to frequency

by $\gamma = \beta(1 - \frac{f}{2f_c})$, where β determines the minimum amount of correlation between the two surfaces. Glover et al. (1998b) set β to 0.6.

Matsuki et al. (2006) defined γ slightly differently, with R_3 being given by $R_3 = R_1 + \gamma R_2$ where γ ranges from 0.0 to 1.0. In this case, the difference in phase between the two surfaces is given by $2\pi\gamma R_2$ (Matsuki et al., 2006). Matsuki et al. (2006) derived a function for γ based on the power spectrum of their measured fracture.

We use a mismatch wavelength cutoff of 1 mm and follow Matsuki et al. (2006) for the definition of the parameter γ. We define γ as a linear function of frequency (Section 4.3.1). The power spectrum of a typical fracture produced by this method is presented in Figure 4.2.

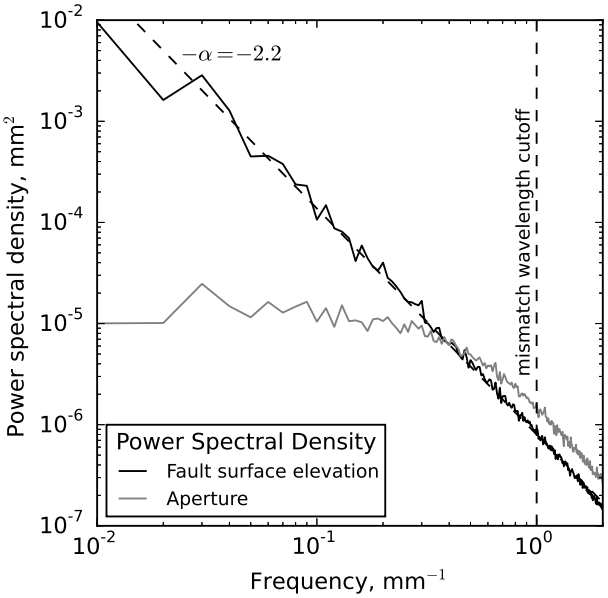

Figure 4.2: The power spectral density (PSD) of the lower fracture surface elevation and aperture for a synthetic fracture. At low frequencies, the PSD of the aperture is small compared to the PSD of the aperture, i.e., the two fracture surfaces follow each other closely. At higher frequencies, the PSD of the aperture is larger relative to the PSD of the surface height, approaching two times the PSD of the surface height variations at the mismatch wavelength cutoff of 1 mm. This means that small (<1 mm) undulations in the two opposing fracture surfaces are almost independent of each other. The slope of the PSD, α, is related to the fractal dimension D through Equation 4.10.

4.2.5 Fault offset

Because fault surfaces are correlated on wavelengths greater than the mismatch wavelength cutoff, introducing offset, or displacement, between two opposing fault surfaces should decrease the correlation between them at any given point on the fault surface. This will affect the aperture distribution and therefore may influence the relationship between hydraulic and electrical conductivity.

Fault offset d scales with fault length L according to the relationship

$$d = cL^n \tag{4.13}$$

(Kim and Sanderson, 2005). The exponent n has been shown to range from 0.5 to 2.0 (e.g., Watterson, 1986; Marrett and Allmendinger, 1991; Schlische et al., 1996; Fossen and Hesthammer, 1997). The constant c is usually between 10^{-6} and 10 but varies depending on the exponent n, the geological province and the type of fault. However, displacement data from faults from a wide range of geological settings and scales (e.g., Muraoka and Kamata, 1983; Scholz and Cowie, 1990; Schlische et al., 1996; Kim et al., 2000) shows that for faults less than 1 km in length, the ratio d/L is generally between 10^{-3} and 10^{-1}. That is, offset is normally less than 10 % of fault length.

4.2.6 Fault spacing

The spacing between faults is an important factor controlling the electrical and hydraulic properties of a faulted medium. We define the fault spacing in terms of the spatial frequency of faults in one dimension, i.e., the number of faults that would be encountered when traversing along a profile perpendicular to the fault plane.

The spatial frequency of faults of a given length is inversely correlated with the length of the fault (Bonnet et al., 2001). In sedimentary basins, faults have been shown to form at a predictable spatial frequency which is inversely related to bed thickness but is also related to lithology (Ladeira and Price, 1981).

4.3 Method

4.3.1 Fault surface creation

The fault aperture distribution was determined by constructing two correlated fractal fracture surfaces then separating them by a given distance.

We generated the fracture surfaces using the method of Matsuki et al. (2006) and Brown (1995). In this method, the Fourier component a of each fracture surface is related to the fractal dimension D and the spatial frequencies p and q in the x and y direction, where l is the size of the fracture through

$$a_{1\ p,q} \propto \left(p^2 + q^2\right)^{((4-D)/2)} e^{i2\pi R_1} \tag{4.14}$$

$$a_{2\ p,q} \propto \left(p^2 + q^2\right)^{((4-D)/2)} e^{i2\pi(R_1 + \gamma R_2)} \tag{4.15}$$

Where R_1 and R_2 are independent uniform random numbers between 0 and 1.

The surfaces differ by the random component R_2, scaled by γ which is defined based on the mismatch cutoff frequency f_c (Section 4.2.4):

$$\gamma = \begin{cases} 1 & f > f_c \\ \frac{f}{f_c} & f \leq f_c \end{cases}$$

Once the two fracture surfaces had been created, they were scaled according to Equation 4.11 and separated by a series of different fixed values for modeling. In cases where offset was to be introduced between the surfaces, the top surface was shifted horizontally in the direction perpendicular to that in which fluid flow and current were to be modeled. Overlapping parts of the fracture resulting in negative apertures were set to zero. This implies that any extra material that was represented by the overlapping section has been washed out of the system and does not remain within the fracture. An example of the resulting fracture surfaces and aperture distribution is shown in Figure 4.3.

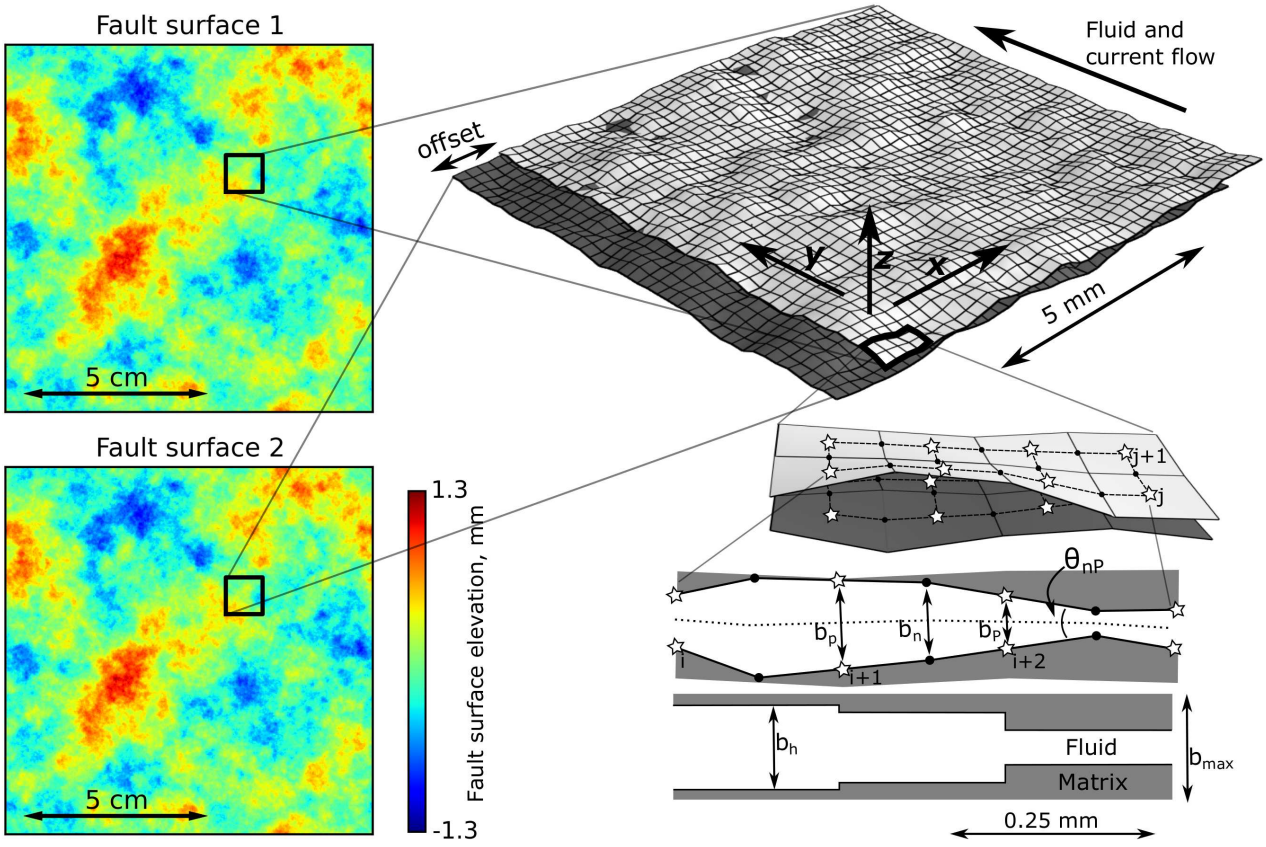

Figure 4.3: Diagram showing key features of the model setup used for modeling fluid flow and current through fractures. Parameters used for calculating the effective hydraulic and electric aperture are shown, including the midpoints of each flat plate (white stars) and aperture at these points b_p, the center points of the edges of the plates (black dots), the aperture at these points (b_n), and the local relative angle between the plates, θ. The two surfaces shown have dimensions of 100 × 100 mm, and were created using a fractal dimension of 2.4 and an elevation scale factor of 1.9 $\times 10^{-3}$. The surfaces have an offset of 1 mm between them.

4.3.2 Modified local cubic law

The modified local cubic law introduced in Section 4.2.3 adjusts the local fault aperture to an effective hydraulic aperture based on the local slope of the two fracture planes and the angle between the two plates (Brush and Thomson, 2003). This aperture is then used to determine the hydraulic resistance. The calculation of effective hydraulic aperture is summarized here.

First, a pair of fracture surfaces are constructed as in Section 4.3.1 on a regular grid. The grid points define the corners of a series of connected flat plates (Figure 4.3). The effective hydraulic aperture is evaluated between adjacent midpoints of these plates in two orthogonal directions.

The effective hydraulic aperture between two midpoints is calculated based on the effective aperture for two adjacent half volumes. To obtain the effective aperture for each half volume, we first calculate the effective hydraulic aperture for the midpoint of each plate $b_{h,p}$, evaluated based on the aperture at the center of the two adjacent plate edges in the direction perpendicular to flow. Because fluid flow rate is proportional to the cube of the aperture, the mean is defined as (for fluid flow in the i direction):

$$b_{hx\ i,j} = \left(\frac{b^3_{i,j-1/2} + b^3_{i,j+1/2}}{2} \right)^{1/3} \tag{4.16}$$

The effective hydraulic aperture at the end of each plate $b_{h,n}$ is calculated from Equation 4.16 based on the aperture at the two adjacent plate corners.

The effective apertures of the two adjacent half volumes are calculated from the apertures at the mid-point of each plate $b_{h,p}$, the aperture at the common end of the two plates $b_{h,n}$, and the local angle between the upper and lower plate, θ:

$$b_{h,pn} = \frac{2b^2_{h,p}b^2_{h,n}}{b_{h,p} + b_{h,n}} \frac{3(tan\theta - \theta)}{tan^3\theta} \tag{4.17}$$

(Nicholl et al., 1999; Brush and Thomson, 2003).

The effective hydraulic aperture between two adjacent mid-points, $b_{h,pP}$ is then calculated using a weighted harmonic mean of the effective aperture for the two half volumes:

$$b^3_{h,pP} = \left(\frac{1}{2\beta_{pn}b^3_{h,pn}} + \frac{1}{2\beta_{nP}b^3_{h,nP}} \right)^{-1} \tag{4.18}$$

Where the weighting factor β_h is defined by:

$$\beta_{h,AB} = \frac{\eta^3_z}{|\ \mathbf{r}_A - \mathbf{r}_B\ |} \tag{4.19}$$

Where η_z is the z component of the unit normal vector to the mid-point between the two surfaces, and $\mathbf{r}$ is the position vector of the midpoint between the two fracture surfaces at a and b (Brush and Thomson, 2003).

4.3.3 Geometry correction for electrical resistance

The effective electrical aperture can be evaluated in a similar manner to the hydraulic aperture.

Using the fracture surface pair in Section 4.3.2, the effective electrical aperture $b_{e,p}$ is calculated for the midpoint of each plate. Since electrical conductivity is linearly related to aperture, this is simply the arithmetic mean of the center points of the plate edges adjacent to each mid-point in the direction perpendicular to flow:

$$b_{ex\ i,j} = \frac{b_{i,j-1/2} + b_{i,j+1/2}}{2} \tag{4.20}$$

The effective aperture is the harmonic mean of every point along the fault segment. The effective electrical aperture $b_{e,l}$ at any given point l between the midpoint and the end of each plate is given by

$$b_{e,l} = b_{e,p} + \frac{b_{e,n} - b_{e,p}}{(\Delta x)/2} l \tag{4.21}$$

Integrating between the mid-point and end-point of each plate and dividing by the distance between the mid and end points $\Delta x/2$, we obtain

$$\frac{1}{b_{e,pn}} = \frac{2}{\Delta x} \left(\int_0^{\frac{\Delta x}{2}} \frac{1}{b_{e,p} + \frac{b_{e,n} - b_{e,p}}{(\Delta x)/2} l} dl \right) \tag{4.22}$$

which reduces to

$$b_{e,pn} = \frac{(b_{e,n} - b_{e,p})}{ln(b_{e,n}) - ln(b_{e,p})} \tag{4.23}$$

Once the effective aperture has been calculated in each half volume, the mean aperture between the midpoints of two adjacent planes can be calculated:

$$b_{e,pP} = \left(\frac{1}{\beta_{pn} b_{e,pn}} + \frac{1}{\beta_{nP} b_{e,nP}} \right)^{-1} \tag{4.24}$$

Where the weighting factor β_e is defined by:

$$\beta_{e,ab} = \frac{\eta_z}{|\ \mathbf{r}_a - \mathbf{r}_b\ |} \tag{4.25}$$

4.3.4 Resistance value

The hydraulic and electrical resistance at each point in the fracture $R_{i,j}$, was calculated as a weighted harmonic mean of the resistance of the fracture itself $R_{f\ i,j}$, and that of the surrounding matrix R_m:

$$\frac{\Delta z}{R_{i,j}} = \frac{b}{R_f} + \frac{\Delta z - b}{R_m} \tag{4.26}$$

where Δz is a fixed value representing the width of the fracture, and $R_{f\ i,j}$ is defined by Equations 4.6 and 4.8 for the hydraulic and electrical resistance respectively, using the corrected aperture from Sections 4.3.2 and 4.3.3. This Δz value is also used later (Section 4.3.5) to calculate the bulk hydraulic and electric properties of the fracture.

Taking a harmonic mean over a fixed width is necessary as it allows zero apertures to be handled without causing infinite resistance. For all models presented here, we have set Δz to be equal to the maximum fault aperture, b_{max}, down to a minimum of 0.1 mm. Setting Δz to b_{max} ensures that the minimum resistivity within any given fracture is equal to the fluid resistivity, and the maximum resistivity is the matrix resistivity. Likewise, the permeability in the fracture ranges from the matrix permeability to ${b_{max}}^2/12$. Choosing Δz to be some fixed value greater than b_{max} would reduce the resistivity and permeability at sections of the fracture with large apertures but have no effect on zero apertures. Conversely, setting Δz to less than b_{max} would effectively increase the electrical resistivity above the matrix value, and would reduce the permeability to below the matrix value, at small apertures. The minimum Δz value of 0.1 mm was set to avoid very high hydraulic and electric resistance for fractures with very small maximum apertures.

4.3.5 Modelling approach

In order to calculate the effective resistivity of the fracture, we followed the approach of Bahr (1997). A potential difference was applied from one end of the fracture to the other, with no current leaving or entering the sides. Kirchhoff's Law was applied in each node, and the electrical potential was assumed to sum to zero in each elementary cell.

Likewise, to calculate the effective permeability, a pressure difference was applied across the fracture, with no-flow boundary conditions set for the fracture sides. Mass was assumed to be conserved in each node and the pressure was assumed to sum to zero in each elementary cell.

Applying these boundary conditions, a series of equations was then constructed and solved to determine the current and fluid flow in each node. The resulting current and fluid flow through each end of the fracture was summed and used in Equations 4.1 and 4.3 together with the fixed potential and pressure difference and the Δz value (Section 4.3.4) to calculate an effective electrical conductivity and permeability for the fracture.

The resistor network approach implies that the electrical conduction pathways are independent of the absolute resistivities present but depend on their ratio. Therefore, we discuss the electrical conductivity of the fracture in terms of the ratio of the rock

matrix to fluid resistivity, defined here as m. Likewise, we define the ratio of the matrix to fracture resistivity as M.

4.3.6 Input parameters

A total of 760 different parameter combinations were modeled in order to identify the main controls on fluid and electrical current flow through a fracture. These include four different offset values between 0.0 and 10.0 mm. For each offset that was considered, 200 fractures were created, using different random number seeds to generate each fracture, in order to obtain a representative sample of models. The separation between the fracture surfaces was then varied, to simulate progressive opening of a fracture. To encompass the changes in resistivity and permeability as the fracture was opened, twenty different separation values were used. Each of these offset / separation pairs were modelled with m ranging from 3 to 3x10^4, using a matrix permeability of 10^{-18} m^2. In addition, the zero offset case was modelled over the 20 separation values with m equal to 1x10^4 and the matrix permeability equal to two different values; 10^{-16} m^2 and 10^{-14} m^2.

The fractal dimension of all of the fractures was set to 2.4, which corresponds to an elevation scale factor of about 1.9 $\times 10^{-3}$ (Figure 4.1). The mismatch wavelength cutoff for mismatch between the two surfaces was set to 1 mm. All fracture surfaces presented here are isotropic.

For the models presented here a cell size of 0.25 mm was used. Using this cell size, it was possible to adequately represent the mismatching behavior of the fractures which occurs over a wavelength of 1 to 10 mm (Figure 4.2), while at greater cell sizes this was not possible. Models were run on an 0.1 × 0.1 m fracture, or 400 × 400 cells.

4.4 Results

4.4.1 Base case

The base scenario we considered is a fracture with no offset, a matrix permeability of 10^{-18} m^2, and m equal to 10^4, which we modeled over 20 separation values. The results of modeling this scenario 200 times are presented in Figures 4.4 and 4.5.

Figure 4.4a shows the fracture permeability as a function of M. Figure 4.4b shows fracture permeability and electrical conductivity as a function of arithmetic mean aperture. For comparison, the results for a flat plate with an equivalent mean aperture, are also shown. Figure 4.5 shows the fluid and current passing through a fracture at two different separation values indicated by white stars and triangles in Figure 4.4.

The fluid and current behave similarly at low apertures, increasing gradually with aperture (Figure 4.4b). However, at an aperture of about 0.02 to 0.03 mm, the fracture reaches a percolation threshold, and both properties increase more rapidly. At this

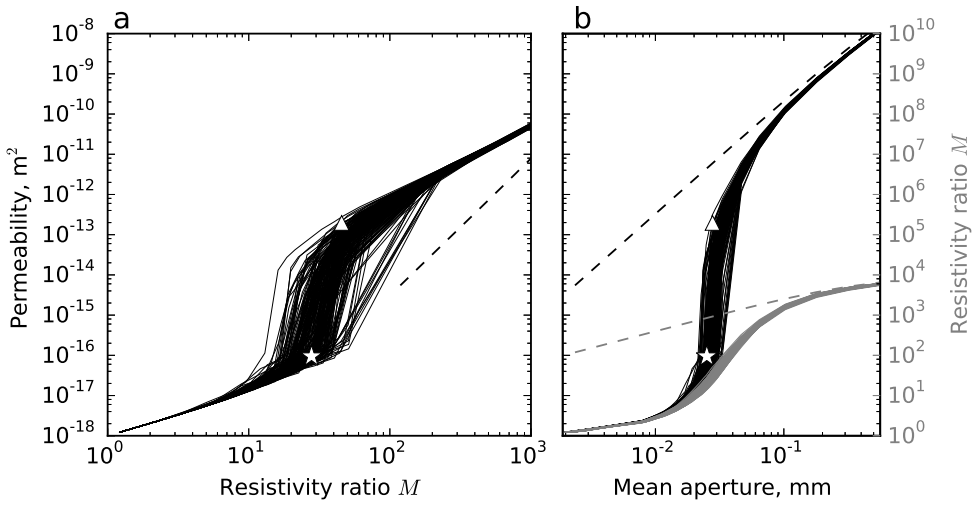

Figure 4.4: Changes in fracture conductivity (expressed in terms of the ratio M) and permeability as the fracture is opened, for fractures with no offset, within a matrix with permeability 10^{-18} m^2, with m equal to 10^4. (a) Permeability as a function of M. (b) Permeability (black) and M (grey) as a function of arithmetic mean fracture aperture. Position of percolation threshold and leveling off point for the fracture in Figure 4.5 indicated as white stars and triangles respectively. Dashed lines show the permeability and resistivity ratio m for a flat plate model with equivalent mean aperture.

point, permeability begins to increase rapidly, increasing by a factor of about 10^4 over a change in aperture of around 0.01 mm, while M increases by a factor of 5 over this change in aperture. The position of the percolation threshold is different for each of the 200 fractures shown in Figure 4.4, and this results in the spread observed in the percolation threshold curves. This is because each fracture is generated from a different random number seed, and therefore the fracture topograpy and the aperture distribution for each fracture is slightly different. Above a mean aperture of 0.03 mm, the permeability continues to increase, but at a lower rate. The ratio M levels off later, at a mean aperture of about 0.05 mm.

Permeability increases more rapidly than electrical conductivity at the percolation threshold, and therefore, the percolation threshold in permeability can be defined with respect to M. In the instance considered in Figures 4.4 and 4.5, the percolation threshold occurs where M is about 30. So here, a fluid-filled fracture that increases the electrical conductivity by a factor of about 30 increases the permeability by a small amount (to around 10^{-16} m^2), while an increase in the electrical conductivity by a factor of 50 corresponds to a high permeability (2×10^{-13} m^2). Both of these changes occur over a change in mean aperture of less than 0.01 mm.

The fracture shown in Figure 4.5a-c was separated by -0.006 mm (i.e. the surfaces were moved together) and is at the percolation threshold. The same fracture with a separation of 0.000 mm (Figure 4.5d-f) is above the percolation threshold. The mean aperture for each of these fractures is 0.025 and 0.028 mm respectively, and the percentage contact area between the two fracture surfaces (i.e. the percentage of the surface in which aperture is zero) is 53 and 49% respectively.

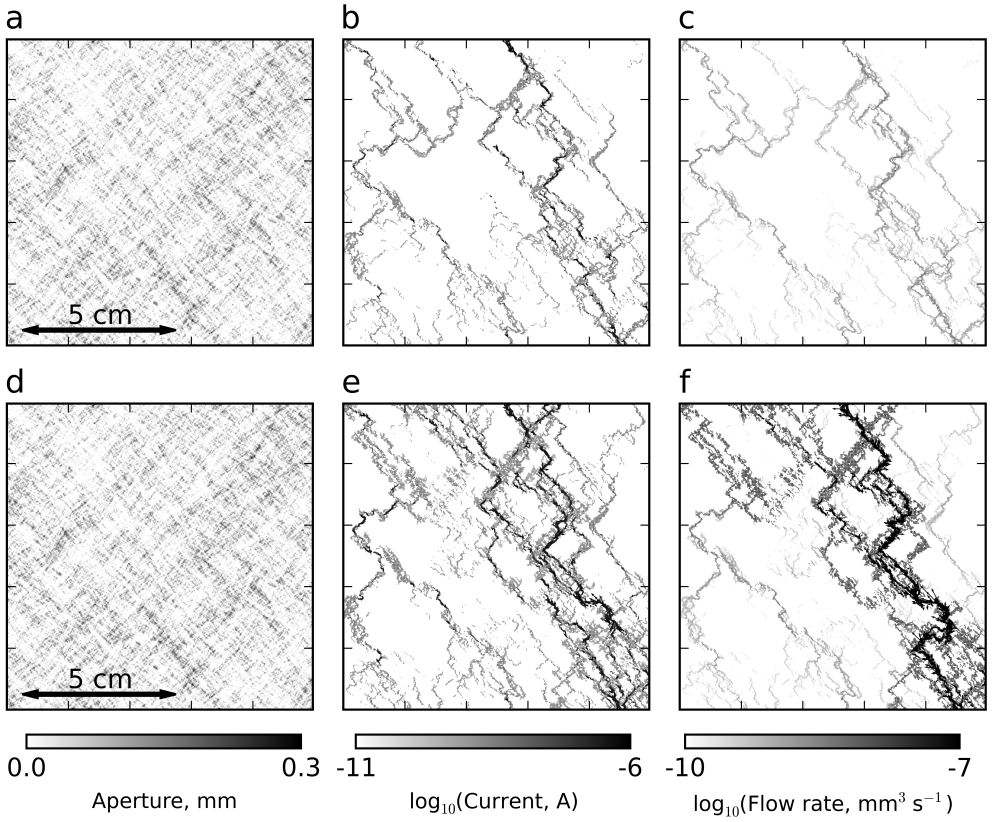

Figure 4.5: Fluid and current flow along a fracture with no horizontal offset but with two different separation values. (a) aperture distribution, (b) electrical current and (c) fluid flow for a fracture in which the fault surfaces have been separated by -0.006 mm. This fracture is at its percolation threshold. (d) aperture distribution, (e) electrical current and (f) fluid flow for a fracture with a separation of 0.000 mm. This fracture is above its percolation threshold.

These examples demonstrate the strong differences in electrical current and fluid flow that occur over this small change in aperture. In Figure 4.5a–c, there is minimal current and fluid flow, and the bulk permeability of the fracture is low (10^{-16} m^2), while M is equal to 28. In Figure 4.5d–f, the fluid and current flow is considerably greater, due to the fracture becoming connected along the right hand side. The permeability of the fracture is over three orders of magnitude greater than in the first scenario at 2.0×10^{-13} m^2, while M is a factor of 1.6 greater, at 46. This supports the concept that the permeability and resistivity of the fracture is strongly controlled by the distribution of void space, and at the percolation threshold, the connectivity at a specific point in the fracture, the location of which varies depending on the pore space distribution of that individual fracture, controls the permeability of the whole fracture. These observations are consistent with those of previous authors (e.g., Brown, 1989).

In the following sections we investigate the effect of changing different attributes of both the fracture and the rock matrix on the percolation behavior that is observed, and in particular the position of the percolation threshold with respect to the ratio M.

4.4.2 Matrix and fluid properties

Fluid flow and electrical current were modeled through fractures with m ranging from 3 to 3×10^4. The permeability – resistivity relationship for these models is shown in Figure 4.6.

Increasing the matrix permeability simply raises the starting permeability of the fracture at smaller apertures; above the percolation threshold, the dependence of the relationship between resistivity, permeability and aperture on the matrix permeability is minimal.

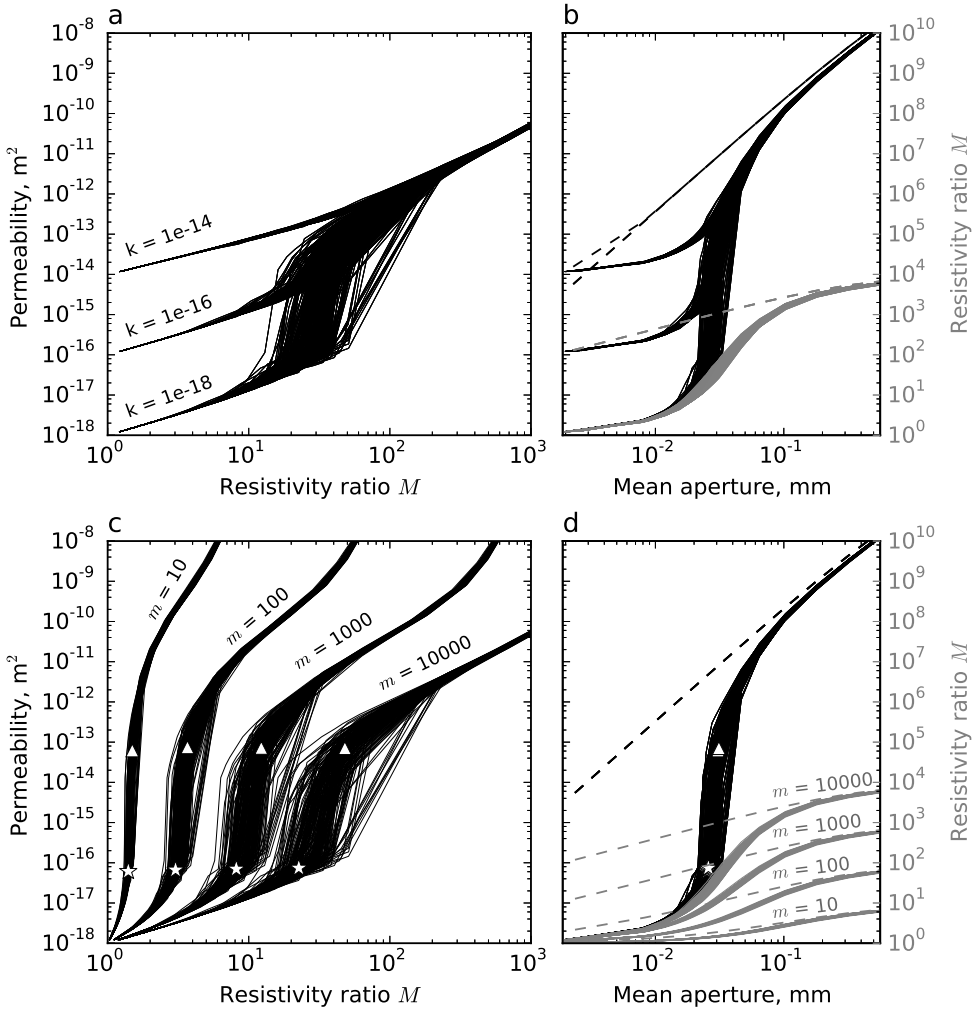

Figure 4.6: Changes in M and permeability as a fracture is opened for rough fractures with no offset. (a) Permeability as a function of M and (b) permeability and M as a function of arithmetic mean fracture aperture for matrix permeability values of 10^{-14} m^2, 10^{-16} m^2, and 10^{-18} m^2. (c) Permeability as a function of M and (d) permeability and M as a function of arithmetic mean fracture aperture for m equal to 10, 100, 1000, and 10000. Stars indicate the percolation threshold, and triangles indicate the leveling off point, as described in the text.

As might be expected, an increase in m corresponds to an increase in the matrix to fracture resistivity ratio at the percolation threshold, M_{PT}. However, with increasing m, M_{PT} decreases strongly as a proportion of m. Where m is equal to 100, M_{PT} equals about 4, i.e. 4% of m. Where m is equal to $3{\times}10^4$, M_{PT} is about 60, only 0.2% of m. This reflects a decrease in the contribution of the matrix conductivity to the passage of current through the fracture. As m increases, less current passes through the matrix and therefore the conductivity of the fracture is more strongly controlled by the fracture aperture distribution.

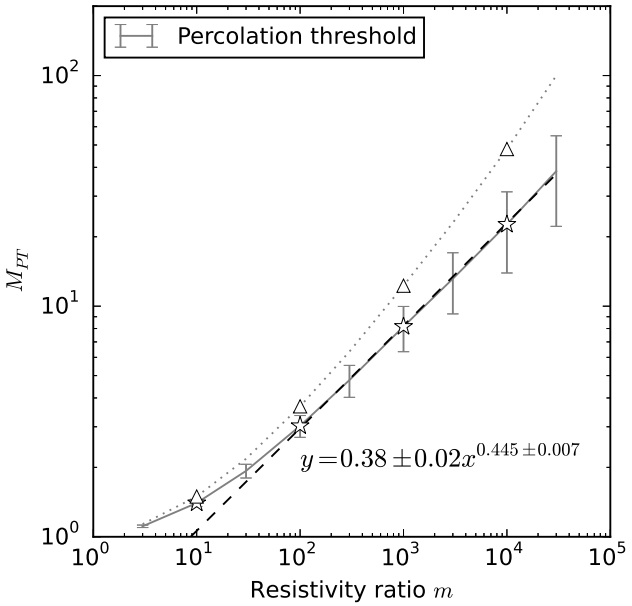

Figure 4.7: Percolation threshold location M_{PT} as a function of matrix to fluid resistivity ratio for fractures with no offset, contained within a matrix with a permeability of 10^{-18} m^2, with m ranging from 3 to $3{\times}10^4$. The percolation threshold is indicated by a grey line, with the error bars indicating the standard deviation. The leveling off point is indicated by the dotted black line. The stars and triangles correspond to the percolation thresholds and leveling off points in the examples shown in Figure 4.6c and d. The dashed line and corresponding equation is a line of best fit for the points with a matrix to fluid resistivity ratio greater than or equal to 100.

In order to numerically analyze how M_{PT} varies with m, we have applied a systematic method to calculate the percolation threshold location as well as the point at which permeability levels off with respect to both resistivity and aperture. First, we interpolated the fracture resistivity values (and corresponding permeability values) onto regular intervals in log space, allowing changes in the gradient to be defined more precisely. We then calculated the second derivative of the resistivity – permeability curve. Typically, this produced positive peaks, with the first peak corresponding to the percolation threshold. There are also several negative peaks with the final one corresponding to the leveling off point. To pick these points automatically we selected the

first point on the curve with the second derivative greater than 20 % of the maximum (percolation threshold), and the last point in the curve with the second derivative less than 20 % of the minimum (leveling off point).

The median and standard error in M_{PT}, and the median leveling off point, are plotted against m in Figure 4.7. Where $m \geq 100$, M_{PT} appears to follow a straight line relationship with respect to m on a log-log plot. Fitting a line to all points where $m \geq 100$ produces the following power law relationship between M_{PT} and m (Figure 4.7):

$$M_{PT} = (0.38 \pm 0.02) m^{0.445 \pm 0.007} \tag{4.27}$$

Where $m < 100$, the slope decreases below that in Equation 4.27. This is because M must equal 1 where m equals 1.

4.4.3 Fault offset

As discussed in Section 4.2.5, fault offset scales with fault length, generally reaching up to about 10 % of the fracture length (Kim and Sanderson, 2005). For our fracture of dimensions 100 mm × 100 mm, we have used offsets of up to 10 mm. We introduced offset between the surfaces by shifting the top surface in the direction perpendicular to that in which fluid flow and current was to be modeled (Figure 4.3).

Figure 4.8 shows that increasing the offset between the two fault surfaces increases the aperture at which the percolation threshold occurs in both the resistivity and permeability. If there is no offset, the percolation threshold occurs at a mean aperture of ~0.025 mm. If the offset is 10 mm, the percolation threshold occurs at a mean aperture of ~0.25 mm. However, because the offset affects both the resistivity and permeability, the percolation threshold location in the permeability – resistivity curve varies to a lesser degree with offset (Figure 4.8a). For m equal to 10^4, M_{PT} is equal to 25 if there is no offset, increasing to 50 if there is 0.5 mm of offset, and decreasing down to 17 for 10 mm of offset (Figure 4.9). Above the percolation threshold, increasing the offset results in permeability leveling off later with respect to M (Figure 4.8a). As a result, the permeability at the leveling off point is two orders of magnitude greater for a fault with 10 mm offset than one with 1 mm offset (Figure 4.8a). The percentage contact area between the two fault planes, both at and immediately above the percolation threshold, varies by less than 1 % for different offset values. It is, on average, 50 % at the percolation threshold and 55 % at the leveling off point.

When there is offset between the two fault surfaces, the relationship between M_{PT} and m deviates from the simple power law relationship exhibited by faults with no offset (Figure 4.9). Faults with offsets of 0.5 mm are associated with an increase in M_{PT} for all values of m, however as offset increases above 0.5 mm, M_{PT} decreases, and is, for an offset of 10 mm and $m > 10^4$, lower than M_{PT} for a zero offset fault (Figure 4.9).

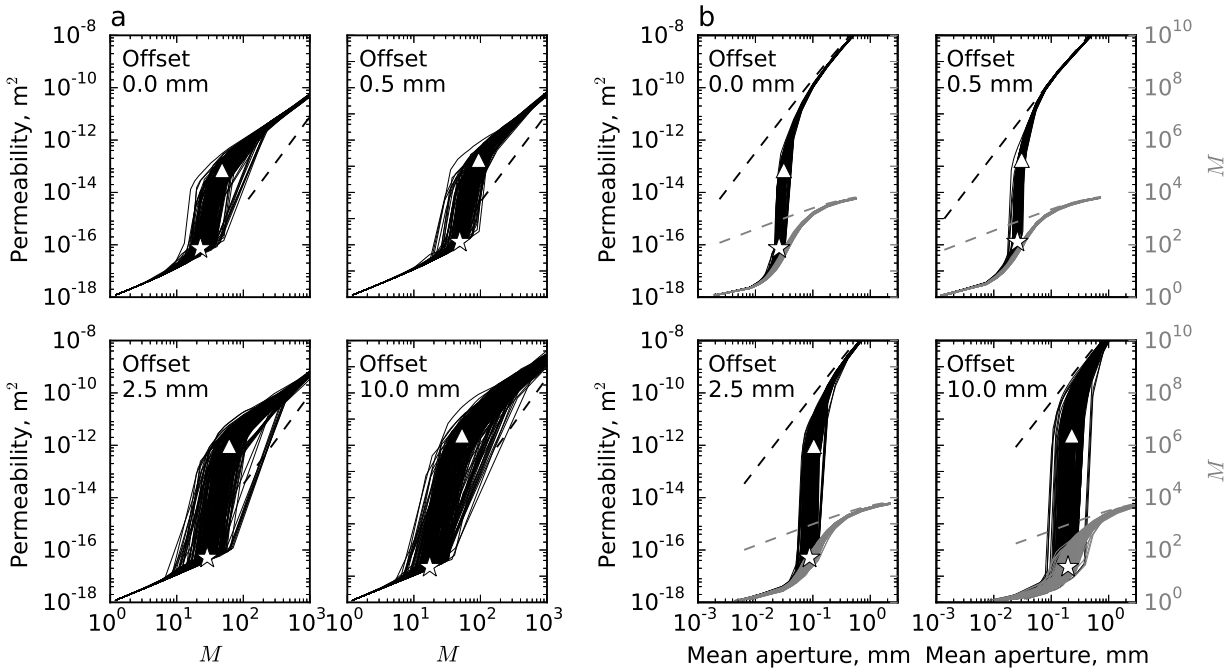

Figure 4.8: Changes in M and permeability as a fracture is opened, for faults with offsets of 0.0, 0.5, 2.5, and 10.0 mm. The matrix permeability is 10^{-18} m^2 and m is equal to 10^4. Dashed lines show the permeability and resistivity of a flat plate model with equivalent mean aperture, and stars and triangles indicate the median percolation threshold and leveling off point respectively. (a) Permeability and matrix to fracture resistivity as a function of arithmetic mean aperture. (b) Permeability as a function of matrix to fracture resistivity ratio.

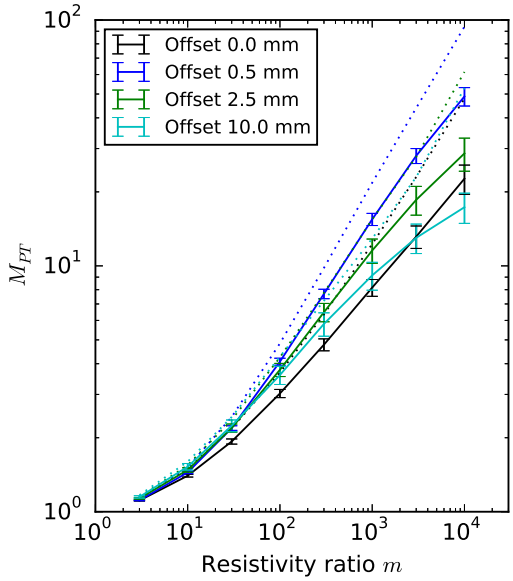

Figure 4.9: Changes in M_{PT} (solid lines) as a function of matrix to fracture resistivity ratio for faults with offsets of 0.0, 0.5, 2.5, and 10 mm with matrix permeability equal to 10^{-18} m^2. Error bars indicate the standard error, and dotted lines indicate the leveling off point.

4.4.4 Fault spacing

So far we have considered the electrical properties of a single fault. However, a more realistic scenario is a faulted rock volume. Therefore, we extend the aforementioned concept in order to model a rock volume, with variable width (perpendicular to the fault plane), containing a single fault. Changing the width of the rock volume is equivalent to changing the spacing between faults.

We adjust the width of the rock volume by correcting both the permeability and the resistivity values observed in Section 4.4.1. The effective electrical resistivity of a medium of width G with a single fault through it can be approximated by the weighted harmonic mean of the conductivity of the fault and that of the surrounding rock. Since the width of the fault Δz has been defined as the maximum fault aperture b_{max} (Section 4.3.4), the resistivity $\rho_{F,G}$ of a fractured rock of width G, along the direction of the fracture, is a function of the resistivity of the fracture ρ_F:

$$\frac{G}{\rho_{F,G}} = \frac{b_{max}}{\rho_F} + \frac{G - b_{max}}{\rho_m} \tag{4.28}$$

From this, an expression can be derived for the ratio of the matrix to fractured volume resistivity, M_G:

$$M_G = \frac{b_{max}}{G}(M - 1) + 1 \tag{4.29}$$

The permeability $k_{f,G}$ along the fault, averaged across width G is a weighted arithmetic mean of the matrix and fault permeabilities k_m and k_f:

$$k_{f,G} = \frac{b_{max}k_f}{G} + \frac{(G - b_{max})k_m}{G} \tag{4.30}$$

Equations 4.29 and 4.30 have been used to calculate the hydraulic and electrical properties of volumes with widths of 1, 10 and 100 mm. The resistivity – permeability behavior and the location of the percolation threshold are shown in Figures 4.11a and b. In addition, bulk properties have been calculated for faults with offsets ranging from 0 to 10 mm, averaged across a volume with width 10 mm (Figure 4.10). Figure 4.10 also shows the permeability at the percolation threshold and at the leveling off point.

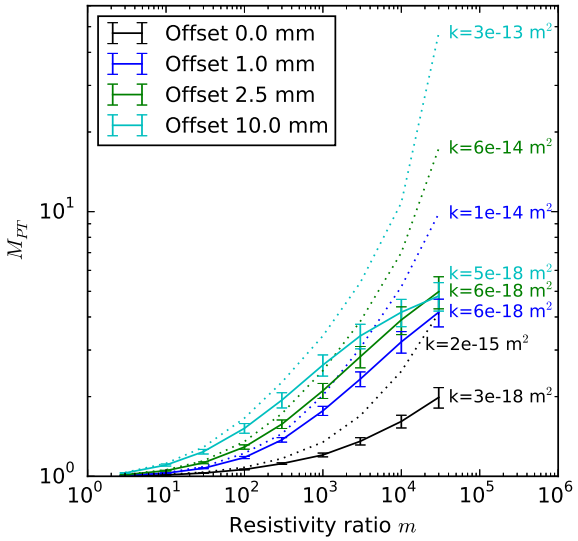

Figure 4.10: The ratio M_{PT} (solid lines) and leveling off point (dotted lines) as a function of m for faults with offsets of 0.0 mm (black), 0.5 mm (blue), 2.5 mm (green), and 10 mm (cyan). Matrix permeability is equal to 10^{-18} m^2, fault spacing is fixed at 10 mm. The permeability values at the percolation threshold and leveling off point are labelled. Error bars indicate standard error.

Both the permeability and M_{PT} vary inversely with fault spacing, and therefore increasing the spacing by an order of magnitude corresponds to a decrease in each of these properties by an order of magnitude. However, M_{PT} generally varies by only one or two orders of magnitude over the range of apertures considered here, while permeability varies by up to ten orders of magnitude. Therefore, the permeability is less affected by increasing the spacing than the resistivity.

The value of M_{PT} is strongly affected by fault spacing. For the example shown in Figure 4.11b, a fault spacing of 1 mm is associated with M_{PT} ranging from 1 to 15, depending on m. However, once the spacing is increased to 10 mm, the maximum value of M_{PT} is just over two, and if the spacing is increased to 100 mm, M_{PT} reaches a maximum of less than 1.1.

Figure 4.10 shows that increasing fault offset increases M_{PT} for a given spacing. However, the greatest increases occur at small fault offsets. As fault offset increases above about 1 mm, M_{PT} is less sensitive to increases in offset.

Offset has a greater effect on the resistivity above the percolation threshold. Both the resistivity and permeability at the leveling off point increase with increasing fault offset (Figures 4.11b and 4.10).

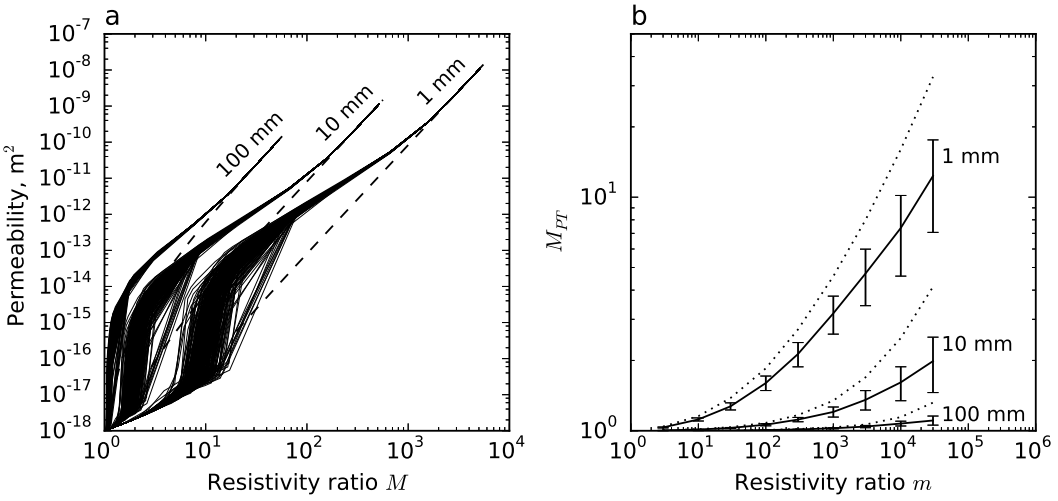

Figure 4.11: Changes in M as a fracture is opened for fractures spaced varying widths apart within a rock matrix with a permeability of 10^{-18} m^2. Dashed lines show the permeability and resistivity of a flat plate model with equivalent mean aperture. (a) Permeability as a function of M for fractures with no offset spaced 1 mm, 10 mm and 100 mm apart, with m fixed to 10^4. (b) Percolation threshold location (solid line), and leveling off point (dotted line), as a function of matrix to fluid resistivity ratio for fractures with no offset, for faults spaced 1 mm, 10 mm and 100 mm apart, with error bars indicating standard deviation.

4.5 Discussion

We have presented models of faults as resistor networks to explore the relationship between electrical and hydraulic conductivity in fractured rocks. The results confirm the observations of Ishibashi et al. (2015) and Brown (1989) that fluid flow in fractures depends strongly on the aperture distribution, and that variations in aperture along a fault plane lead to fluid and current channeling, which are not necessarily coincident.

Further to these observations, our models explore the changes in the resistivity and permeability of a fault as it opens. As the fault separation increases, the electrical and hydraulic conductivity both increase, initially at a similar rate. However, once the fault reaches its percolation threshold, both properties increase more rapidly. The permeability increases by at least three orders of magnitude over changes in aperture of less than 0.1 mm (less than 0.01 mm for faults with offsets of 0.5 mm or less). On the other hand, the electric conductivity only changes by up to one order of magnitude over this aperture change, depending on the ratio of matrix to fluid resistivity, m. The difference in the behavior at the percolation threshold allows the percolation threshold to be defined in terms of electrical resistivity, which can be expressed as the ratio of matrix to fracture resistivity, M_{PT}.

Figure 4.12 shows a physical interpretation of the processes occurring during incremental separation of two rough fracture surfaces. In Zone 1, the fracture is closed such that the void space only exists in isolated pockets. If the matrix were impermeable and non-conductive, these isolated patches would not contribute to either electrical

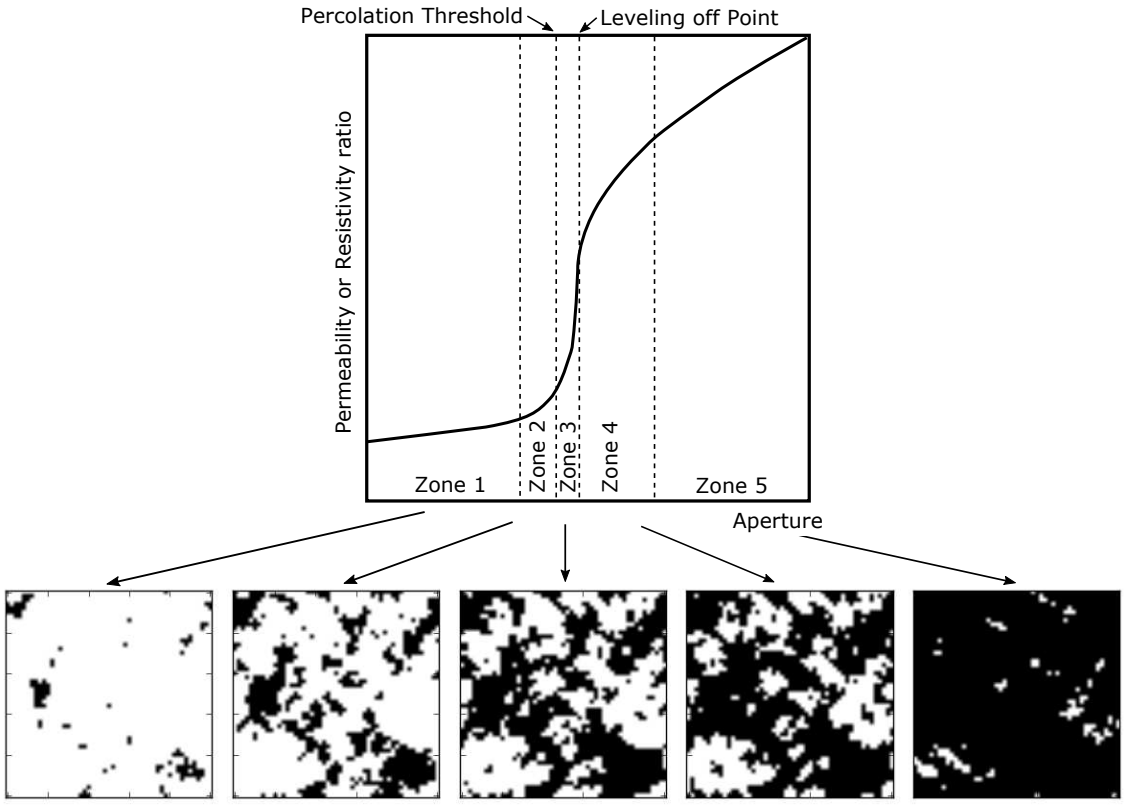

Figure 4.12: The development of the transport properties of a rough fracture embedded in a low permeability and electrical conductivity matrix as a function of the incremental separation of the fracture surfaces.

conduction or fluid flow. However, here there is a matrix conductivity and permeability, which implies the system has a small finite permeability and conductivity. Increases in separation between the two fracture surfaces result in only small increases in the conductivity and permeability because the fluid and current has to pass through large portions of matrix.

As the fault surfaces are separated further, there comes a point where isolated patches of void space begin to link up such that fluid flow and electrical conduction is mainly within these patches, with only a few barriers to electrical conduction and fluid flow (Zone 2).

Zone 2 ends at the percolation threshold, which marks the development of the first continuous flow and conduction pathway through the fracture. This is Zone 3: the distributary zone where flow is distributed amongst many branches of cross-cutting pathways that have developed as the fracture surfaces separate. In this zone, the rate of increase in permeability and conductivity depends on the addition of new pathways. Eventually, the fracture becomes almost completely connected and the rate of increase in permeability and conductivity decreases. This is the leveling off point, which marks the end of Zone 3.

Zone 4 begins at the leveling off point. Here, the fracture permeability and conductivity is controlled primarily by the distance between the plates, but also from the removal of any remaining surface contact. By Zone 5, variations in the aperture have become small compared to the aperture itself, and the permeability and conductivity approaches a parallel plate model.

The differences in the physical processes of electrical conduction and fluid flow lead to differences in the positioning of the boundaries between the zones for each process. In the case of fluid flow, the boundary is sharp. Consider a fractured volume of width 1 mm, with a matrix permeability of 10^{-18} m^2 and m equal to 3×10^4. Applying Equations 4.1 and 4.5, the aperture needed for the fluid flow through the fracture to equal that in the surrounding matrix at any given point in the fracture is about 0.2 μm. By an aperture of 1.1 μm there is 100 times more fluid passing through the fracture than the matrix. The corresponding apertures for electrical current are 0.03 and 3.3 μm respectively. So the transition from Zone 2 to Zone 3 should occur at a different point, and over a different fault separation range, for electrical conduction and fluid flow. This is indeed the case when we consider Figures 4.4 and 4.6. The point at which the conductivity increases most rapidly is different for different values of m and doesn't necessarily coincide with the maximum rate of change of the permeability. This difference in the timing of the two processes leads to the relationship between m and M_{PT} shown in Figure 4.7.

For both fluid flow and electrical conduction the difference in mean fault aperture is very small across the percolation threshold, varying in both cases by less than 0.1 mm. However the electrical and hydraulic properties vary strongly. Therefore, small changes in the local stress field in an area, for example, may be enough push fractures over their percolation threshold, leading to large changes in both the resistivity and the permeability. As such, areas that are in similar geological settings may have strong differences in both the electrical and hydraulic properties, resulting not from lithological differences but from differences in the local structure and/or stress field. Such differences in the electrical and hydraulic properties may even occur temporally due to changes in the stress field resulting from earthquakes. These differences may be detectable as changes in resistivity using techniques such as MT that are sensitive to not only the resistivity but also variations in resistivity with orientation.

The ratio M is inversely related to fault spacing. For the faults considered here, if the average spacing is greater than about 0.1 m, M_{PT} is always between 1 and 1.2 (Section 4.4.4). However, if the average spacing is 10 mm, M_{PT} is up to 5, depending on m and the offset on the fault.

The amount of offset between the two fault surfaces also influences M_{PT} (Section 4.4.3). The ratio M_{PT} increases for faults with small offsets (Figure 4.9). For m equal to 10^4, M_{PT} increases by a factor of 2 from zero to 0.5 mm offset. However, once the offset increases above 0.5 mm, M_{PT} begins to decrease. At 10 mm of offset, M_{PT} is two thirds of that for a fault with no offset.

When averaged over a volume of fixed width, the fault permeability and resistivity shows a different relationship with offset. This is because as offset increases, the mean

fault aperture increases. Therefore, faults with smaller offsets are more strongly affected by the volume averaging than faults with larger offsets that take up a greater volume, so faults with greater offsets decrease the resistivity of the volume by more. However, once the faults reach an offset of 0.5 mm or more the effect of increasing offset begins to reduce.

These results suggest that smaller faults are likely to have a stronger effect on the resistivity at the percolation threshold than larger faults. Fault spacing, offset and size are correlated (e.g., Bonnet et al., 2001); i.e., faults with greater offset are likely to be larger and more widely spaced than those with small offsets. However, the strongest decreases in resistivity occur with smaller offsets. For example, for m equal to 10^4 and a fault spacing of 10 mm, an increase in offset between 0 and 1 mm results in an increase in M_{PT} by a factor of about 50 %. However, increasing the offset from 1 mm to 20 mm only increases M_{PT} by a further 25 %. In contrast, halving the spacing increases M_{PT} by more than 70 %. Consider a rock volume containing 10 mm long fractures with 1 mm offset each, spaced 10 mm apart. In this case, M_{PT} equals about 3.3. In contrast, 100 mm fractures with 10 mm offset each, spaced 100 mm apart, correspond to M_{PT} equal to about 1.3.

Above the percolation threshold, the relationship between resistivity, permeability and fault aperture is different. Figure 4.10 shows that, as offset increases, both permeability and resistivity increase by more at the percolation threshold. If we consider the faults in the example above but at the leveling off point on the resistivity-permeability curve, those with 1 mm of offset and spaced 10 mm apart will decrease the resistivity by a factor of about 5.5, while those with 10 mm of offset decrease the resistivity by a factor of about 3.1.

In all the cases considered here, M_{PT} is almost always less than 10. In many cases it is very close to 1, which means the fracture is only enhancing the electrical conductivity by a very small amount. In order to enhance the conductivity of a fluid-filled fractured volume by a factor of more than 10, as inferred by MacFarlane et al. (2014) and Kirkby et al. (2015), the fractures must be above their percolation threshold. The modelling presented here suggests that if such conductivity enhancement is present, the fractures will also be open for fluid flow.

4.6 Conclusion

Through models of random resistor networks we have explored the relationship between electrical resistivity and permeability in fractures filled with an electrically conductive fluid. A percolation threshold can be defined for these in terms of the resistivity of the fault. At the percolation threshold, very small changes in aperture are associated with large changes in both the resistivity and permeability of the fault. The position of this threshold depends on the rock and fluid resistivity, and properties of the fracture (in particular, offset and spacing). Decreased spacing, increased offset and an increased rock to fluid resistivity ratio all increase the resistivity ratio at the percolation threshold. In the majority of geologically likely scenarios, the resistivity ratio at

the percolation threshold is less than about 10, and it is often closer to 1. Therefore, if a higher ratio than this is observed and can be attributed to the presence of fluid-filled fractures, then it is likely that the fractures are above their percolation threshold and open for fluid flow.

CHAPTER

FIVE

THE RESISTIVITY AND PERMEABILITY OF 3D FRACTURE NETWORKS

Alison Kirkby[1,2]

[1] Electrical Earth Imaging Group, School of Physical Sciences, University of Adelaide, Adelaide, SA 5000, Australia
[2] Geoscience Australia, Canberra, ACT 2601, Australia

Statement of Authorship

Title of Paper	The resistivity and permeability of 3D fracture networks
Publication Status	☐ Published ☐ Accepted for Publication ☐ Submitted for Publication ☑ Unpublished and Unsubmitted work written in manuscript style
Publication Details	

Principal Author

Name of Principal Author (Candidate)	Alison Kirkby
Contribution to the Paper	Developed conceptual framework, modelling technique, wrote the modelling code. Carried out the modelling and wrote the manuscript
Certification:	This paper reports on original research I conducted during the period of my Higher Degree by Research candidature and is not subject to any obligations or contractual agreements with a third party that would constrain its inclusion in this thesis. I am the primary author of this paper.
Signature	Date 18/8/16

SUMMARY

The resistivity and permeability of 3D fracture networks have been modelled as the fractures within these networks are incrementally opened. In these models, the ratio of the rock resistivity to that of the fluid is 10^4. The changes in both resistivity and permeability depend on characteristics of the network itself such as fault density, as well as the aperture distribution within individual faults. In dense fault networks where the density constant α is equal to 30, a percolation threshold can be defined in terms of mean fault aperture, below which both resistivity and permeability are close to their matrix values. At the percolation threshold, a change in mean aperture of 0.02 mm can change the permeability by four orders of magnitude and resistivity by a factor of four. The percolation threshold does not necessarily occur at the same aperture for different flow directions, so fault networks near their percolation threshold commonly show anisotropy in both resistivity and permeability. Most sparse networks (α equal to 0.3 or less) do not percolate no matter how open the faults are. On the other hand, many fault networks with an intermediate value of α (equal to around 3) will percolate only in one or two directions. This can lead to very strong anisotropy in both resistivity and permeability (up to a factor of 160 and 10^9 respectively), with anisotropy increasing as the aperture of the fractures increases.

5.1 Introduction

Fracture permeability is vital to the successful development of many unconventional energy resources. These resources are often located at several kilometres depth, where compaction and cementation processes can remove much of the primary permeability (e.g. Barton et al., 1997; Cumming, 2009). Exploration of fracture permeability, however, is not straightforward. Permeability can vary by orders of magnitude over length scales of kilometres to metres, making it difficult to target enhanced permeability zones from the surface.

Electrical resistivity has long been used to infer the porosity of rocks, for example in Archie's Law, a widely used empirical relationship that relates resistivity to porosity and water saturation in a rock with high background resistivity (Archie, 1942). Variants of Archie's Law exist, including to account for non-negligible surface conduction (e.g. Tiab and Donaldson, 2012) or for multiple fluid phases (e.g. Glover, 2010). The porosities can then be empirically related to permeability. However, Archie's Law was developed for porous rocks with high primary permeability, and may not be relevant for low porosity, fractured rocks.

The magnetotelluric (MT) method is sensitive to changes in the subsurface resistivity both spatially and with orientation. It has been shown to have merit in detecting resistivity changes due to both addition of electrically conductive fluids in an enhanced

geothermal system (e.g. Peacock et al., 2012, 2013; Rosas-Carbajal et al., 2015) and more recently, hydraulic stimulation of a shale gas prospect (e.g. Rees et al., 2016a,b). In both examples, the addition of fluids were associated with increases in permeability along the fracture network. However, quantitatively linking the resistivities to permeability has not yet been possible.

Kirkby et al. (2016) modelled the resistivity and permeability of individual synthetic fractures, allowing a link to be made between the two properties. The fractures were generated based on measured characteristics in rock surfaces. The modelling was carried out at various points as the fractures were incrementally separated, providing information on the evolution of both resistivity and permeability as a fracture is opened.

Both the permeability and resistivity of the fractures were shown to demonstrate percolation behaviour. At low apertures, fluids are only present in isolated pockets, and both the permeability and resistivity are close to the rock matrix values. However, as the fracture is opened, the void space becomes more connected, eventually reaching its percolation threshold, when a fully connected pathway through the fracture develops. At this point, both the permeability and resistivity increase rapidly. The modelling showed that in order to have substantial resistivity (greater than a factor of 2) and permeability (greater than one order of magnitude) enhancement from fractures, it is necessary that the fracture is at or over its percolation threshold, confirming results from previous studies (e.g. Bahr, 1997). The modelling also demonstrated the percolation threshold in terms of measurable fracture parameters such as the separation between the fracture planes. The change from below to above the percolation threshold occurs over an aperture change of < 0.1 mm. Thus, very small changes in the fracture aperture can lead to large changes in both resistivity and permeability of a fracture.

One limitation of the work of Kirkby et al. (2016) is that it was carried out on individual fractures and not fracture networks. Thus, it is difficult to directly relate the results to resistivities and permeabilities that might be observed in the subsurface. There are empirical relationships that relate the spacing, size, and offset of faults within networks (e.g. Bonnet et al., 2001; Kim and Sanderson, 2005). These could be used to build on the work of Kirkby et al. (2016) to gain a more complete understanding on the effect fracture networks have on the resistivity and permeability values that are measured in the subsurface.

In this paper, we build on the work of Kirkby et al. (2016) by modelling the electrical and fluid flow properties of synthetic fracture networks in rocks. Fault networks are constructed based on established relationships between fault spacing, size and offset. Each fracture within the network is constructed based on characteristics measured in real rock fractures. As with Kirkby et al. (2016), the resistivity and permeability of each of these fracture networks is evaluated at several points as the aperture of the fractures within the network is incrementally increased.

5.2 Background

5.2.1 Resistor networks

The approach used in this work is based on the resistor network approach used by Bahr (1997). Electrical current and fluid flow is assumed to occur through a network of resistors. In the approach of Bahr (1997), the resistors were assumed to either be perfect conductors or insulators. Kirkby et al. (2016) developed this concept further by taking the resistance of each resistor to be related to the local fault aperture, and, in the case of resistivity, the conductivity of the fill material. A potential difference is then simulated and used to determine the electrical current passing through the network. This current distribution is then used in conjunction with the potential difference to calculate the bulk resistivity. Likewise, a pressure gradient is applied across the network to determine the fluid flow distribution, which is then used to calculate the permeability.

5.2.2 Hydraulic and electric resistance in fractures

The electrical resistance at each point in the fracture, R_E, is related to the local current I and the electrical potential v via Ohm's Law (Brown, 1989; Kirkby et al., 2016):

$$I = \frac{1}{R_E} \nabla v \tag{5.1}$$

Where

$$R_E = \frac{\rho_f \Delta z}{A} = \frac{\rho_f \Delta z}{b \Delta y} \tag{5.2}$$

Where ρ_f is the fluid resistivity, A is the cross sectional area perpendicular to flow, b is the fracture aperture, Δz is the cell size in the direction of flow, and Δy is the cell size perpendicular to both the flow direction and the fracture opening direction (Brown, 1989; Kirkby et al., 2016).

Likewise, the permeability k is related to the local fluid flow rate Q and the pressure p through Darcy's Law:

$$Q = \frac{kA}{\mu} \nabla p \tag{5.3}$$

Where μ is the fluid viscosity. Fluid flow in fractures is commonly approximated by the local parallel plate model, in which the fracture surfaces are assumed, locally, to be flat and parallel. The steady state solution of the Navier-Stokes equations for laminar fluid flow leads to a cubic dependence of fluid flow on aperture (e.g., Witherspoon et al., 1980; Brown, 1989):

$$Q = -\Delta y \frac{b^3}{12\mu} \nabla p \tag{5.4}$$

From Equations 5.3 and 5.4 we obtain the permeability as $b^2/12$ and the local hydraulic resistance, R_H, as:

$$R_H = \frac{12\mu\Delta x}{l_y b^3} \tag{5.5}$$

The local parallel plate model for fluid flow can be extended to non-parallel, sloping plates through a correction factor derived by Brush and Thomson (2003). The correction is based on the Navier-Stokes solution for fluid flow in a wedge, and also corrects for extra path length resulting from sloping plates. It was shown to provide a good approximation to the full Navier-Stokes solutions at the low flow velocities likely to be encountered in the subsurface (Brush and Thomson, 2003). This correction was used by Kirkby et al. (2016) who developed and applied an equivalent correction for electrical aperture.

5.2.3 Scaling in fault networks

Bonnet et al. (2001) reviewed relationships in the scaling between fault length, spacing, displacement, and aperture in natural fault networks. The authors concluded that power law distributions are the most widely applicable models for characterising the size distribution of most fracture systems, although in some cases (for example, where there is horizontal bedding), exponential or lognormal distributions may apply (Odling et al., 1999).

Assuming a power law distribution, the number of fractures per area R^2, $N_{f,2D}$, can be modelled as:

$$N_{f,2D} = \int_{l_{min}}^{l_{max}} \alpha l^{-a} R^2 dl = \frac{\alpha}{a-1}(l_{min}^{1-a} R^2) \tag{5.6}$$

(Bonnet et al., 2001). The constant α and exponent a are determined empirically. The truncation length, l_{min}, is usually assumed to be the length of the smallest observed fault. In practice, this length depends on the resolution, which depends on the method and scale of observation. Bonnet et al. (2001) presented a compilation of the characteristics of natural fracture networks from 45 separate studies. The faults range in length from the core scale (~ 3 mm to 1 m scale) to the aerial photo/seismic scale (~ 10 m to 100 km).

The number of faults in a particular length range within a given area is then given by

$$N_{f,2D} = \frac{\alpha}{a-1}(l_{min}^{1-a} - l_{max}^{1-a}) R^2 \tag{5.7}$$

Bonnet et al. (2001) presented α and a values calculated from the 45 natural fault networks included in the review. All of the presented fault networks were calculated from 2D areas, i.e. in cross section or from maps.

There is a moderately high degree of scatter in observed values of a. The exponent a ranges from 1.3 to 3.3 with most values clustering within the 1.75 – 3.0 range. However, of the 45 studies in the compilation, only six were calculated for fault lengths that extend down to 1 m or less (Reches, 1986; Bahat, 1987; Knott et al., 1996; Schlische et al., 1996; Ackermann and Schlische, 1997), and in all but one of these, a falls within the range 2.0 – 2.75.

The constant, α, shows an even higher degree of scatter, ranging from 10^{-5} to 100, although it broadly decreases as the fault network area increases. Of the six presented studies that include fault lengths < 1 m, α ranges from around 0.3 to just under 100, with a median of approximately 3.

Both a and α were calculated from 2D fault distributions (Bonnet et al., 2001). Given that the fault networks in this study are 3D, equivalent values for 3D need to be calculated. Synthetic tests were carried out by generating 3D fault networks and then analysing the fault length distribution of 2D slices intersecting them. These tests showed that the equivalent value of a for 3D can be obtained by adding 1 to a (2D). The value of α is the same in 3D as it is in 2D, however the area R^2 becomes a volume (R^3). As such, the number of faults in a volume R^3, $N_{f,3D}$ is given by:

$$N_{f,3D} = \frac{\alpha}{a}(l_{min}^{-a} R^3) \tag{5.8}$$

5.2.4 Fracture aperture

Both the hydraulic and electrical resistance in each fracture plane in the fault network depend on the aperture distribution within that fracture plane (Section 5.2.2). Thus, it is important to accurately model the aperture distribution in order to adequately represent these two properties.

Fracture surfaces have power spectral densities of the form

$$G(f) \propto f^{-\alpha} \tag{5.9}$$

where G is the power spectral density, f is the spatial frequency and α is related to the fractal dimension D through (Brown, 1987)

$$\alpha = \frac{7 - D}{2} \tag{5.10}$$

Fractal dimension ranges from about 2.2 to 2.6 in rock fractures (e.g., Brown, 1995; Glover et al., 1998b; Matsuki et al., 2006; Ishibashi et al., 2015). Brown (1995) used this

relationship to develop an algorithm for generating self-similar fracture surfaces, which uses the inverse Fourier transform to generate fractures with power spectral density functions described by Equations 5.9 and 5.10. The phase of each Fourier component was scaled by a random number between zero and one, in order to replicate the random phase spectra that has been observed in natural rock fractures (Brown, 1995).

The random phase can be used to develop mismatching between two opposing fracture surfaces on different length scales. If the random phase components are the same between the two fracture surfaces, then the two fracture surfaces will be identical. If they are different for some frequencies, then the surfaces will show mismatching over the corresponding length scales. Partial correlation can be achieved by combining the random phase component from one surface with a new random component for the second surface using a weighted mean. The weighting factor γ is normally defined as some function of frequency (Glover et al., 1998b; Matsuki et al., 2006). A mismatch cutoff frequency can be defined, which describes the length scales over which the mismatching develops, and has been shown to range from about 0.25 to 8.0 mm in real rock fractures (Glover et al., 1997, 1998b,a; Matsuki et al., 2006; Ogilvie et al., 2006; Ishibashi et al., 2015). Various models have been applied to describe the shape of the cutoff, and these are discussed by Kirkby et al. (2016). We follow Kirkby et al. (2016) by applying a mismatch cutoff frequency of 1 mm. Below the frequency cutoff, γ is a linear function of frequency (Section 5.3.2).

The absolute amplitude of surface height variations, measured in terms of the standard deviation σ_h, scales with the length L of a profile across the fracture (Matsuki et al., 2006):

$$\sigma_h = \sigma_{h,ref}\left(\frac{L}{L_{ref}}\right)^{3-D} = sL^{3-D} \tag{5.11}$$

where L_{ref} and $\sigma_{h,ref}$ are the length and standard deviation of the heights for a reference fracture surface. Kirkby et al. (2016) combined these to give s, a fracture length-independent scaling factor:

$$s = \frac{\sigma_{h,ref}}{L_{ref}^{3-D}} \tag{5.12}$$

Kirkby et al. (2016) demonstrated that there is broadly an inverse relationship between the two parameters. That is, in fracture surfaces with high fractal dimensions the standard deviation of the surface height overall tends to be smaller. Kirkby et al. (2016) used a fractal dimension of 2.4, which corresponds to a scaling factor of 1.9×10^{-3}.

5.3 Method

5.3.1 Fault network generation

A small volume of 1.5 cm × 1.5 cm × 1.5 cm was used. As discussed later, this volume size is a compromise between being able to model multiple realisations of a fault network in a reasonable time frame (given the number of cells required) and modelling a volume of rock that is large enough to be relevant to measurements of resistivity and permeability in the subsurface.

The fracture network comprises of three orthogonal sets of fractures. While this is not necessarily realistic for many natural fracture networks, it is a reasonable starting point in beginning to understand the cumulative effect fractures of different sizes have on a rock volume.

To generate synthetic fracture networks, an approach similar to that used by Xu and Dowd (2010) was used. The general approach is that the position of each fault in a network is defined randomly and assigned attributes including size, orientation, roughness, etc. If details of the fracture network are known (e.g. the dominant fault orientation or fault locations) then these can be assigned. However, for this work, the fault networks being described are completely synthetic, so key characteristics are selected from observations of natural fault networks.

First, Equation 5.8 was used to determine a fault size distribution. This was discretised using 20 bins per decade in log space, with Equation 5.8 providing the number of faults in each length bin. Then, for each fault, three uniform random seeds were generated to define the x, y and z position of the centre point of the fault within the rock volume. A uniform random fault length was selected from within the length bounds defined by the bin, and this length was also used as the height. An orientation was also randomly selected with equal probability for the yz, xz and xy plane. The fault was then assigned to the rock volume. Figure 5.1 shows the resulting distribution of faults for one of these fault networks.

5.3.2 Aperture assignment

Each fault in the network was assigned an aperture using the method described by Kirkby et al. (2016), which follows that of Matsuki et al. (2006) and Brown (1995). Two partly correlated fractal fracture surfaces were generated for each fracture, and these were then separated by a fixed distance for modelling.

The Fourier component a of each fracture surface is related to the fractal dimension D and the spatial frequencies p and q in the x and y direction, where l is the size of the fracture through

$$a_{1\ p,q} \propto \left(p^2 + q^2\right)^{((4-D)/2)} e^{i2\pi R_1} \tag{5.13}$$

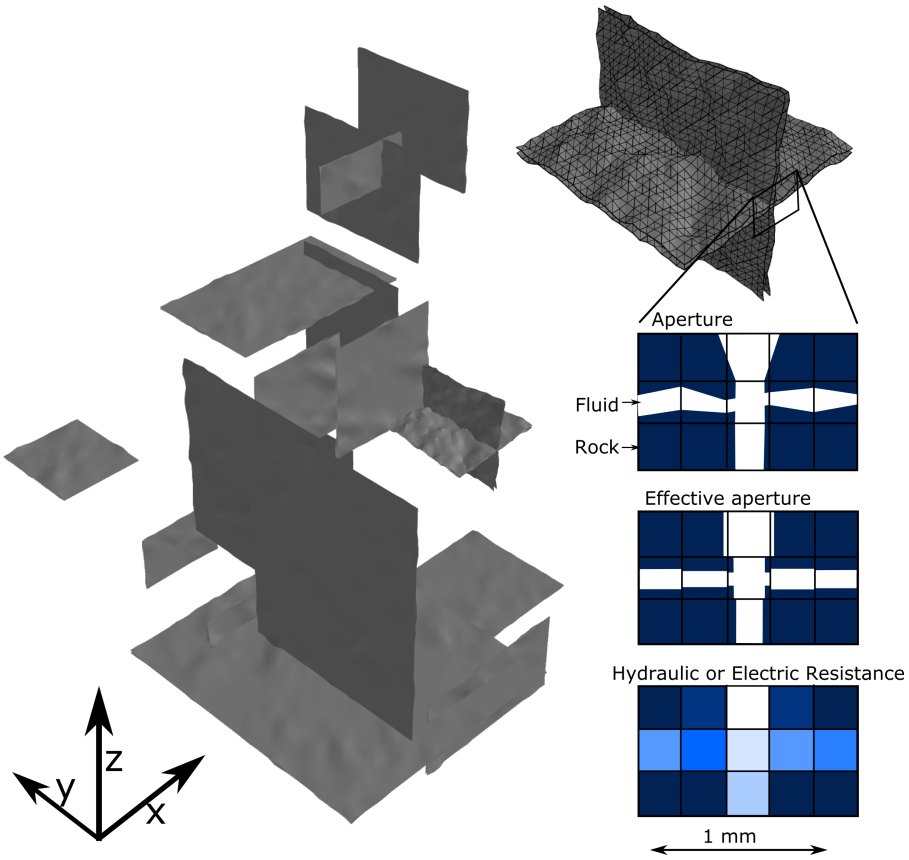

Figure 5.1: Key features of the model setup used for modeling fluid flow and current through fracture networks. An example fracture network is shown, generated with a equal to 2.5 and α equal to 3. Two intersecting fractures from the network shown in detail, from the fracture surfaces for each fracture, to the aperture, corrected aperture, and finally, the resistance. All aperture values in this diagram represent y direction resistances, i.e., into the page. The vertical fracture has a local aperture that exceeds one cell width, and so the fracture has been extended into the adjacent cells.

$$a_{2\ p,q} \propto \left(p^2 + q^2\right)^{((4-D)/2)} e^{i2\pi(R_1+\gamma R_2)} \tag{5.14}$$

Where R_1 and R_2 are independent uniform random numbers between 0 and 1 (Matsuki et al., 2006).

The surfaces differ by the random component R_2, scaled by γ which we define based on the mismatch cutoff frequency f_c (Section 5.2.4):

$$\gamma = \begin{cases} 1 & f > f_c \\ \frac{f}{f_c} & f \leq f_c \end{cases}$$

Once the two fracture surfaces had been created, they were scaled according to Equation 5.11 and separated by a fixed value for modelling. Overlapping parts of the fracture resulting in negative apertures were set to zero. Geometry-corrected apertures were then calculated using the method of Kirkby et al. (2016) (Sections 4.3.2 and 4.3.3).

5.3.3 Local resistance

The apertures were then used to calculate local electric and hydraulic resistances associated with the fracture plane, using Equations 5.2 and 5.5. To calculate the local resistance of the cell, a weighted harmonic mean of the resistance associated with the fracture, and that associated with the surrounding matrix in that cell, was used.

The fact that the modelling is now being carried out in 3D presents several additional challenges in assignment of aperture and calculation of local resistances. In 3D, it is not possible to dynamically change the cell size perpendicular to each fault according to the fracture aperture, as was done by Kirkby et al. (2016), as this would change the frequency spectrum of fault surfaces in the other directions. To counteract this, local fault apertures wider than one cell width were expanded across to fill adjacent cells. The expansion was done symmetrically, i.e. the expanded faults took up three, five, or seven cells and not two, four or six (Figure 5.1). In the case of electrical resistance, the fracture volume simply expands to adjacent cells, resulting in new apertures that can be used directly in Equation 5.2. The hydraulic resistance calculation is more complicated. This is because the resistance is related to the cube of the aperture, and so if the local aperture in each cell was reduced to fit in that cell, this would reduce the resistance of that cell by the cube of the aperture.

To manage hydraulic resistances for cells with the local aperture greater than the cell size, a concept of hydraulic resistivity is introduced. The local hydraulic resistivity, ρ_h, in any cell can be derived from Equations 5.2 and 5.5. For a connector in the z direction, associated with a fault opening in the x direction, ρ_h is given by:

$$\rho_h = \frac{R_H A}{\Delta z} = \frac{12\mu\Delta y}{b^2\Delta z} \tag{5.15}$$

Where Δy and Δz are the cell size in the y and z directions, respectively. If the cell size is the same in all directions, then ρ_h is simply $12\mu/b^2 = k\mu$, where k is the permeability. Thus, the hydraulic resistivity for matrix cells is simply $k_m\mu$, and in cells that contain both matrix and fracture, a weighted harmonic mean is used as for electrical resistivity. The hydraulic resistivity can then be used to calculate the resistance of the cell, in a similar way to electrical resistivity.

The second challenge is handling fault intersections. To assist with calculation, each connector (in each of the x, y and z directions) was initially assigned three aperture values representing faults opening in the x, y and z directions. The local resistance value was calculated for each cell, in each direction, by combining the resistances associated with each fault opening direction (Figure 5.1). In the case of electrical resistance, this was simply achieved by using the area of each of the faulted and matrix parts of the connector, and the resistivity of the fluid and matrix, in Equation 5.2. For example, for a connector in the z direction, with fluid resistivity ρ_f and rock matrix resistivity ρ_m:

$$R_{E,z} = \left(\frac{A_{fracture}}{\rho_f \Delta z} + \frac{\Delta x \Delta y - A_{fracture}}{\rho_m \Delta z} \right)^{-1} \tag{5.16}$$

Where the area taken up by the fracture, $A_{fracture}$, is given by

$$A_{fracture} = b_x \times \Delta y + b_y \times (\Delta x - b_x) \tag{5.17}$$

Where b_x and b_y are apertures opening in the x and y directions. In the case of hydraulic resistance, this was again more complicated. The hydraulic resistance in cells where two faults intersect was defined by summing the local hydraulic resistance associated with each of the two intersecting faults, and then subtracting the intersecting part. Equation 5.15 implies that the local hydraulic resistivity for each of the two intersecting faults will not necessarily be the same. The hydraulic resistivity associated with the smaller aperture (higher hydraulic resistivity) was therefore subtracted. For example, for a connector in the z direction:

$$R_{H,z} = \left(\frac{b_x \Delta y}{\rho_{h,zx}} + \frac{b_y \Delta x}{\rho_{h,zy}} - \frac{b_x b_y}{max(\rho_{h,zx}, \rho_{h,zy})} + \frac{\Delta x \Delta y - b_x \Delta y - b_y \Delta x}{k_m \mu} \right) \tag{5.18}$$

where $\rho_{h,zx}$ and $\rho_{h,zy}$ are hydraulic resistivity values in the z direction, associated with faults opening in the x and y directions, respectively.

5.3.4 Input parameters

A cell size of 0.25 mm was used for the networks, as was used by Kirkby et al. (2016). Using this cell size, it was possible to adequately represent the mismatching behavior of the faults, which occurs over wavelengths > 1 mm (Section 5.2.4), while at greater cell sizes this was not possible.

The largest resistor network that could be computed in a practical amount of time was around 60 × 60 × 60. This size can be calculated in around 20 minutes, while increasing the number of cells to 80 × 80 × 80 increases computation time to around 9 hours. Given that several thousands of models were to be run over the different input parameters as detailed below, a 60 × 60 × 60 network (or 1.5 cm × 1.5 cm × 1.5 cm) was considered to be a reasonable compromise.

The parameters controlling the distribution of faults in the network are maximum and minimum fault length, the exponent in Equation 5.8, a, and the constant α. A minimum fault length (truncation length) of 3 mm was used, based on the minimum fault length observed in natural fault networks in the review of Bonnet et al. (2001). The maximum fault length was taken as the size of the fault network.

Three values of α were used: 0.3, 3 and 30. These were selected to reflect the distribution of α in Bonnet et al. (2001). For this work, a was kept constant at 2.5. It

is acknowledged that varying a will likely also have an effect on the permeability and resistivity of the fracture networks. However, given the higher degree of variability in a, it is anticipated that variation in a will have a greater effect. Future studies could potentially analyse how the parameter a affects the resistivity and permeability of fractured rocks.

Likewise, the parameters of the fracture planes were kept constant. As with Kirkby et al. (2016), a fractal dimension of 2.4, and a scaling factor of 1.9×10^{-3} was used. These parameters, too, may affect the resistivity and permeability of the fracture networks, however, to keep the modelling as simple as possible, these were also kept constant.

The matrix permeability was set to 1×10^{-18} m^2. Kirkby et al. (2016) showed that varying this has little effect on the percolation behaviour that was observed, but simply raises the starting permeability below the percolation threshold. A rock to fluid resistivity ratio, defined here as m, of 10000, was used. Future work will consider other m values, however a value of 10000 represents a starting point in analysing the electrical and hydraulic properties of fractured rock networks.

Each permutation was modelled over twenty different fault separation values ranging from -0.16 mm to 0.89 mm. Fault separation was introduced by adding or subtracting a fixed value from the second surface generated in Section 5.3.2. The modelling was then repeated sixty times using different random number seeds to generate both the distribution of fractures within the network, and the fracture surfaces for each of the individual fractures. Given that each model was run six times, for the x, y, and z permeability and resistivity, this equates to a of 6000 model runs.

5.4 Results

5.4.1 Densely populated fracture networks

5.4.1.1 Resistivity and permeability

Figure 5.2 shows the results of fracture network modelling over twenty different fault separation values for sixty random fault networks. Both resistivity and permeability are shown as a function of fault separation for the highest value of α considered in this study, 30.

For α equal to 30 (Figure 5.2), all but one of the models demonstrate percolation behaviour in all three directions. That is, as the fault separation increases, the resistivity and permeability initially increase moderately, however at some point a fully connected pathway develops and the permeability and resistivity increase more rapidly. The permeability – aperture curves show a similar pattern to that of individual fractures (Kirkby et al., 2016), although the percolation threshold occurs at a slightly lower mean fault aperture on average (~0.01 mm rather than 0.02–0.03 mm), and begins to level out at a slightly lower permeability. The resistivity percolation threshold also oc-

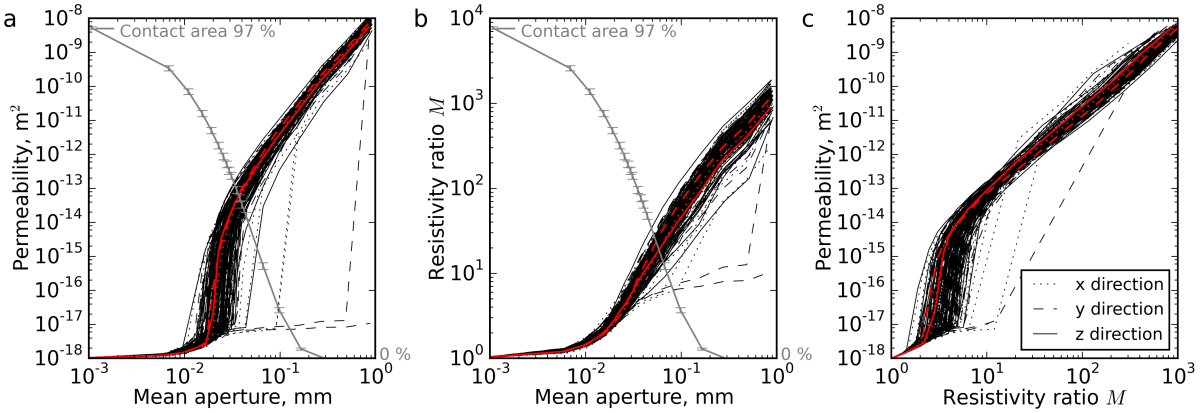

Figure 5.2: The evolution of permeability and resistivity (black dotted, dashed and solid lines for x, y and z directions respectively) in a dense fracture network with the density constant α equal to 30, as the fractures within that network are opened. (a) permeability and (b) resistivity ratio M in three directions as a function of arithmetic mean aperture. The mean and standard deviation contact area for all models shown in grey. (c) permeability as a function of M. The resistivity and permeability of the fracture network in Figure 5.4 shown in red.

curs at around 0.01 mm mean aperture. This curve is also similar to that for individual fractures, but levels off later.

Permeability is also shown as a function of the rock matrix to fracture network resistivity ratio, which we define here as M (Figure 5.2c). As with individual fractures, there is a percolation threshold in permeability with respect to M. The main difference between the curve for an individual fracture and that for a fracture network is the location of the percolation threshold. In fracture networks with α equal to 30, the percolation threshold occurs at an M value between 2 and 10. So (given an m value of 10^4), if M is greater than about 2 – 10, the rock is likely to be above its percolation threshold for fluid flow.

The percolation threshold does not necessarily occur at the same fault separation in each of the x, y and z directions. As a result, near the percolation threshold, the resistivity and permeability in the individual fracture networks become anisotropic (Figure 5.3). A similar effect was noted by Bahr (1997) in modelling the connectivity 2D resistor networks. However, this effect may simply reflect the limited size of the fracture networks considered in this study, and may disappear at larger sizes.

5.4.1.2 Fluid and current flow

An example of the fluid and current distribution in one of the fracture networks with an α value of 30 is shown in Figure 5.4. The modelled current and fluid flow are shown for four different values of fault separation. These diagrams demonstrate the physical processes that are occurring as the fractures within the network open and the network becomes more connected. The processes are quite similar to those described by Kirkby et al. (2016) for individual fracture planes.

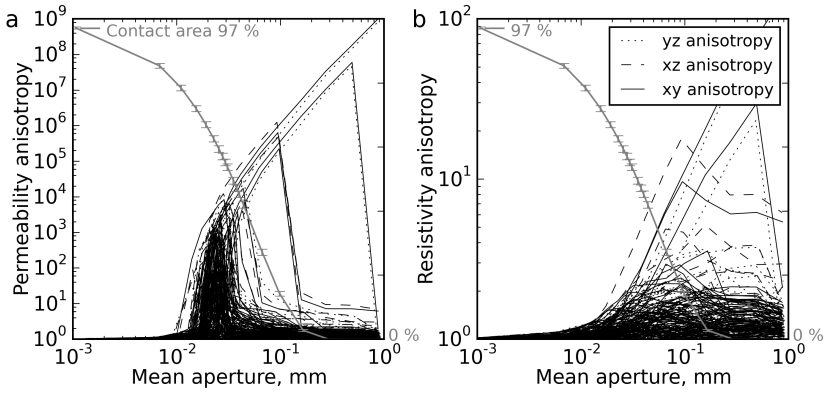

Figure 5.3: Anisotropy in permeability and resistivity as a function of arithmetic mean aperture for an α value of 30. Anisotropy shown as the maximum factor, i.e. xy anisotropy is the maximum of x/y and y/x resistivity or permeability. (a) permeability anisotropy and (b) resistivity anisotropy.

At a fault separation of -0.16 mm (i.e., the faults were shifted together by 0.16 mm, resulting in a mean aperture of 8×10^{-4} mm), there are no fully connected faults, and as such, most of the conduction and fluid flow occur through the rock matrix. At this point, the contact area on the faults is 97 %, i.e. on average, 97 % of each fault surface is in contact with the other surface, and the fracture porosity is 0.04 %. The permeability and M have both increased by a small, identical amount, at $1.02{\times}10^{-18}\text{m}^2$ and 1.02 respectively.

Once the fracture separation increases to -0.038 mm (mean aperture of 0.017 mm), connected pathways begin to form within the fracture network, although as yet, there are no fully connected pathways. Notably, Figure 5.4 shows both fluid flow and conduction in the matrix decreasing at this point, as fluids and current are no longer forced to pass through the rock matrix. These pathways travel along different intersecting fault planes, changing direction as they reach different fracture planes. The mean fault contact area is now 68 % and the fracture porosity 0.9 %. The permeability and M are $2.9{\times}10^{-18}$ m^2 and 2.2 respectively. Thus, despite the strong changes in fluid and current in this fracture network, the permeability and resistivity are still low, and this fracture network is below the percolation threshold.

The percolation threshold occurs at a fracture separation of -0.021 mm (mean aperture of 0.023 mm), where the first fully connected pathway for fluid flow forms through the network. For current, there is only one fully connected pathway, but several pathways that connect partially have now developed. There is also a small further decrease in both the current and fluid flow in the matrix. The percolation threshold is associated with a contact area of 60 %, and a fracture porosity of 1.1 %. The permeability increases markedly here ($1.3{\times}10^{-15}\text{m}^2$) while M shows another steady increase to 3.5.

By a fault separation of 0.009 mm (mean aperture of 0.036 mm), multiple connecting fluid pathways have formed through the network, and the fracture porosity has increased to 1.8 %. The contact area is now 46 %, while the permeability and M values are $5.0{\times}10^{-14}\text{m}^2$ and 8 respectively.

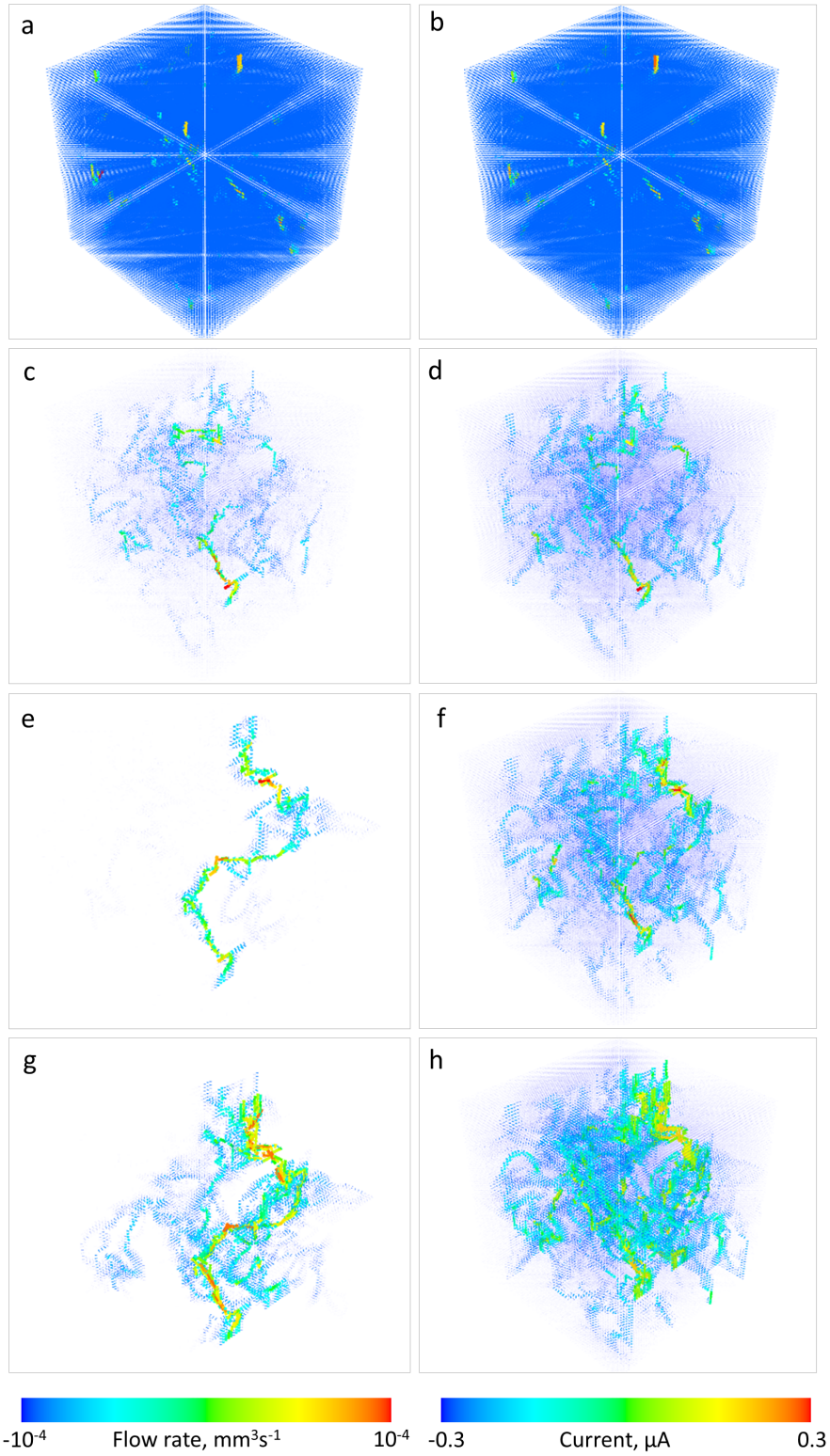

Figure 5.4: Fluid flow and current passing through a fracture network as the fractures are progressively opened. The network was built using an α value of 30. (a) flow rate and (b) current for a fault separation of -0.16 mm, (c) flow rate and (d) current for a fault separation of -0.038 mm, (e) flow rate and (f) current for a fault separation of -0.021 mm, (g) flow rate and (h) current for a fault separation of 0.009 mm. The resistivity and permeability of this network shown in Figure 5.2.

5.4.2 Sparse fracture networks

Figures 5.5 and 5.7 show resistivity and permeability as a function of aperture for α values of 3 and 0.3. The key difference in the results here is that for an α value of 3, only some of the networks demonstrate percolation behaviour, and for an α value of 0.3, only one of them does. This makes intuitive sense: the parameter α controls the density of faults, and as the density of faults is decreased, the likelihood of having a fully connected fracture network also decreases. For an α value of 3, none of the fault networks are fully connected (and thus able to demonstrate percolation behaviour with respect to the fault aperture) in all three directions, however 16 of them, or 27 %, have a percolation threshold in at least one direction. This implies that these rock volume models will have moderate to strong resistivity anisotropy (up to a factor of 160), and strong permeability anisotropy (up to a factor of 10^9), above the percolation threshold, since the rock is fully connected in some directions and not in others (Figure 5.6). However, there is no preferred orientation for which directions percolate and which do not, and so at larger scales this anisotropy may disappear.

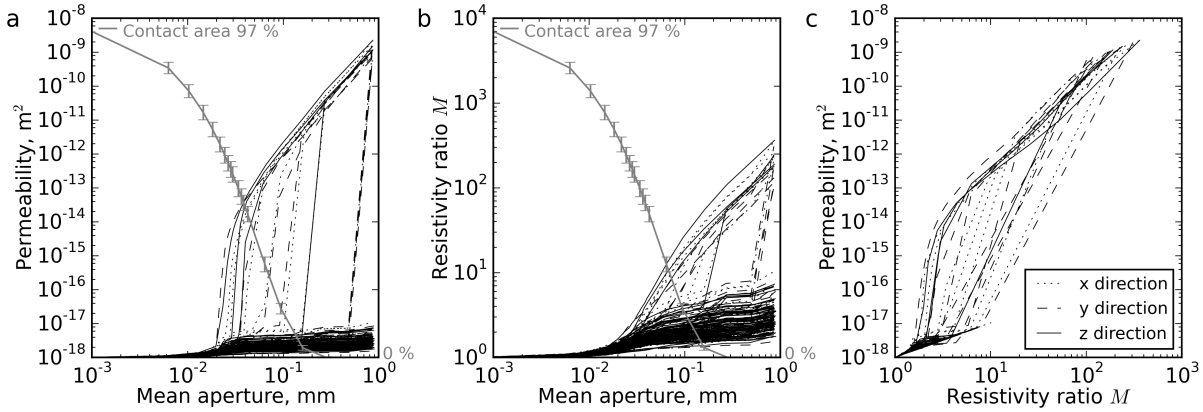

Figure 5.5: The evolution of resistivity and permeability (black dotted, dashed and solid lines for x, y and z directions respectively) in a dense fracture network with the density constant α equal to 3, as the fractures within that network are opened. (a) permeability and (b) resistivity ratio M in three directions as a function of arithmetic mean aperture. The mean and standard deviation contact area for all models shown in grey. (c) permeability as a function of M.

For α equal to 3, there is a greater spread in the percolation threshold for both permeability and resistivity, than for an α value of 30 (Figure 5.5). This results from the fact that many of the fault networks for α equal to 3 are themselves close to a percolation threshold, i.e., even if all the faults within the network are completely open, the networks themselves are on the verge between being connected and disconnected. Some of the fault network models may require that all the fractures within the network are fully connected, before the entire network will become connected. These will display a percolation threshold at a higher mean fault aperture. Others may become connected more easily and will thus percolate at lower mean apertures.

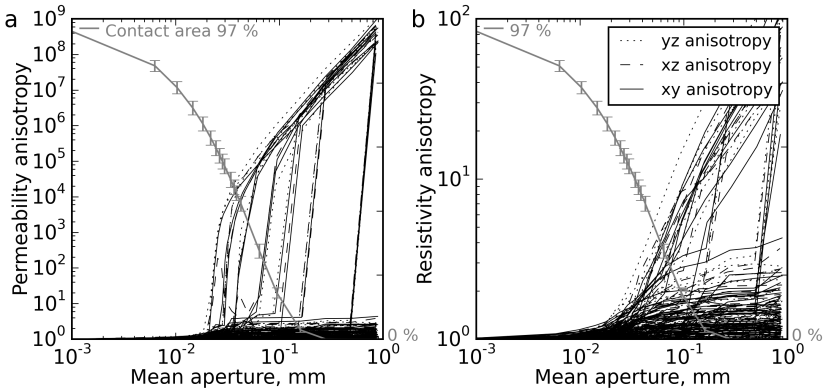

Figure 5.6: Anisotropy in permeability and resistivity as a function of arithmetic mean aperture for an α value of 3. Anisotropy shown as the absolute factor, i.e. xy anisotropy is the maximum of x/y and y/x. (a) permeability anisotropy and (b) resistivity anisotropy.

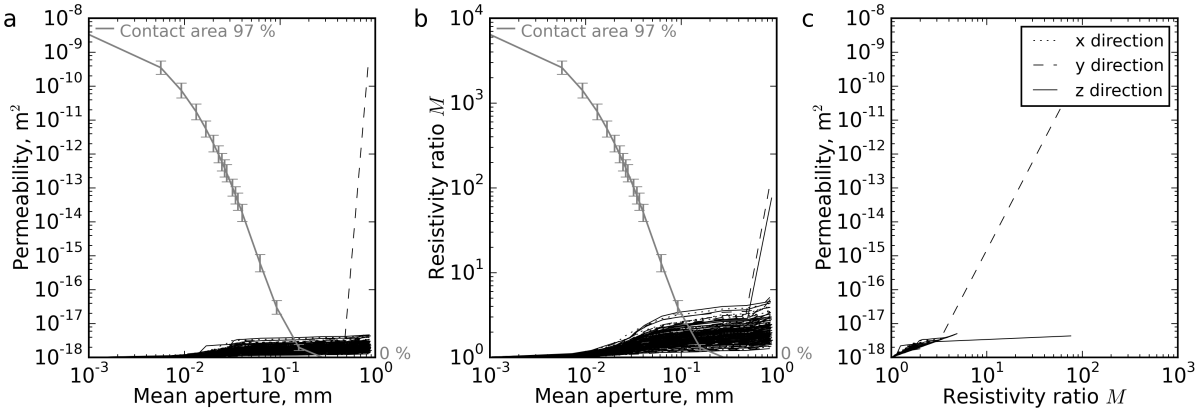

Figure 5.7: The evolution of resistivity and permeability (black dotted, dashed and solid lines for x, y and z directions respectively) in a dense fracture network with the density constant α equal to 0.3, as the fractures within that network are opened. (a) permeability and (b) resistivity ratio M in three directions as a function of arithmetic mean aperture. The mean and standard deviation contact area for all models shown in grey. (c) permeability as a function of M.

5.5 Discussion

Three dimensional electrical conduction and fluid flow models of fluid-filled fracture networks have been developed to assess the effect that fractures have on the resistivity and permeability of a rock. In these models, the ratio of rock matrix to fluid resistivity, m, has been held constant at 10^4. This is equivalent to the base case example considered by Kirkby et al. (2016) in modelling of individual fractures. Similar to individual fractures, fracture networks also display percolation behaviour.

The fracture network constant, α, which controls the density of fractures in the network, is a first order control on whether the network will be able to reach a percolation threshold. If α is low, then even when the individual fractures are fully connected, the

resistivity and permeability will never reach values more than one order of magnitude different from the rock matrix values. On the other hand, if α is high, then the network can reach low resistivity and high permeability values, if the fractures themselves are sufficiently open.

The control of α and other parameters (including the fracture network density exponent, a, Section 5.2.3) on the percolation threshold of fault networks has been studied extensively, at least with respect to fluid flow (e.g. Long and Witherspoon, 1985; Berkowitz, 1995; Mourzenko et al., 2005; Khamforoush et al., 2008). These studies consider the effect of a number of different fracture network characteristics on its percolation properties, in much more detail than considered here. In fact, the distribution of faults within a network has traditionally been assumed to be the key parameter driving the percolation behaviour. The faults within that network are often assumed to be fully connected, and are given constant flow properties (e.g. Mourzenko et al., 2011; Yazdi et al., 2011).

The modelling presented here builds on these studies by also considering variations in aperture in fractures within a network. The models show that when the fracture density constant, α, is sufficiently high, the separation between individual fault planes in the network is a strong control on the resistivity and permeability values. As with the percolation behaviour in individual fractures, the electrical and hydraulic properties of the fracture network depends strongly on the separation between the fault planes. Interestingly, even in an individual fault network, the percolation threshold occurs at different fault separation values for different orientations. Thus, near the percolation threshold, many of the models demonstrate anisotropy in both resistivity and permeability, even though the attributes of the fault network (probability of a fault in a given direction, size of fractures with different orientations) were assigned with equal probability for the xz, yz and xy planes. Anisotropy is more prevalent at smaller values of α. For an α value of 3, around 27 % of fault networks reach a percolation threshold, but only in one or two directions. This implies that above the percolation threshold, these will always have strong resistivity and permeability anisotropy. This effect may simply reflect the limited size of the fracture network, and will likely disappear on larger fracture networks, however it is interesting to note how easily anisotropic resistivity and permeability can develop in fractured rocks. If the fault separation was allowed to vary with orientation, for example, then anisotropic parameters may persist to larger volumes.

This work also builds on previous percolation studies by considering the permeability and resistivity of the rock matrix in the modelling. Traditionally (e.g. Long and Witherspoon, 1985; Berkowitz, 1995; Bahr, 1997; Mourzenko et al., 2005; Khamforoush et al., 2008), the rock matrix has been considered to be impermeable and infinitely resistive, so when the fracture network is not fully connected the permeability (and resistivity) is zero. However, Figure 5.4 demonstrates that even at low rock matrix permeabilities, and particularly below the percolation threshold, the rock matrix has an important role to play. Connecting pathways begin to form even below the percolation threshold, and these have an effect on both the permeability and resistivity of that network, even before it is fully connected.

The changes in the resistivity as the individual fractures within fracture networks are opened will also depend on the ratio of rock to fluid resistivity, m. This effect was not analysed here. Kirkby et al. (2016) showed that the decrease in resistivity at the percolation threshold becomes sharper with increasing m. This is because as m increases, the relative contribution of the matrix to the overall conduction decreases as the current becomes more focussed in the fractures. This effect is less in the fluid flow, partly because of the cubic dependence of flow rate on aperture, and partly because the difference in permeability between the rock and fractures tends to be higher than that for electrical resistivity. In any case, a similar effect is likely to be present in the fracture network as a whole, as in the fracture itself.

Fracture surface displacement was also not included in the models presented here. The displacement (offset) on a fault depends on the style of faulting and geological setting, but generally increases with fault size, and is normally between 0.1 and 10% of the fracture size for fractures less than 1 m in length (Kim and Sanderson, 2005). Thus, for the faults considered here, offsets of up to 1.5 mm might be expected. Offset increases the maximum width of the fault, which results in both the resistivity and permeability of faults increasing by a greater amount at the percolation threshold (Kirkby et al., 2016). A similar effect may occur if offset is added to fractures within a network.

A final limitation of the work presented here is the small size of the fracture network that could be computed. A 1.5 cm cube may be representative of small core samples, however to provide models that are more relevant to resistivities that are measured in well logs and by surface electrical geophysical methods, it would be necessary to scale up to larger rock volumes. In order to scale up, an approach similar to that used by Bahr (1997) could be applied. Bahr (1997) used embedded networks, in which each resistor in a larger network consists of a new, smaller network, which is analysed separately. This could be applied to the type of modelling presented here by generating a larger fracture network, and dividing that network into smaller cubes. The resistivity and permeability of these individual cubes could then be computed and used to fill a larger rock volume representing the entire fault network. This embedding process could be repeated multiple times to compute larger and larger volumes up to any scale of interest. However, it is noted that the properties of fracture surfaces used in this work are based on measured fractures up to 1 m^2 or so in area, so different fracture models might be needed to analyse these larger fractures.

5.6 Conclusions

Modelling of 3D fracture network models has shown that the percolation behaviour that was found in individual fractures is also present in fracture networks, as the fractures within that network are progressively opened. The ability of a network to percolate depends on characteristics of the fracture network itself, notably the density constant, α, as well as the properties of the individual fractures within the network, particularly the separation between the fault planes.

In the fracture networks presented here, where the rock to fluid resistivity ratio is equal to 10^4, resistivity enhancements up to a factor of 5000, and permeability enhancements up to ten orders of magnitude were observed. However, as with the individual fracture planes, permeability enhancement greater than one order of magnitude, and resistivity enhancement greater than a factor of $2 - 3$, is only possible if the fracture network is above its percolation threshold. This requires both the network itself, and the fractures within it, to be connected.

Resistivity anisotropy is common in fracture networks near their percolation threshold. In fracture networks with α equal to 3, more than half of them show anisotropy even when all the fractures within the network are completely open, because the fault network itself is near a percolation threshold. Likewise, many of the dense fracture networks, with α equal to 30, display anisotropy when the fractures within that network are close to their percolation threshold. This effect may disappear on larger fault networks, however it demonstrates how easily anisotropic properties can appear. Future work could look at how anisotropy in fault networks is controlled by variations in the fault separation with orientation.

CHAPTER

SIX

SUMMARY AND CONCLUSION

The overarching aim of the work presented in this thesis was to assess the use of the MT method for permeability exploration in resource industries such as unconventional geothermal, shale gas, and coal seam gas. Such industries rely on fracture permeability as resources are often hosted in rocks with low natural permeability. The MT method may be useful as it detects changes in resistivity, which, like permeability, depends not only on the volume of conducting phases in the crust but also their connectivity. The MT method is also sensitive to changes in resistivity with orientation. Fractures are planar features, and therefore if these are filled with a conductive material, MT may be able to sense their preferred orientation (e.g Wannamaker, 2005).

The MT method has successfully imaged fluid injection in a fracture network in a geothermal monitoring context (e.g. Peacock et al., 2012, 2013) and in monitoring of coal seam gas and shale gas prospects (Rees et al., 2016a,c). However, the information on associated permeability changes is only qualitative. The aim of this work has been twofold: first, to determine quantitatively how changes in resistivity from fractures filled with a conductive fluid relate to changes in permeability. A second aim has been to assess the use of MT in exploration of natural fractures. In order achieve these aims, two complementary approaches have been taken. Firstly, in Chapters 2 and 3, MT data from two regions of the Otway Basin in Victoria and South Australia were analysed for evidence for anisotropy. Secondly, in Chapters 4 and 5, the resistivity and permeability of synthetic fractures have been modelled to determine their electric and hydraulic properties.

6.1 Detecting fractured rocks with MT

In Chapter 2, an anisotropic interpretation was presented for an MT dataset from the Koroit region of the Otway Basin in Victoria, Australia. Strong phase and resistiv-

ity splits were interpreted in terms of anisotropy. Anisotropy was delineated within the Crayfish Group in the Otway Basin sequence and was interpreted to result from fluid-filled fractures and faults, which, rather than being resolved individually, reduce the bulk conductivity of the subsurface in the north-northwest direction. While no image logs are available from the Koroit region, electrically conductive fractures with a preferred north-northwest orientation have been observed in the Otway Basin in the Gordon 1 well, located to the northwest of the Koroit region (3D-Geo, 2009).

The anisotropy strike is consistent with known fracture orientations. Vandenberg (2000) noted that the dominant basement fabric is oriented north-northwest. Bailey et al. (2014) showed that in the Penola Trough, fractures with this orientation are favourably oriented for reactivation. North-northwest oriented neotectonic structures have been observed further north of the Koroit area, suggesting fractures with this orientation have been active recently. This observation lead Tassone (2014) to suggest that the basement fabric is controlling present-day fracture reactivation. Furthermore, permeability measurements in the Pretty Hill 1 well reveal high permeabilities within the Crayfish Group (Bain, 1962). Thus the anisotropic interpretation, resulting from fluid-filled fractures in faults, is consistent with other datasets.

In contrast, in Chapter 3 in the Penola Trough, minimal to no phase splits were observed. Minor phase splits occur in the northeast Penola Trough, and so inversions revealed only marginal anisotropy in this area. Moreover, the anisotropy strike determined from 1D inversion of these stations was not consistent with known fracture orientations. Thus, it appears that the data are compatible with an isotropic interpretation in Penola (Chapter 3).

While the MT (and other) data in Koroit are consistent with an electrically anisotropic subsurface, anisotropy may not be the only interpretation possible for the data. The ocean was considered as a possible cause of the observed phase and resistivity splits but was excluded on the basis of 2D forward modelling tests (Chapter 2). It is also possible that lateral changes in the subsurface resistivity, either within the Koroit area, or outside the survey area, are contributing to the phase splits in the data. Two or three dimensional structure within the Koroit area is less likely due to the highly consistent responses across the array and small tipper vector magnitudes. However, it is possible that external structure, located out of the immediate Koroit area, has some influence.

The results from these two regions highlight the problem of ambiguity in interpreting MT responses in isolation and the importance of bringing all available geological data into an interpretation. As noted by previous authors (e.g. Heise et al., 2006; Martí, 2014) and again in Chapter 3, the MT response at a single site, or even at several closely spaced sites, can be identical for a 2D and a 1D anisotropic subsurface.

6.2 The resistivity and permeability of fractures

in Chapters 4 and 5, the resistivity and permeability of fractured rocks was examined. A resistor network approach was used, similar to that presented by Bahr (1997) in

modelling the electrical properties in rocks, but with a few key differences. The first of these is that realistic fractures were included in the models, with variable aperture, using the model based on measured fracture surface profiles by Brown (1987, 1995) and developed by Matsuki et al. (2006). The fracture aperture distribution generated from this model, combined with the electrical resistivity of the fluid, were used to calculate local electrical resistances in the fracture plane. In Chapter 4, a simulated potential difference was applied along the fracture, resulting in an electrical current distribution, which was then used to calculate the bulk resistivity of the fracture. The same process was applied for fluid flow, with the local fracture aperture in the plane used to calculate local hydraulic resistances, and with a simulated pressure difference applied. In Chapter 5, the same method was applied to 3D fracture networks, with each fracture containing a realistic aperture distribution as for Chapter 4.

Similar to the work of Bahr (1997), the models were been evaluated as the system becomes incrementally more connected. However, in Chapters 4 and 5, this objective was achieved in a different way. While Bahr (1997) gradually increased the probability of connection in a given direction, in Chapters 4 and 5 the fracture was incrementally opened from the starting condition where the fracture is completely closed. In this way, the resistivity and permeability relationship was explored based on measurable fracture characteristics.

Modelling shows that the resistivity and permeability are highly sensitive to the separation between fault planes in both individual fractures and fracture networks. Similar to the results of Bahr (1997), which showed conductivity is non-linearly dependent on probability of connection, Chapters 4 and 5 show that both the conductivity and permeability of fractures varies non-linearly with mean fracture aperture. At low apertures, void space exists only in isolated pockets and thus the overall permeability and resistivity is only slightly greater than that of the rock matrix. As the fracture or fractures within the network open, more of the fracture or network becomes connected until it reaches its percolation threshold. At this point, fully connected paths form, and the permeability increases by multiple orders of magnitude. The increase in the electrical conductivity is generally less, occurs over a wider aperture range, and depends on the resistivity of the fluid and the rock matrix. Based on the results in Chapter 4, strong resistivity enhancement due to fractures (greater than a factor of about 3) requires a large contrast in resistivity between the matrix and the fluid (matrix to fluid resistivity ratio of around 1000 or more) and the faults to be over their percolation threshold. Further, the work shows that the transition from below to above the percolation threshold occurs over very small aperture changes of <0.1 mm. Therefore, slight changes in the openness of a particular fracture due to, for example, changes in the stress field either spatially or temporally, can lead to large differences in electrical and hydraulic properties.

Chapter 5 demonstrated that the changes in rock resistivity and permeability depend on characteristics of the fault network as well as the individual faults within that network. In particular, the constant α controls the density of faults within a network. Almost all fault networks with α equal to 30 (densely populated) can reach a percolation threshold with respect to the mean fault aperture. On the other hand, only one of the analysed

networks with α equal to 0.3 reached a percolation threshold with respect to aperture. Only around 27 % of intermediate fracture networks with α equal to three reach a percolation threshold, and most of these will only reach a percolation threshold in one direction. Strong anisotropy is observed in these networks when they are above their percolation threshold. Anisotropy is also observed in dense fault networks near their percolation threshold.

6.3 Challenges and future directions

Markedly different MT responses were observed in two areas of the Otway Basin (Chapters 2 and 3), despite similar lithologies being present in the two areas. Both areas are located in local troughs in the Otway Basin, with the depth to basement ranging from about 3 to 6 km in each area (Figures 2.12c and 3.8) and thus variations in basement depth are similar between the two regions. However, it is still possible that the phase splits at Koroit result, fully or in part, from lateral resistivity variations. Ambiguity between isotropic and anisotropic models is a problem in the interpretation of MT data that has been noted before (e.g. Heise et al., 2006; Martí, 2014), and presents a challenge in using the MT method for exploration for fracture permeability. There are several ways that this ambiguity may be reduced.

Two or three dimensional forward modelling tests might be informative in order to determine the resistivity effect of known structures in the Koroit region. Depth to basement models are available for both areas (Jensen-Schmidt et al., 2002; Jorand et al., 2010), and so simple forward modelling tests may be useful in testing the effect of changes in basement topography. Alternatively, 3D isotropic, or 2D anisotropic inversions may help to provide more certainty in the Koroit region as to the amount and distribution of anisotropy. In doing this, MT data outside of the immediate Koroit area would be useful to examine the influence of outside structure.

One way to directly test for the presence of anisotropic resistivity characteristics in the Koroit region may be through further drilling and/or well logging. Electromagnetic resistivity logging tools that provide directional information on resistivity, several metres into the formation, have been recently introduced as a tool in characterising petroleum reservoirs and guiding drilling (e.g. Li et al., 2005; Bittar et al., 2009). These could provide direct evidence on the location and amount of any anisotropy present.

Whether or not electrical resistivity anisotropy is present and expressed in the MT data at Koroit, and absent at Penola, the work raises an important point. It is common practice to interpret MT data isotropically, unless there is evidence for anisotropy, or an isotropic data cannot match the data. Anisotropy is often not observed to be a possibility in interpretation. However, geological features are commonly anisotropic, with sedimentary layering and fracturing both forming on planes. Thus, as discussed in Section 1.2.3, the resistivity of these rocks will be anisotropic.

Synthetic modelling of fractures and fracture networks has started to provide a physical basis for how fractures reduce the resistivity of a rock, which could then lead to

macro-scale resistivity anisotropy if open fractures form along a preferred orientation. Fractures have been shown to change the resistivity of the subsurface following the injection of an electrically conductive fluid, in an unconventional geothermal context (Peacock et al., 2012, 2013) and in shale gas and coal seam gas monitoring (Rees et al., 2016a,c). Chapters 4 and 5 demonstrated that the transition from below to above the percolation threshold occurs over a change of mean fault aperture of <0.1 mm. Therefore, small changes in the fault aperture can lead to large changes in resistivity and permeability.

One of the limitations of the modelling in Chapters 4 and 5 is that it assumes no deformation, either on the fracture planes, or in the surrounding rock. Deformation on and around the fracture plane may change the overall resistivity and permeability. Therefore, the results presented in Chapters 4 and 5 are most relevant to minor fractures with small offsets, that are less likely to have significant damage associated with them. The modelling could quite easily be extended to fractures with deformation, but a realistic fracture model that includes deformation would be required.

A second limitation is that the approach relies on all faults being filled with a conductive fluid, and not other conductive materials such as siderite, clay, or graphite. In a relatively un-compacted sedimentary basin like the Otway Basin, it is unlikely that significant graphite will be present in fractures due to the high temperatures and pressures needed for graphite to form. However, it could be present in crystalline rocks that might be encountered in an unconventional geothermal reservoir. It is also quite possible that clay is present in both sedimentary and crystalline rocks, and this could reduce the resistivity but either have no effect on, or even reduce, the permeability. The electrically conductive mineral siderite was noted to be present on fracture surfaces in the Penola Trough (Bailey et al., 2014). Despite this, it is common practice to assume that electrically conductive fractures on borehole image logs are open for fluid flow (e.g. Bailey et al., 2014). So this problem is not unique to MT, but applies to both resistivity logs, and resistivity-based image logs as well.

One way to help reduce this ambiguity is to use core from one or two drillholes to characterise the proportion of fluid-filled and clay-filled fractures. While this would not eliminate the uncertainty, it would provide more certainty in a given area as to the general character of the fractures and their fill material. If core samples were able to provide information on the proportion of clay-filled to fluid-filled fractures in an area, for example, this would be informative in using any measured resistivity (or resistivity anisotropy) values to deduce permeability.

6.4 Concluding remarks

To conclude, MT shows considerable promise in inferring the presence and orientation of conductive natural fractures. Synthetic modelling on fracture network models with a rock to fluid resistivity ratio of 10^4 shows that resistivity reduction from fluid-filled fractures by a factor of ten or more is usually associated with fracture networks that are

over their percolation threshold, and are therefore highly permeable. At the percolation threshold, both resistivity and permeability are highly sensitive to changes in aperture.

If fractures filled with a conductive material show a preferred orientation, or if the stress field is such that one orientation is only slightly more open than others, macro-scale resistivity anisotropy may well be present. However, in order use MT to effectively image these, the ambiguity surrounding isotropic vs. anisotropic models must be reduced. This could be achieved by using a wide array of MT data (covering more than the area of interest), and utilising data from wells (in particular, directional resistivity measurements), and other data sources.

Appendices

APPENDIX

A

SUPPORTING INFORMATION FOR CHAPTER 2

A.1 Station locations

The station locations for the Koroit MT survey are shown in Figure A.1 and tabulated in Table A.1.

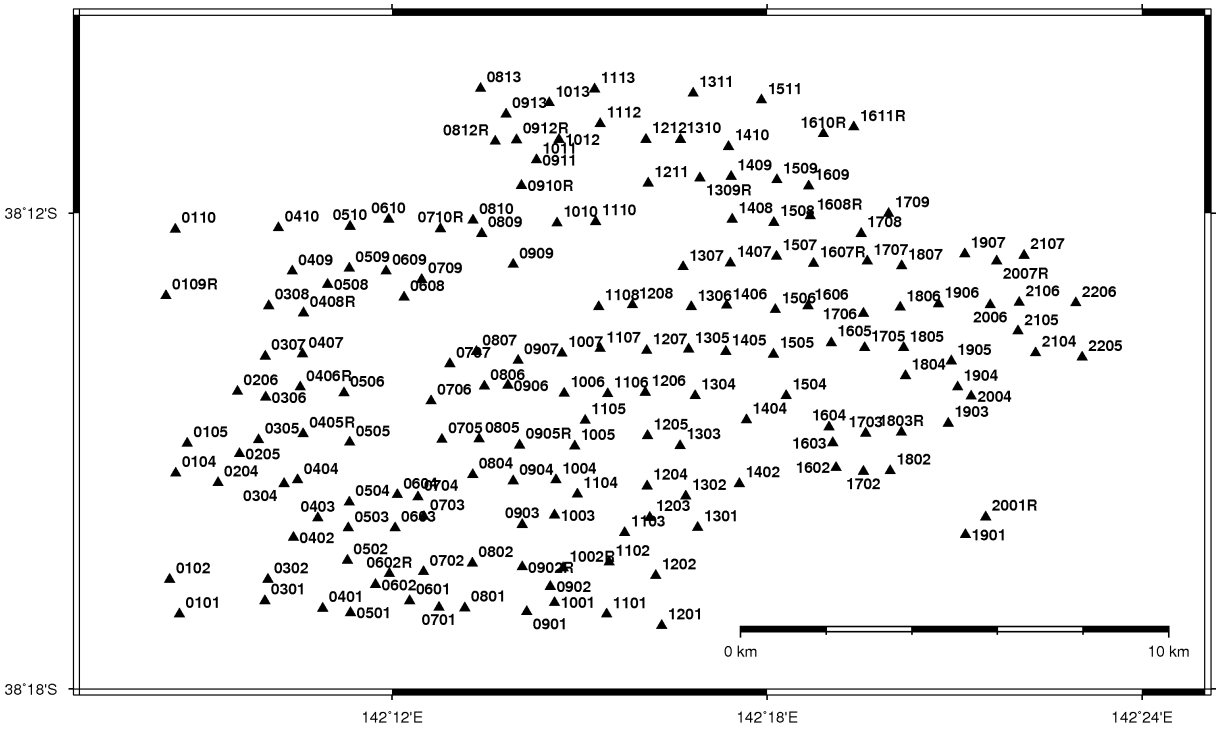

Figure A.1: Locations of MT stations in the Koroit MT survey (Chapter 2). Station labels displayed as numbers only for clarity.

Table A.1: Station locations in the Koroit MT survey.

Station	Longitude	Latitude
K0101	142.143317	-38.284317
K0102	142.140733	-38.277017
K0104	142.1423	-38.254683
K0105	142.145417	-38.2484
K0109R	142.139683	-38.217367
K0110	142.142244	-38.203367
K0204	142.15355	-38.256717
K0205	142.159303	-38.250586
K0206	142.158764	-38.237497
K0301	142.16605	-38.281467
K0302	142.166867	-38.277033
K0304	142.171183	-38.256883
K0305	142.164433	-38.24765
K0306	142.166303	-38.238736
K0307	142.166153	-38.230069
K0308	142.167081	-38.219481
K0401	142.181497	-38.283086
K0402	142.1737	-38.268217
K0403	142.180231	-38.264119
K0404	142.17485	-38.25615
K0405R	142.176264	-38.246417
K0406R	142.175456	-38.236636
K0407	142.176119	-38.2296
K0408R	142.176414	-38.221
K0409	142.173383	-38.212233
K0410	142.16975	-38.203083
K0501	142.1889	-38.284
K0502	142.18805	-38.273033
K0503	142.188333	-38.266247
K0504	142.1886	-38.260783
K0505	142.188667	-38.248217
K0506	142.187186	-38.237781
K0508	142.182833	-38.21495
K0509	142.188583	-38.211633
K0510	142.188764	-38.202753
K0601	142.204733	-38.281467
K0602R	142.199317	-38.27585
K0602	142.195617	-38.27815
K0603	142.200806	-38.266219
K0604	142.201364	-38.259239
K0608	142.203183	-38.217683
K0609	142.198383	-38.212217
K0610	142.199122	-38.201303
K0701	142.21255	-38.282867
K0702	142.208364	-38.27545
K0703	142.208533	-38.2638
K0704	142.206869	-38.259667
K0705	142.213331	-38.247578
K0706	142.210397	-38.239497
K0707	142.215422	-38.231733
K0709	142.20795	-38.213967
K0710R	142.21295	-38.203253
K0801	142.219433	-38.283
K0802	142.221436	-38.273631
K0804	142.221478	-38.255003
K0805	142.223169	-38.247503
K0806	142.224606	-38.236369
K0807	142.222461	-38.229136
K0809	142.223886	-38.204283
K0810	142.221589	-38.201494
K0812R	142.227478	-38.18495
K0813	142.223581	-38.173781
K0901	142.235886	-38.283814
K0902R	142.234664	-38.274419
K0902	142.2422	-38.278503
K0903	142.234731	-38.265478
K0904	142.232278	-38.256331
K0905R	142.234036	-38.248786
K0906	142.230864	-38.236231
K0907	142.233567	-38.230983
K0909	142.232253	-38.210828
K0910R	142.234533	-38.194167
K0911	142.23845	-38.1888
K0912R	142.233217	-38.184567
K0913	142.230417	-38.179167
K1001	142.243319	-38.281853
K1002R	142.245617	-38.274617
K1003	142.243311	-38.263542
K1004	142.243719	-38.256058
K1005	142.24865	-38.249033
K1006	142.245903	-38.237931
K1007	142.245336	-38.229511
K1010	142.244017	-38.202061
K1011	142.23845	-38.1888
K1012	142.2445	-38.184517
K1013	142.241883	-38.176833
K1101	142.257167	-38.28435
K1102	142.257894	-38.273408
K1103	142.26205	-38.267233
K1104	142.249383	-38.259083
K1105	142.2515	-38.243617
K1106	142.257528	-38.238003
K1107	142.255469	-38.228536
K1108	142.255089	-38.219653
K1110	142.254314	-38.201756
K1112	142.255531	-38.181222
K1113	142.253994	-38.173919
K1201	142.271917	-38.286717
K1202	142.27025	-38.276167
K1203	142.268653	-38.263964

Table A.2: Station locations in the Koroit MT survey (continued).

Station	Longitude	Latitude
K1204	142.268	-38.257364
K1205	142.268117	-38.246833
K1206	142.267533	-38.237689
K1207	142.267872	-38.228917
K1208	142.264117	-38.21925
K1211	142.268267	-38.19375
K1212	142.267694	-38.184497
K1301	142.281514	-38.266114
K1302	142.278314	-38.259497
K1303	142.276811	-38.248869
K1304	142.2808	-38.238417
K1305	142.279119	-38.228614
K1306	142.2798	-38.219747
K1307	142.277572	-38.211317
K1309R	142.282086	-38.192569
K1310	142.276886	-38.184497
K1311	142.28025	-38.1748
K1402	142.2926	-38.25685
K1404	142.294467	-38.243483
K1405	142.288967	-38.229119
K1406	142.289167	-38.219433
K1407	142.290247	-38.210486
K1408	142.290736	-38.201333
K1409	142.29045	-38.192333
K1410	142.289736	-38.185969
K1504	142.305083	-38.2384
K1505	142.301681	-38.229664
K1506	142.302217	-38.220317
K1507	142.302467	-38.209097
K1508	142.301847	-38.20195
K1509	142.302617	-38.192967
K1511	142.298508	-38.176242
K1602	142.31845	-38.253467
K1603	142.317531	-38.248322
K1604	142.3165	-38.244953
K1605	142.317083	-38.22725
K1606	142.310917	-38.219517
K1607R	142.312397	-38.210564
K1608R	142.311531	-38.200569
K1609	142.311067	-38.194317
K1610R	142.314967	-38.183336
K1611R	142.323117	-38.181933
K1702	142.325686	-38.254331
K1703	142.326317	-38.246331
K1705	142.326033	-38.228283
K1706	142.325683	-38.221133
K1707	142.326722	-38.210069
K1708	142.325053	-38.204267
K1709	142.332444	-38.200119
K1802	142.332836	-38.254167
K1803R	142.335764	-38.246097
K1804	142.33685	-38.234233
K1805	142.33635	-38.22835
K1806	142.3355	-38.219833
K1807	142.335936	-38.211119
K1901	142.352867	-38.267633
K1903	142.34825	-38.244183
K1904	142.350753	-38.236553
K1905	142.34905	-38.231103
K1906	142.345689	-38.2191
K1907	142.352667	-38.2086
K2001R	142.358286	-38.263853
K2004	142.354444	-38.238536
K2006	142.35955	-38.219267
K2007R	142.361239	-38.210117
K2104	142.371617	-38.229397
K2105	142.366917	-38.224847
K2106	142.3672	-38.2188
K2107	142.368517	-38.208867
K2205	142.38395	-38.230281
K2206	142.382297	-38.218917

A.2 Koroit MT data and responses

This section contains the resistivity and phase data and model responses from the 1D anisotropic inversions presented in Chapter 2.

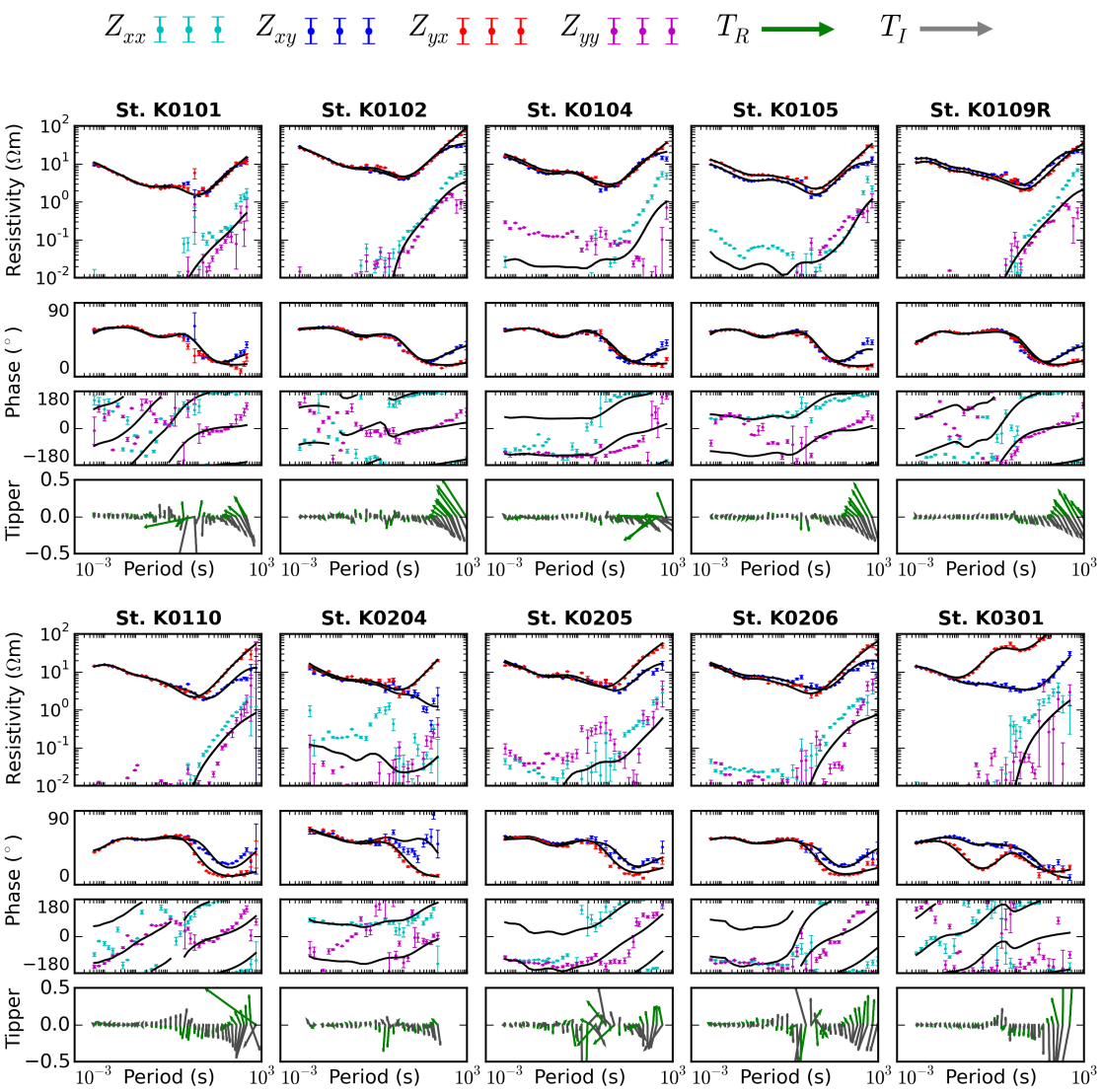

Figure A.2: Koroit data and resistivity and phase responses to the 1D anisotropic inversion models in Chapter 2. Resistivity and phase responses shown in black over the input data; real and imaginary tipper data shown in green and grey.

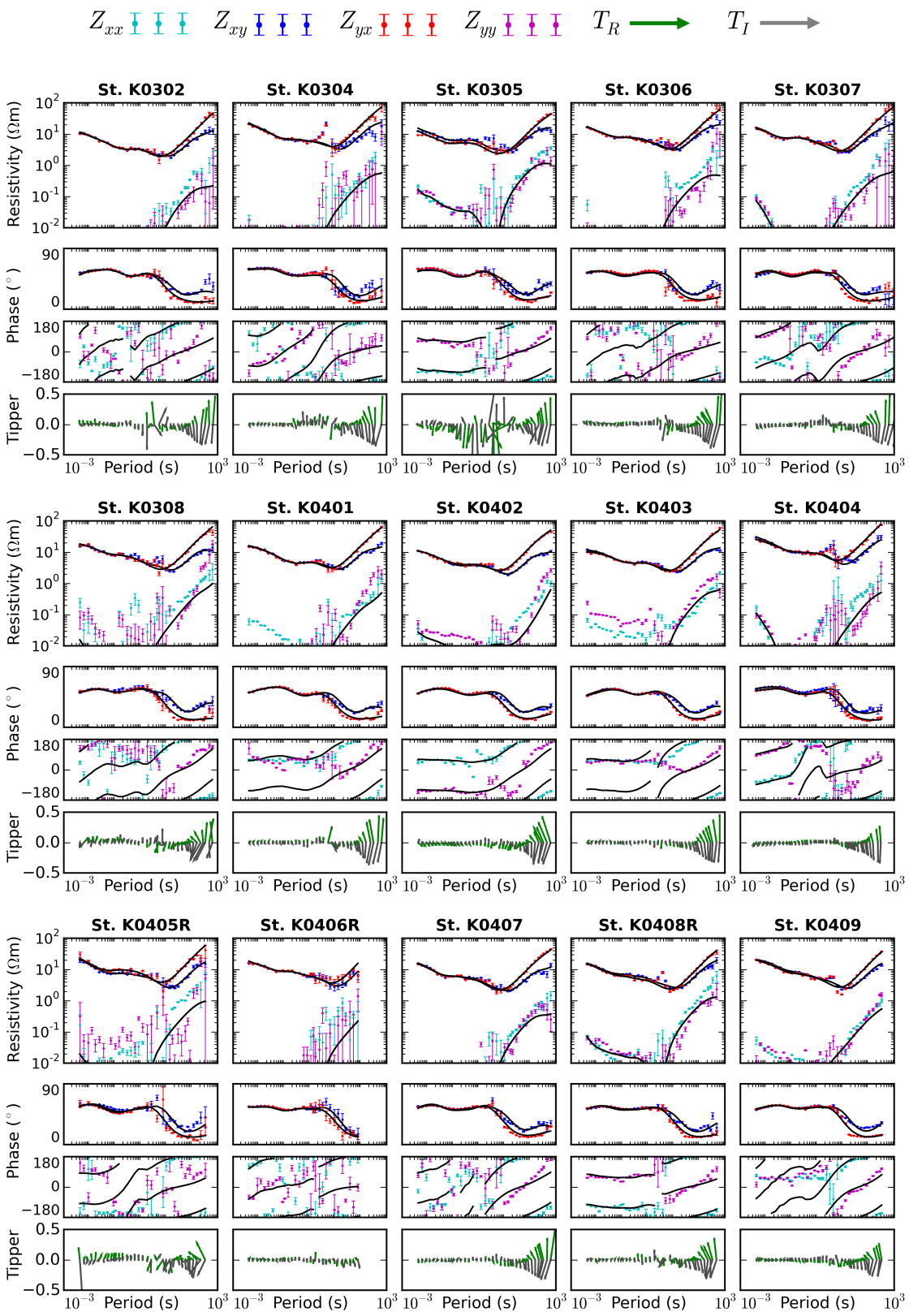

Figure A.3: Koroit resistivity and phase data and responses to the 3D inversion model in Chapter 2 (continued).

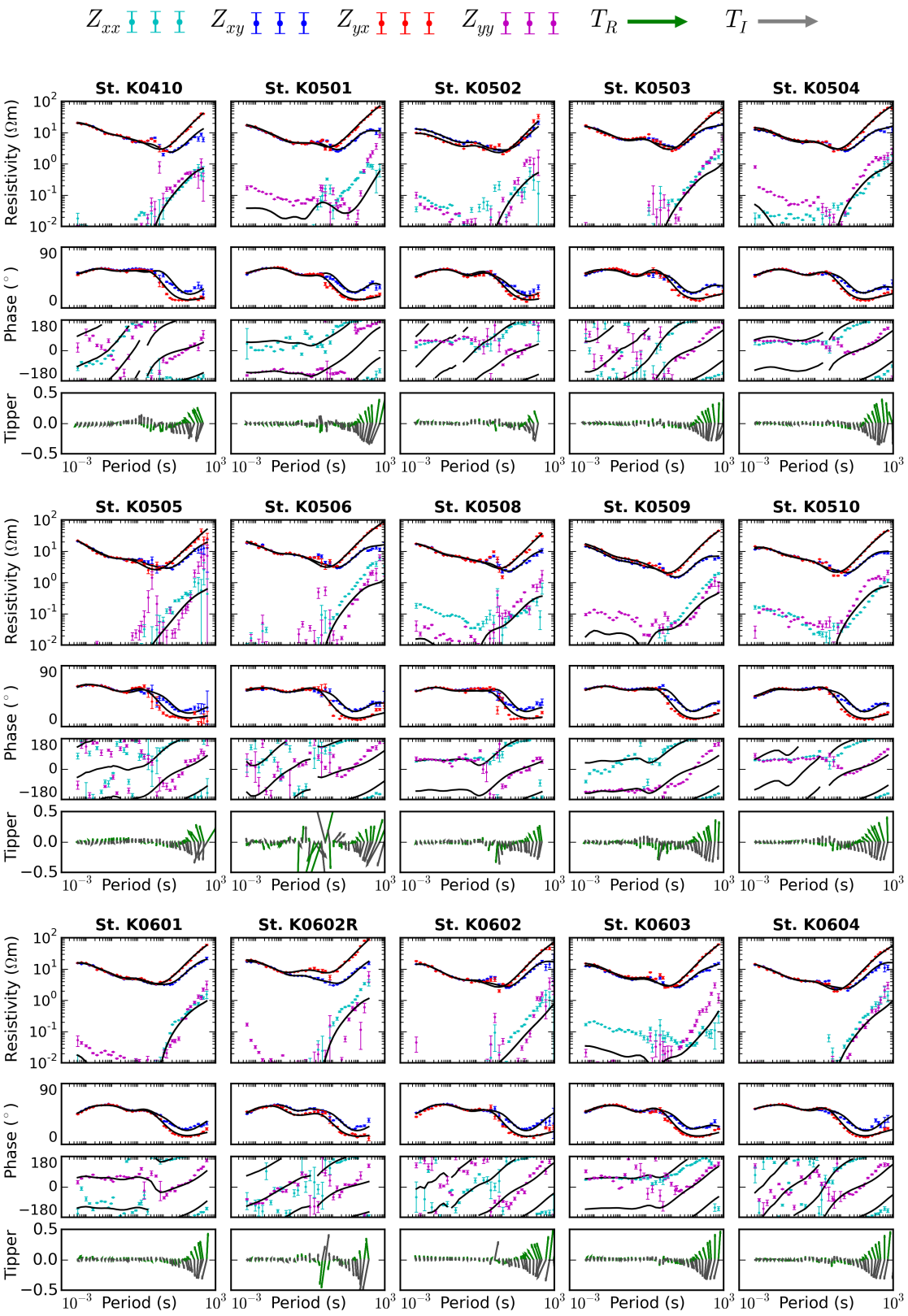

Figure A.4: Koroit resistivity and phase data and responses to the 3D inversion model in Chapter 2 (continued).

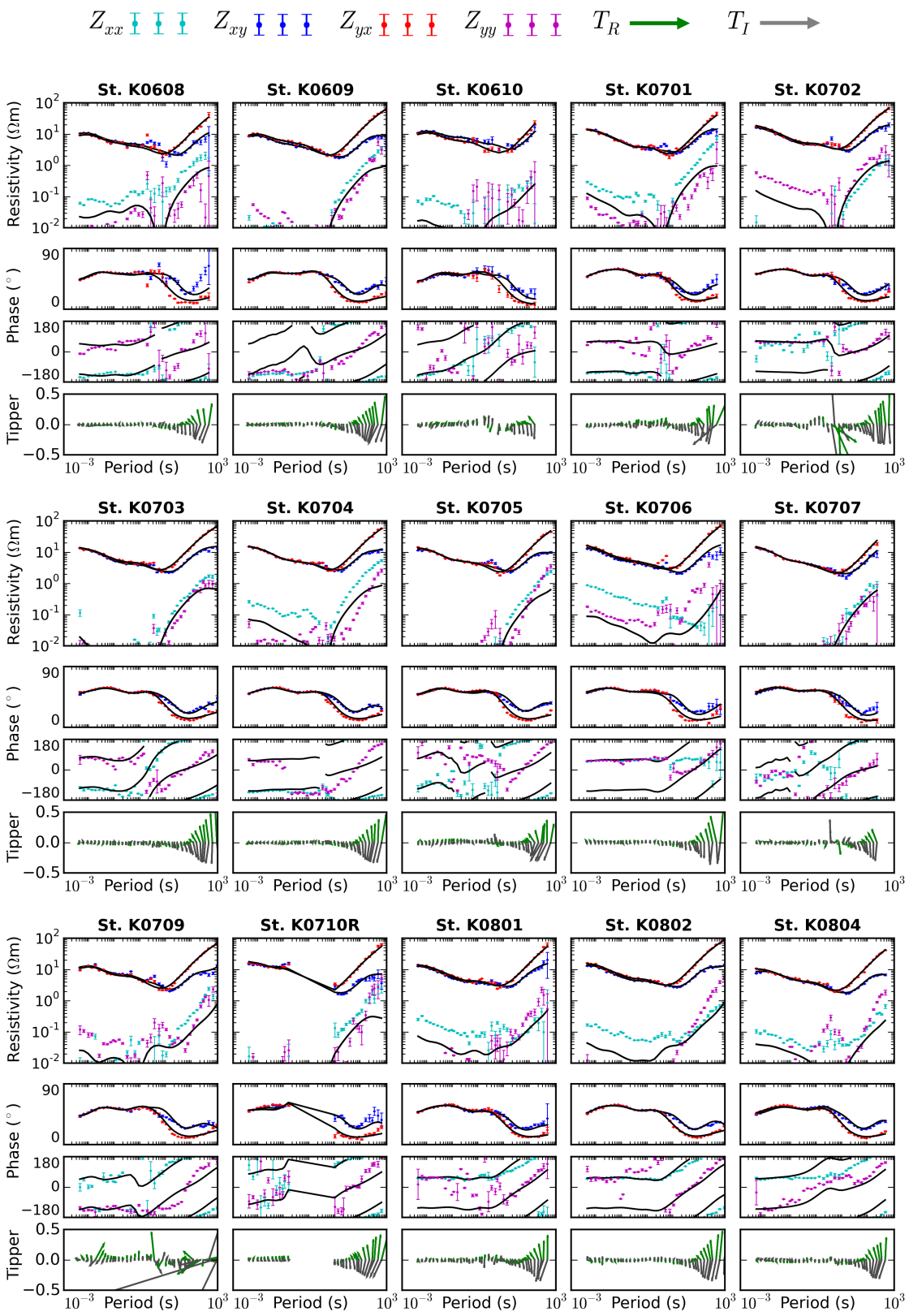

Figure A.5: Koroit resistivity and phase data and responses to the 3D inversion model in Chapter 2 (continued).

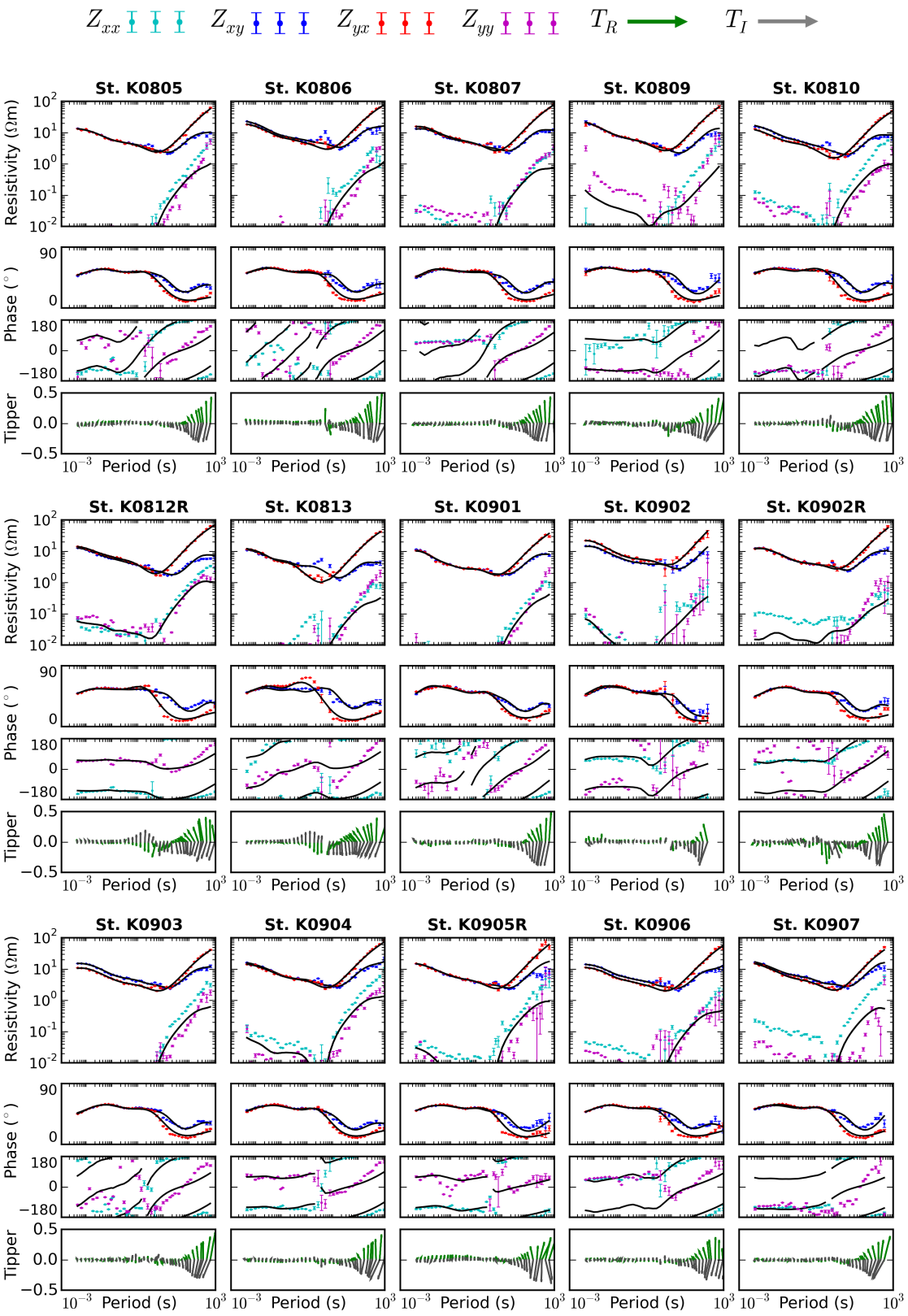

Figure A.6: Koroit resistivity and phase data and responses to the 3D inversion model in Chapter 2 (continued).

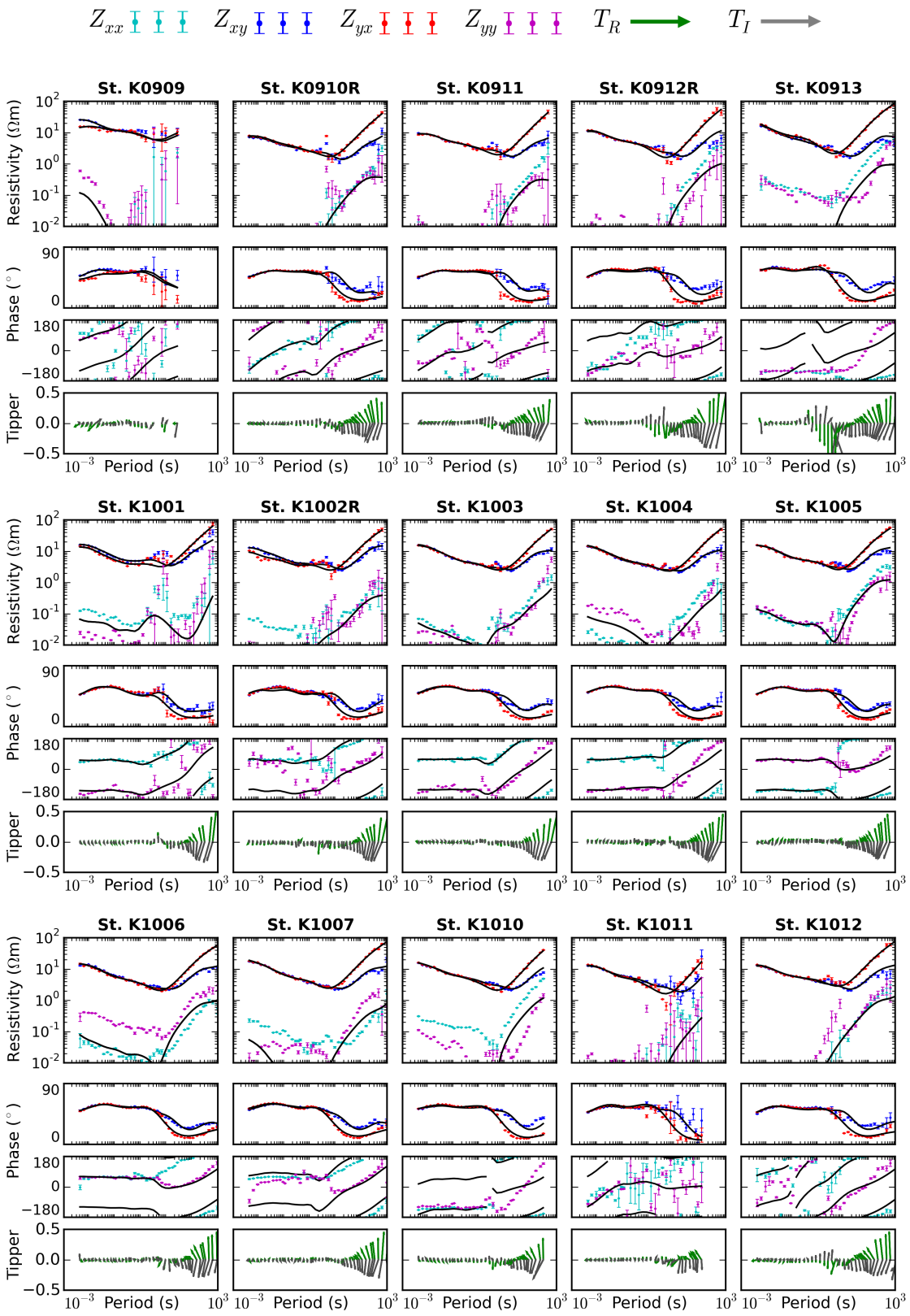

Figure A.7: Koroit resistivity and phase data and responses to the 3D inversion model in Chapter 2 (continued).

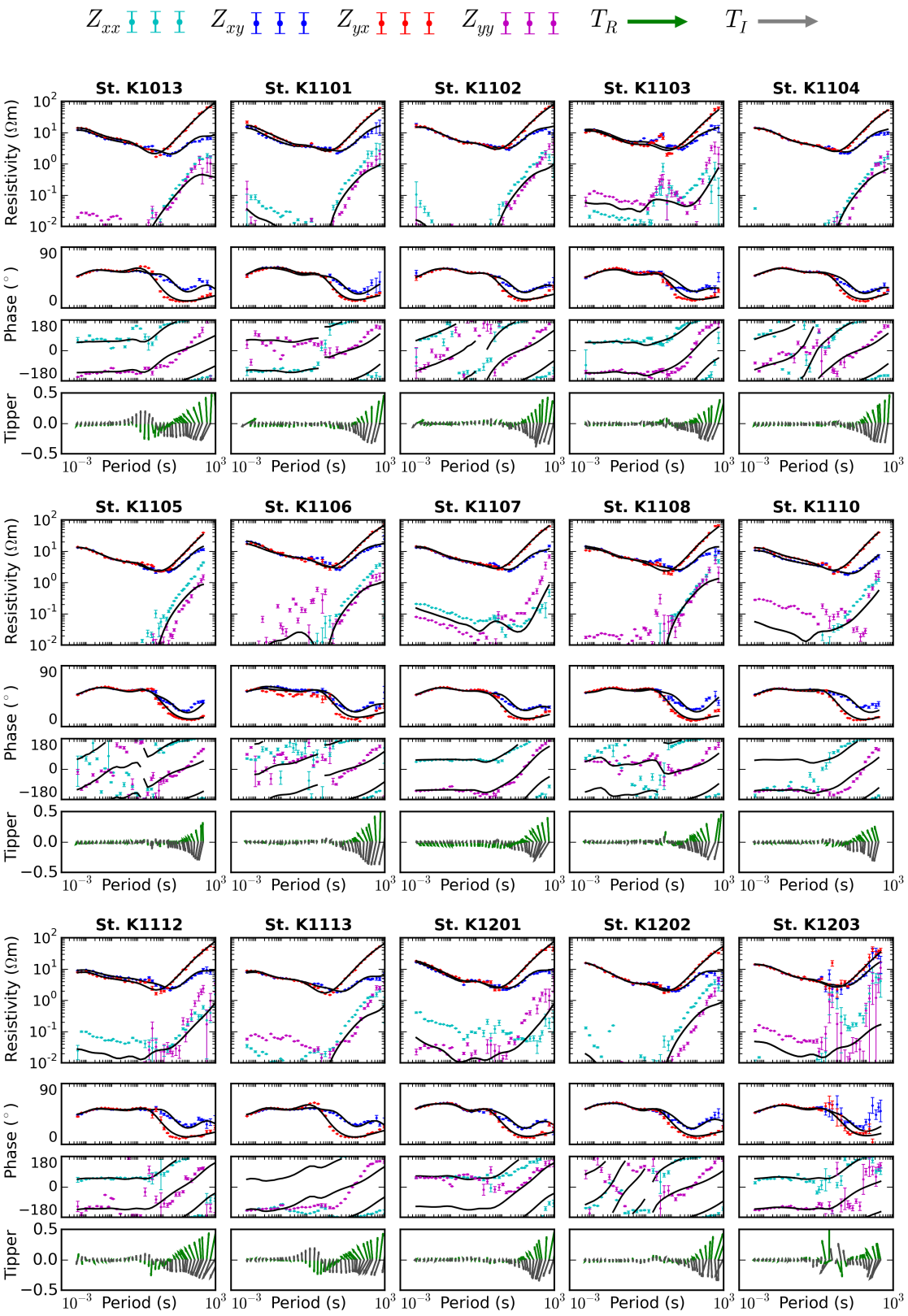

Figure A.8: Koroit resistivity and phase data and responses to the 3D inversion model in Chapter 2 (continued).

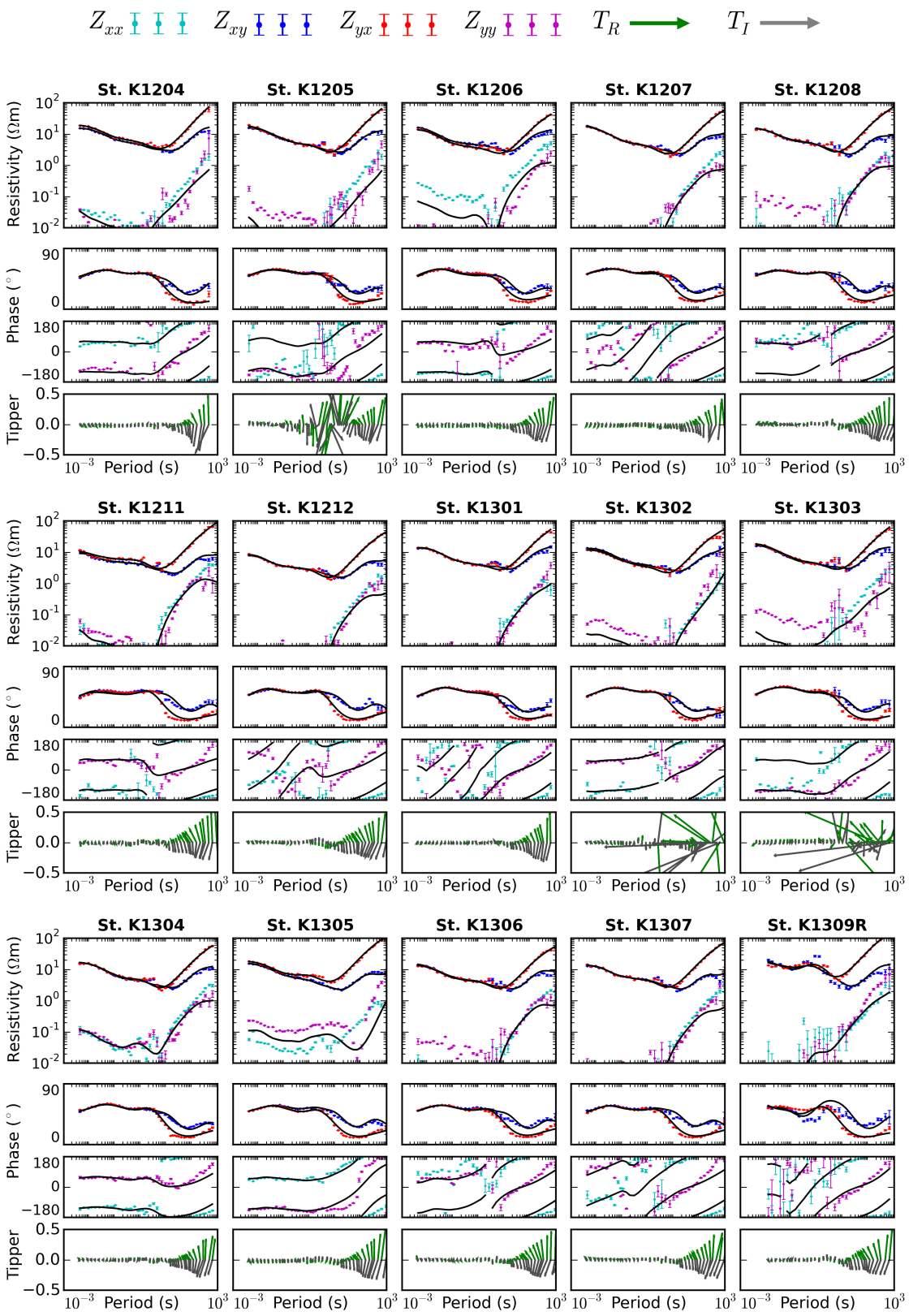

Figure A.9: Koroit resistivity and phase data and responses to the 3D inversion model in Chapter 2 (continued).

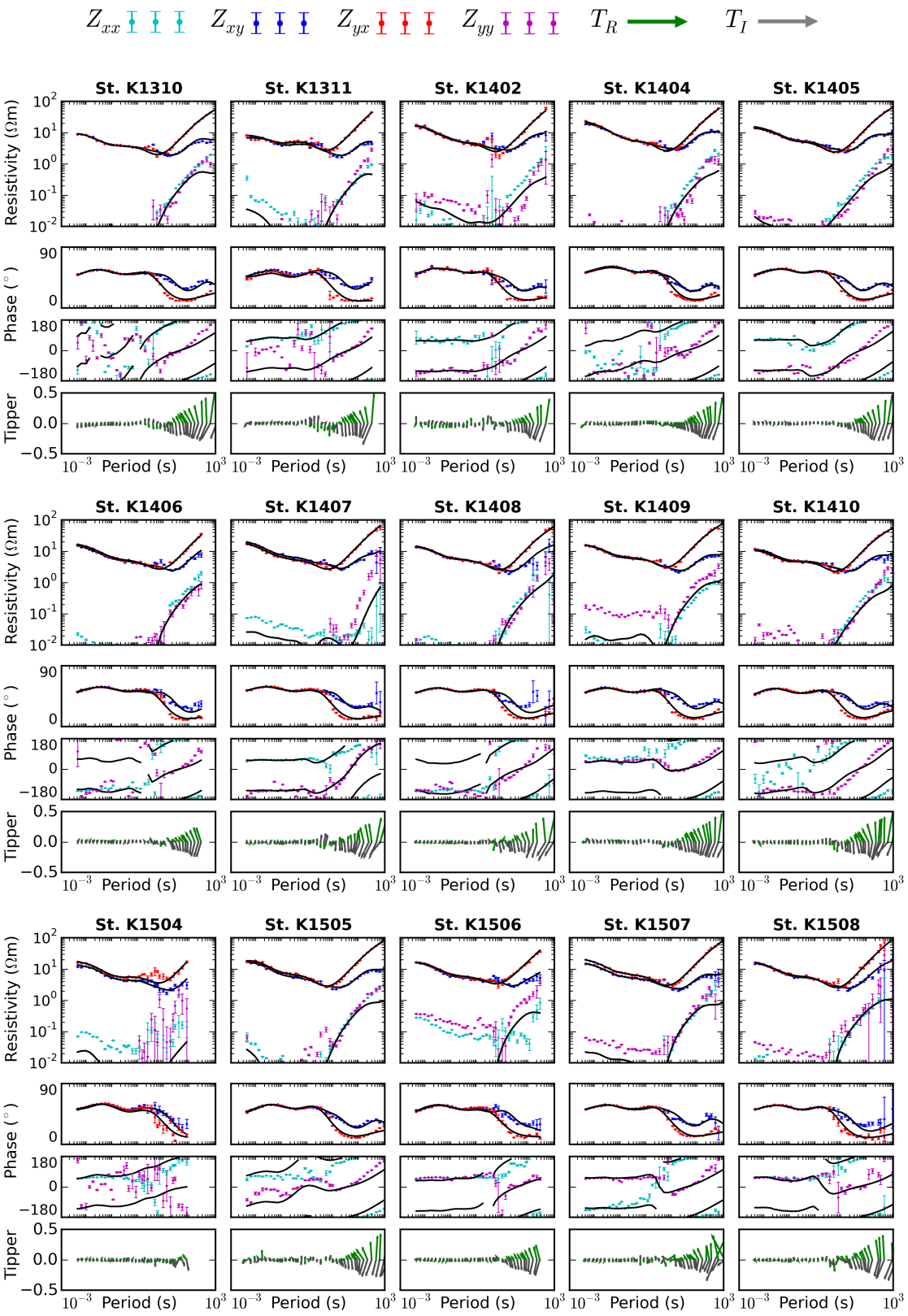

Figure A.10: Koroit resistivity and phase data and responses to the 3D inversion model in Chapter 2 (continued).

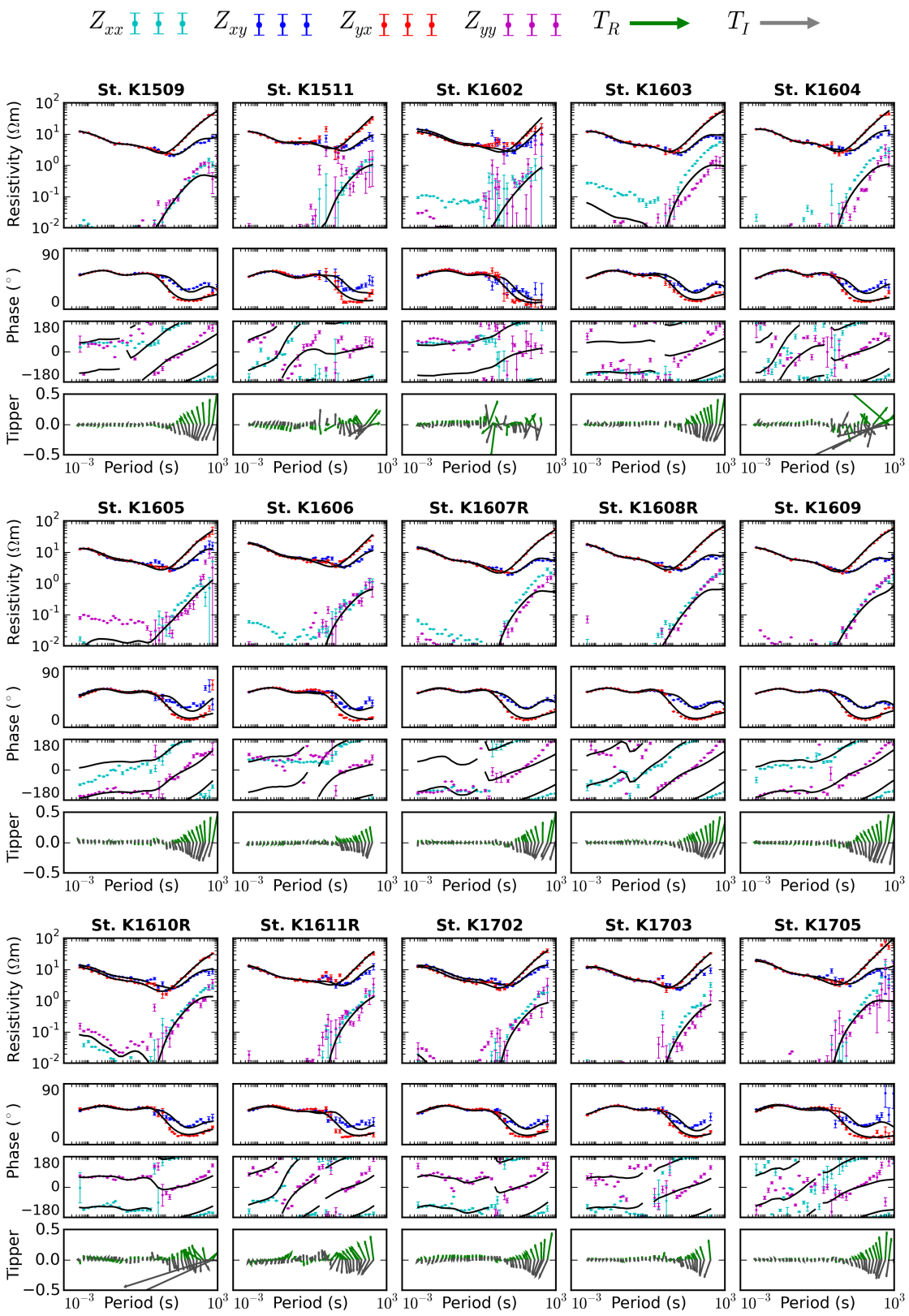

Figure A.11: Koroit resistivity and phase data and responses to the 3D inversion model in Chapter 2 (continued).

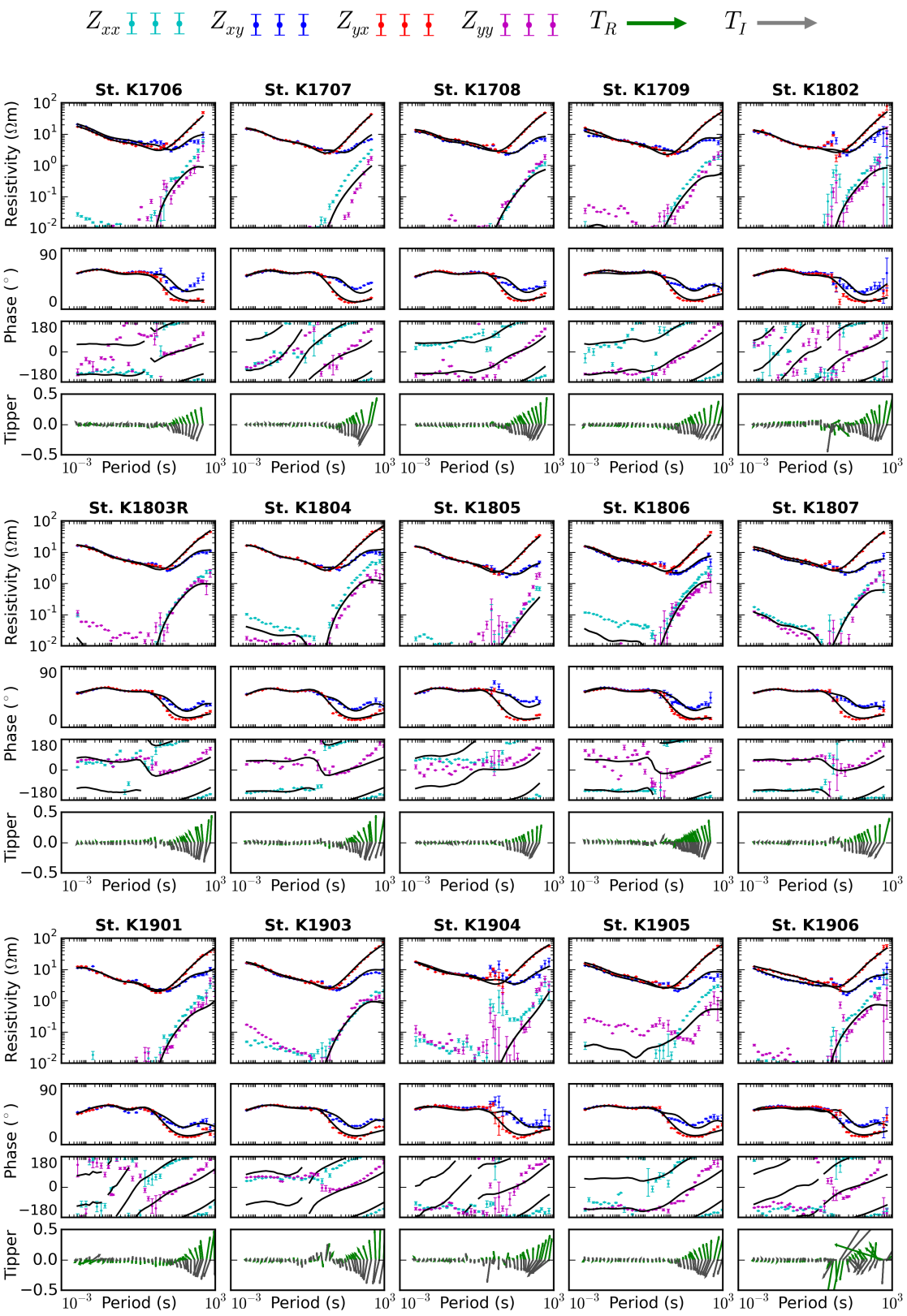

Figure A.12: Koroit resistivity and phase data and responses to the 3D inversion model in Chapter 2 (continued).

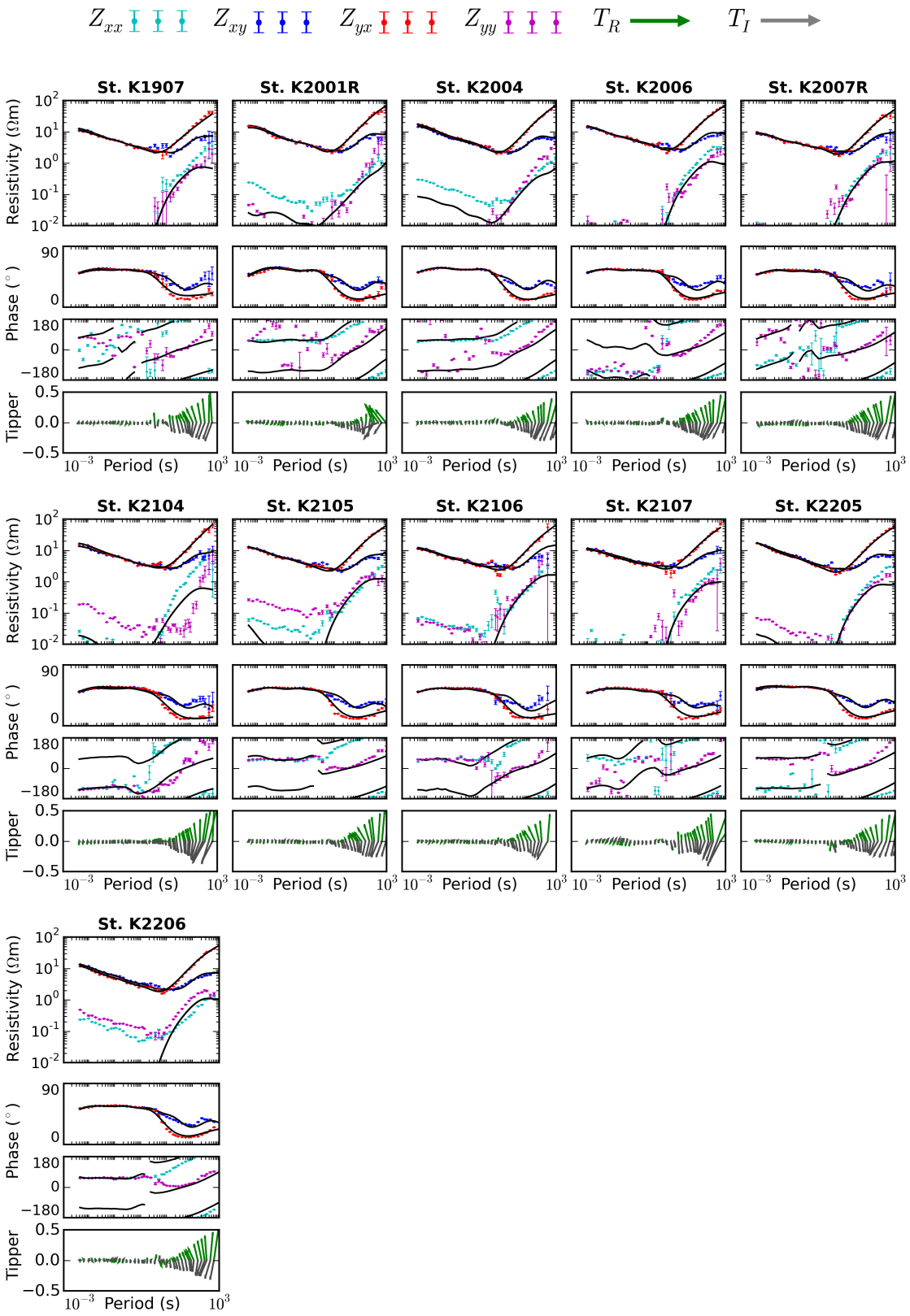

Figure A.13: Koroit resistivity and phase data and responses to the 3D inversion model in Chapter 2 (continued).

APPENDIX

B

SUPPORTING INFORMATION FOR CHAPTER 3

B.1 Station locations

The station locations for the Penola MT survey are shown in Figure B.1 and tabulated in Table B.1.

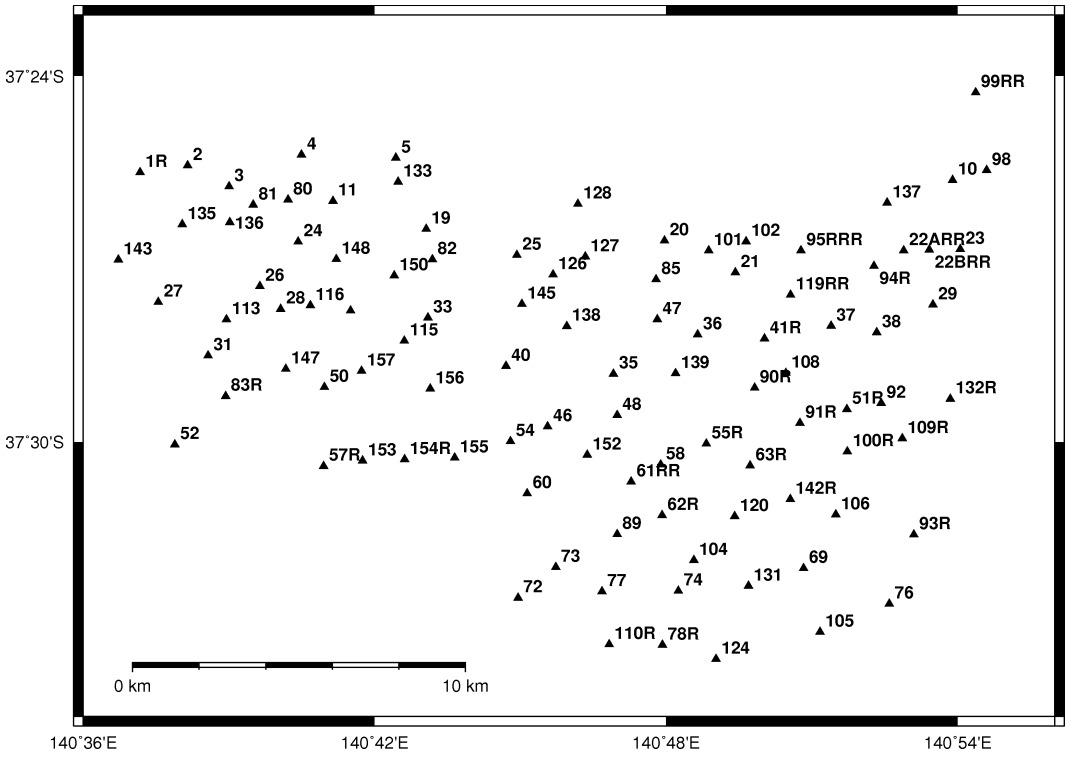

Figure B.1: Locations of the MT stations in the Penola MT survey (Chapter 3)

Table B.1: Locations of stations in Penola Trough MT survey.

Station	Longitude	Latitude	Elevation
10	140.898267	-37.428467	79
1R	140.619550	-37.426350	38
2	140.635850	-37.424483	51
3	140.650083	-37.430233	45
4	140.674917	-37.421550	54
5	140.707283	-37.422383	60
10	140.898267	-37.428467	79
11	140.685733	-37.434183	74
19	140.717717	-37.441850	63
20	140.799433	-37.445050	63
21	140.823753	-37.453717	87
22ARR	140.881494	-37.447731	70
22BRR	140.890269	-37.447514	65
23	140.900867	-37.447350	75
24	140.673767	-37.445317	63
25	140.748800	-37.448983	68
26	140.660650	-37.457483	61
27	140.625783	-37.461833	57
28	140.667783	-37.463717	65
29	140.891517	-37.462517	66
31	140.642867	-37.476433	63
33	140.718283	-37.466083	63
35	140.781933	-37.481433	66
36	140.810817	-37.470700	63
37	140.856583	-37.468333	68
38	140.872217	-37.470100	76
40	140.745067	-37.479300	67
41R	140.833717	-37.471800	84
46	140.759350	-37.495817	70
47	140.796967	-37.466550	67
48	140.783200	-37.492717	66
50	140.682767	-37.485050	63
51R	140.861983	-37.491083	82
52	140.631483	-37.500733	59
54	140.746617	-37.499867	69
55R	140.813783	-37.500533	62
57R	140.682494	-37.506636	66
58	140.798133	-37.506233	83
60	140.752333	-37.514117	68
61RR	140.787983	-37.510883	74
62R	140.798600	-37.520033	84
63R	140.828783	-37.506483	60
69	140.847131	-37.534519	76
72	140.749217	-37.542600	69
73	140.762150	-37.534200	86
74	140.804183	-37.540700	77
76	140.876553	-37.544233	78
77	140.778000	-37.540864	65
78R	140.798731	-37.555431	90
80	140.670317	-37.433833	61

Table B.2: Locations of stations in Penola Trough MT survey (continued).

Station	Longitude	Latitude	Elevation
81	140.658383	-37.435233	52
82	140.719817	-37.450167	67
83R	140.648900	-37.487517	64
85	140.796533	-37.455633	69
89	140.783200	-37.525250	76
90R	140.830367	-37.485250	71
91R	140.845900	-37.494867	68
92	140.873767	-37.489400	72
93R	140.884983	-37.525350	84
94R	140.871300	-37.451967	71
95RRR	140.846256	-37.447733	63
98	140.909933	-37.425750	78
99RR	140.906183	-37.404531	78
100R	140.862167	-37.502633	72
101	140.814600	-37.447717	61
102	140.827433	-37.445250	68
104	140.809517	-37.532317	94
105	140.852767	-37.551914	77
106	140.85800	-37.519867	86
108	140.841083	-37.481233	80
109R	140.881000	-37.499050	70
110R	140.780483	-37.555317	87
113	140.649183	-37.466583	59
115	140.710200	-37.472400	62
116	140.677967	-37.462733	58
119RR	140.842683	-37.459867	64
120	140.823500	-37.520333	69
124	140.817097	-37.559319	95
126	140.761217	-37.454317	69
127	140.772267	-37.449400	70
128	140.769717	-37.435017	60
131	140.828228	-37.539333	75
132R	140.897483	-37.488267	76
133	140.708050	-37.428950	63
135	140.634017	-37.440583	55
136	140.650317	-37.440017	45
137	140.875783	-37.434667	64
138	140.765917	-37.468400	69
139	140.803233	-37.481300	66
142R	140.84260	-37.515683	73
143	140.612117	-37.450233	58
145	140.750533	-37.462367	64
147	140.669550	-37.480083	61
148	140.686850	-37.450117	56
150	140.706717	-37.454567	63
152	140.772950	-37.503567	68
153	140.695867	-37.505150	56
154R	140.71030	-37.504767	59
155	140.727467	-37.504333	68
156	140.71910	-37.485467	56
157	140.695533	-37.480617	64

B.2 Penola input data and responses

This section contains the resistivity and phase data and model responses from the 3D resistivity model presented for the Penola Trough in Chapter 3.

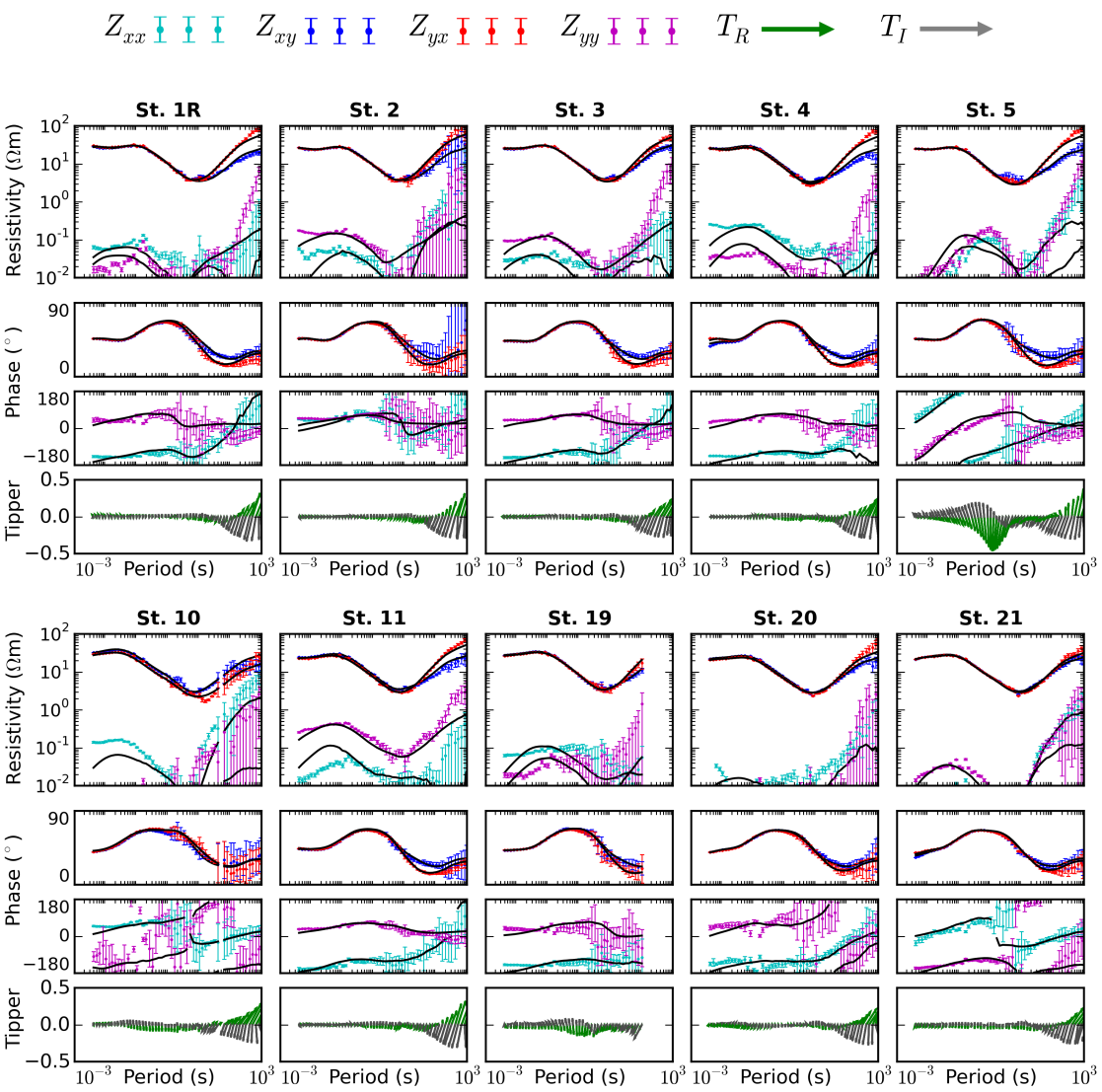

Figure B.2: Penola data and resistivity and phase responses to the 3D inversion model in Chapter 3. Resistivity and phase responses shown in black over the input data; real and imaginary tipper data shown in green and grey.

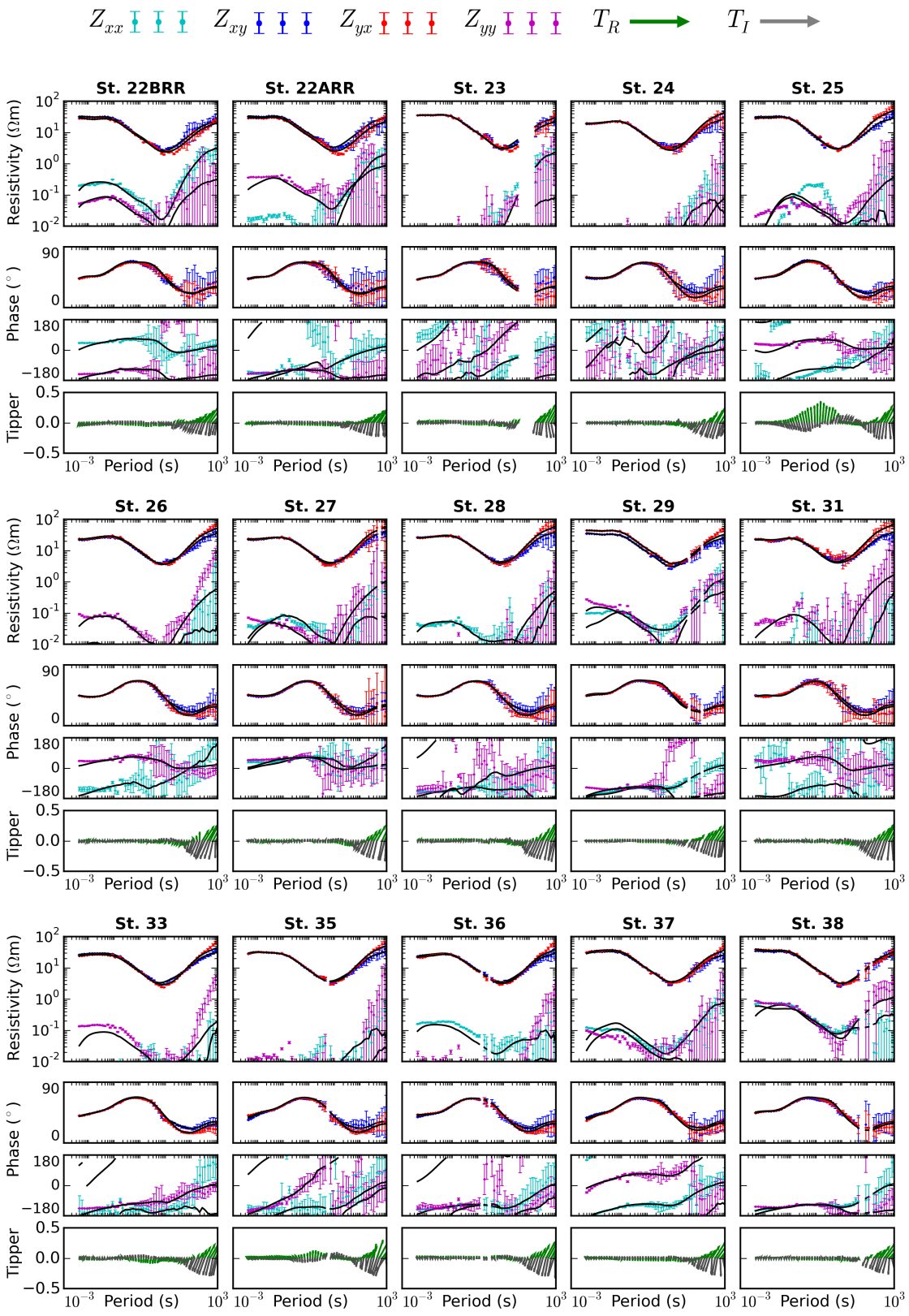

Figure B.3: Penola resistivity and phase data and responses to the 3D inversion model in Chapter 3 (continued).

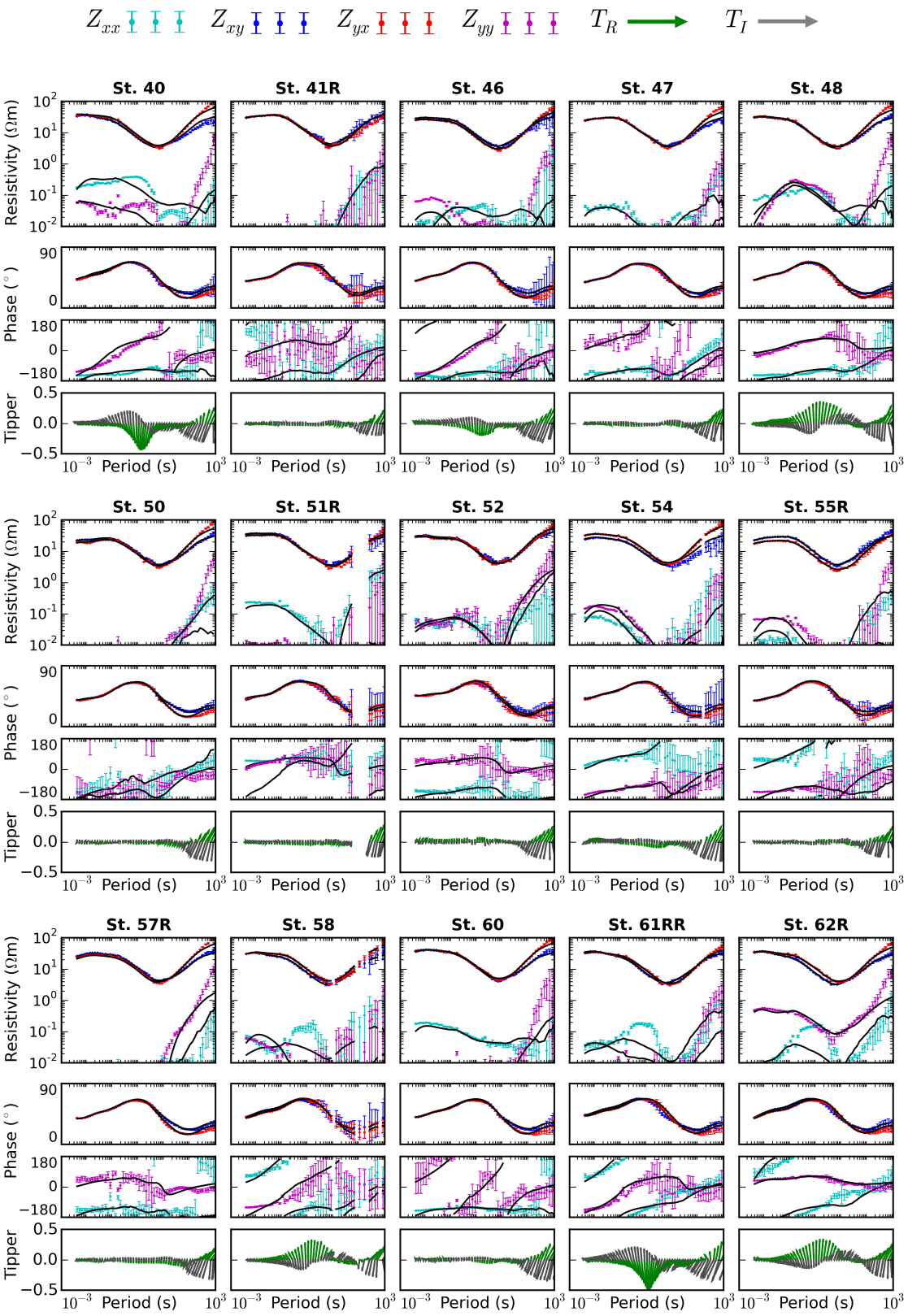

Figure B.4: Penola resistivity and phase data and responses to the 3D inversion model in Chapter 3 (continued).

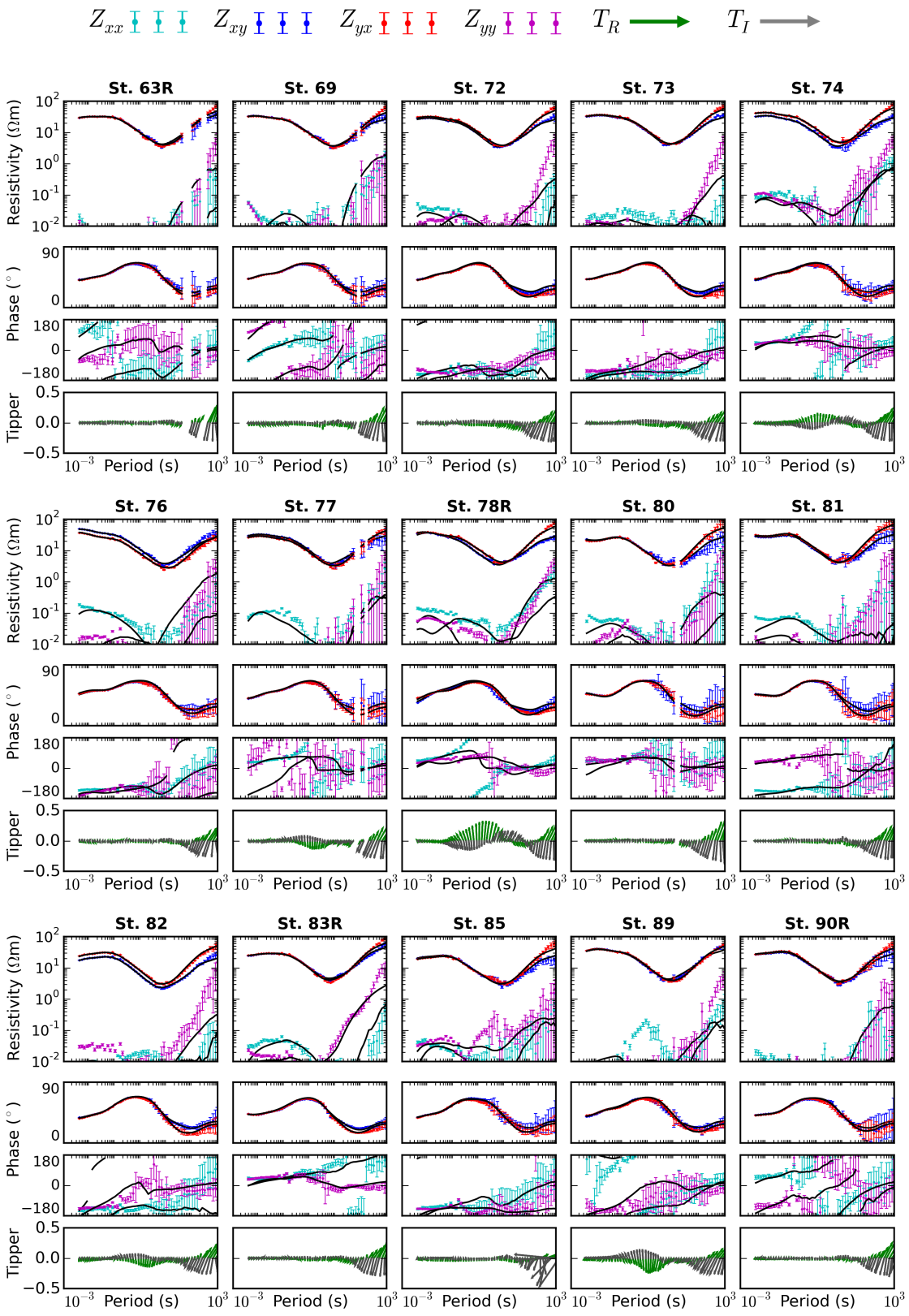

Figure B.5: Penola resistivity and phase data and responses to the 3D inversion model in Chapter 3 (continued).

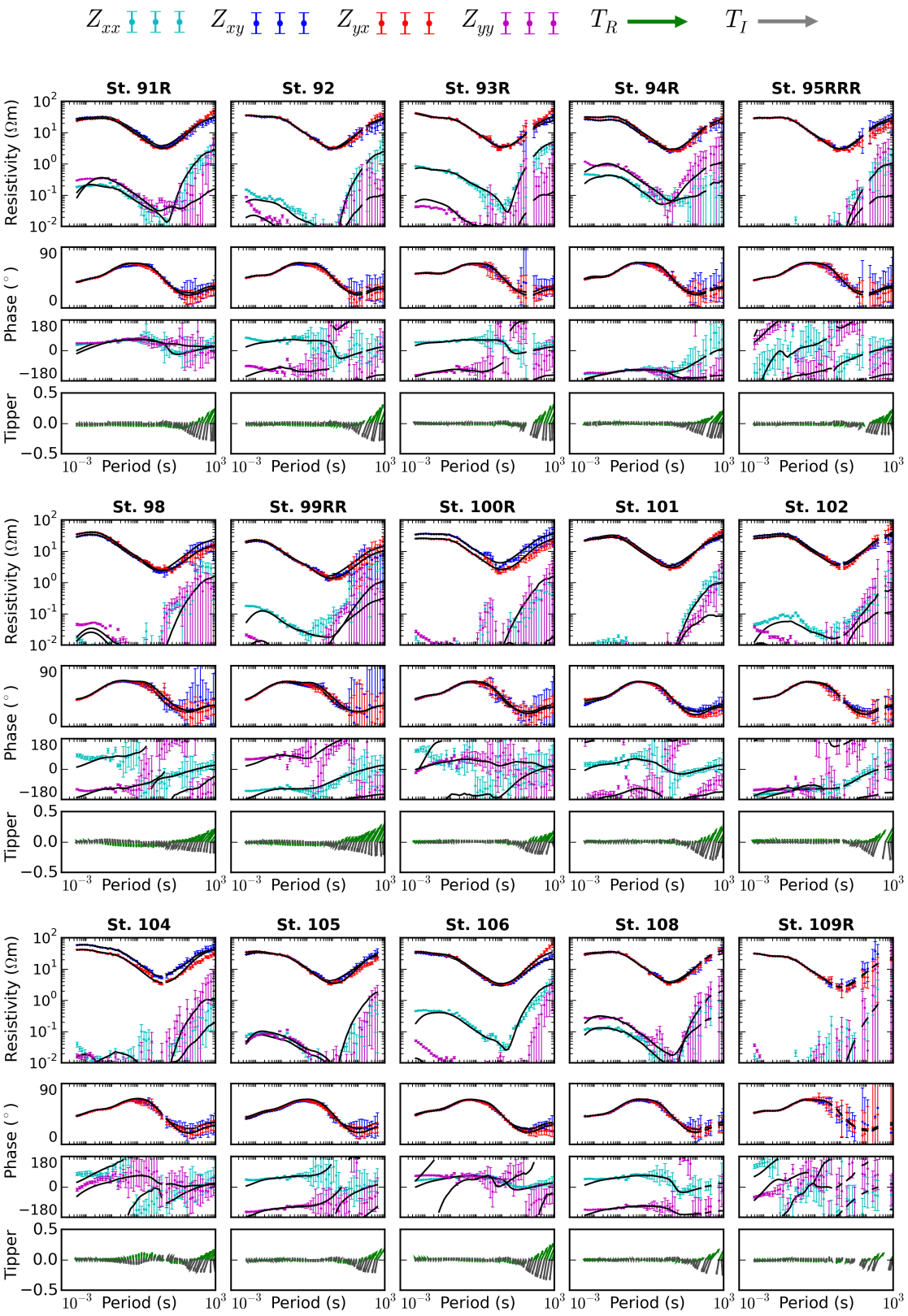

Figure B.6: Penola resistivity and phase data and responses to the 3D inversion model in Chapter 3 (continued).

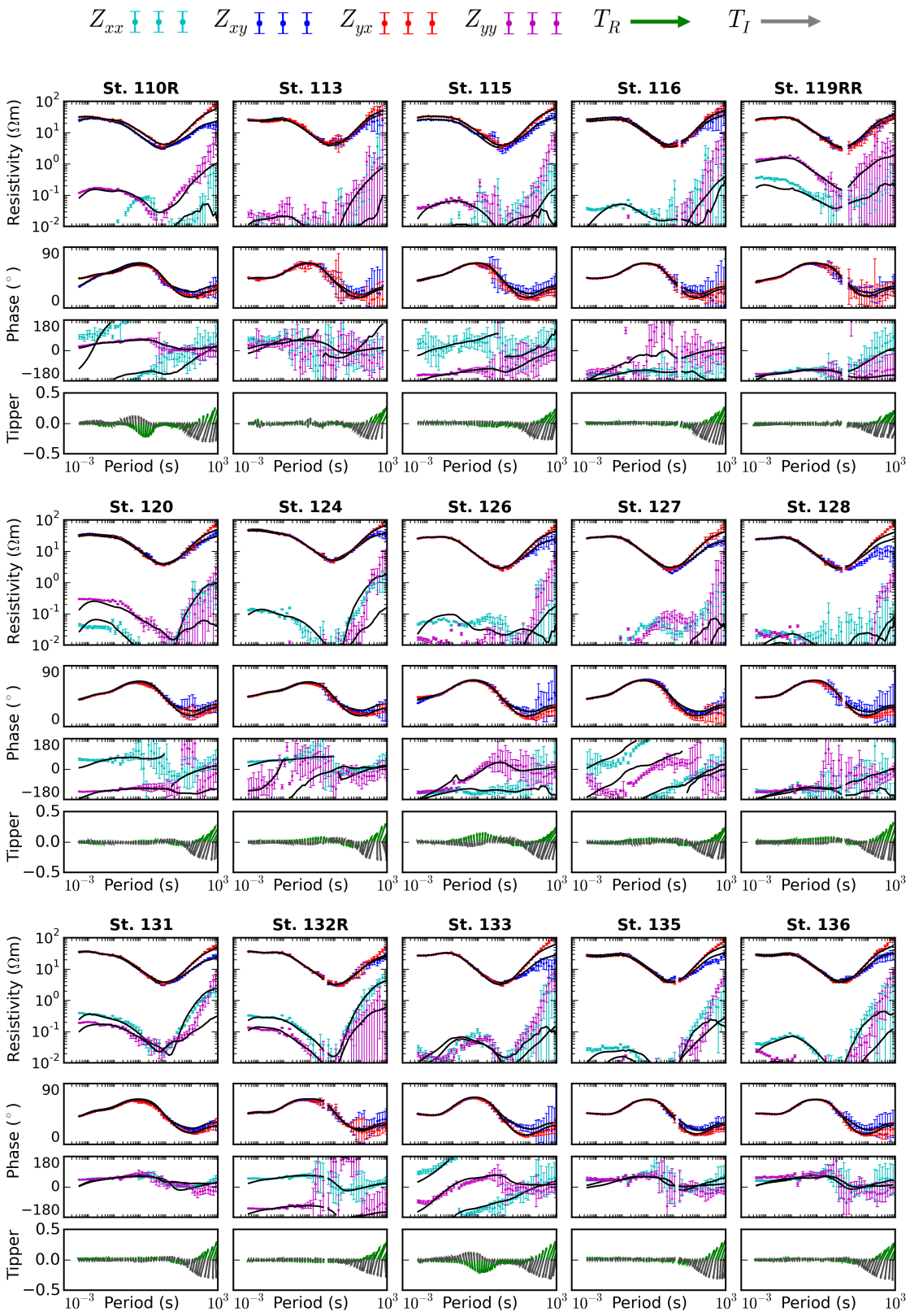

Figure B.7: Penola resistivity and phase data and responses to the 3D inversion model in Chapter 3 (continued).

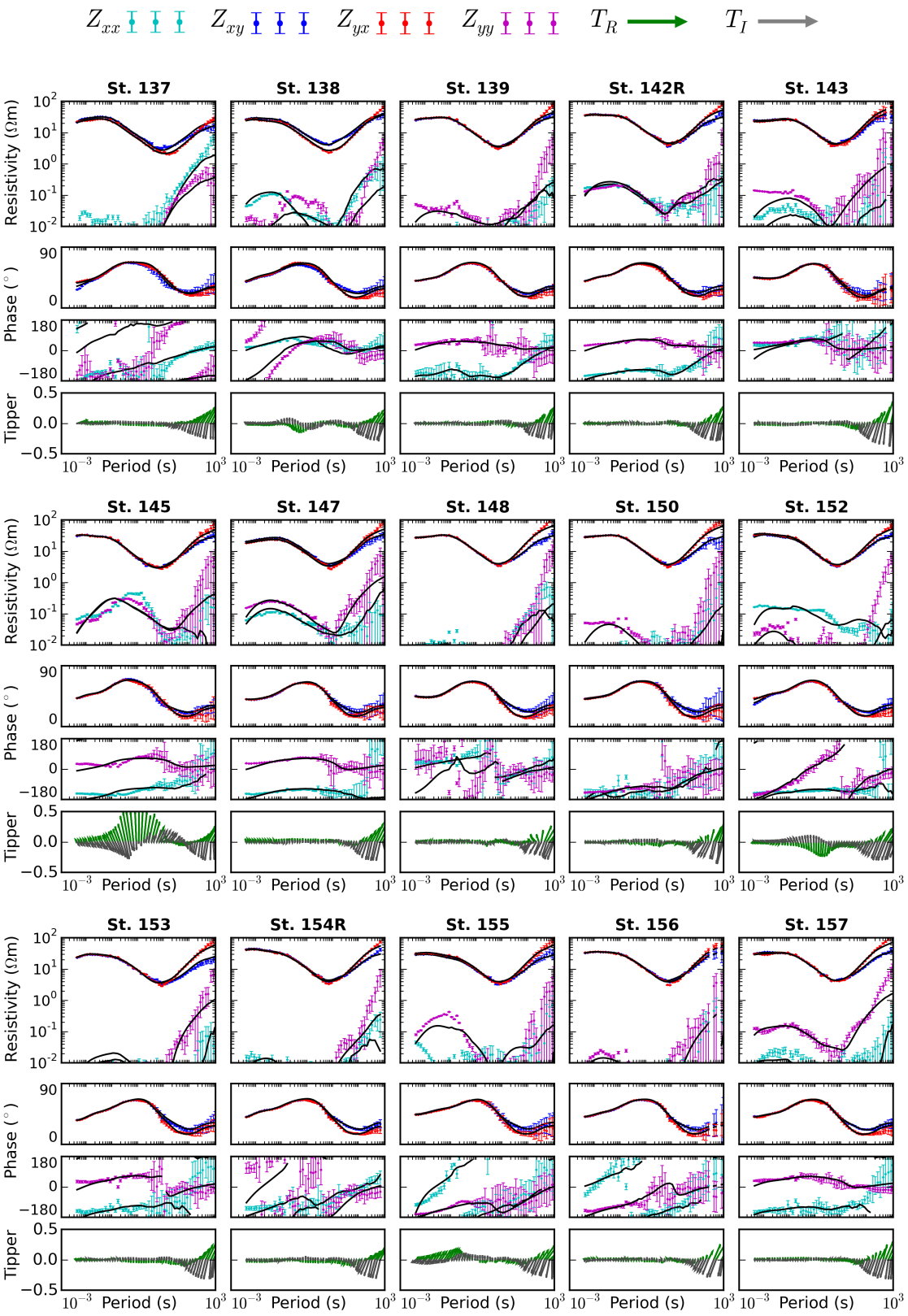

Figure B.8: Penola resistivity and phase data and responses to the 3D inversion model in Chapter 3 (continued).

BIBLIOGRAPHY

3D-Geo (2009). Hot Rock Ltd, Otway Basin Project, Koroit Geothermal Project. Technical report to Hot Rock Ltd, 3D-GEO.

Ackermann, R. V. and Schlische, R. W. (1997). Anticlustering of small normal faults around larger faults. *Geology*, 25(12):1127–1130.

Al-Yaarubi, A. H., Pain, C. C., Grattoni, C. A., and Zimmerman, R. W. (2005). Navier-Stokes simulations of fluid flow through a rock fracture. *Dynamics of fluids and transport in fractured rock*, pages 55–64.

Alexander, E. (1992). Geology and petrophysics of petroleum reservoirs from the Otway Group, Otway Basin. Technical Report 92/70, Department of Mines and Energy South Australia.

Archie, G. (1942). The electrical resistivity log as an aid in determining some reservoir characteristics. *Petroleum Transactions of the Australian Institute of Mining, Metallurgical, and Petroleum Engineers*, 146:54–62.

Babadagli, T. and Al-Salmi, S. (2004). A review of permeability-prediction methods for carbonate reservoirs using well-log data. *SPE Reservoir Evaluation & Engineering*, 7(02):75–88.

Backé, G. V. R., Khair, H. A. F., King, R. C., and Holford, S. P. (2011). Fracture mapping and modelling in shale-gas target in the Cooper Basin, South Australia. *The Australian Petroleum Production and Exploration Association Journal*, 51:397–410.

Bahat, D. (1987). Jointing and fracture interactions in Middle Eocene chalks near Beer Sheva, Israel. *Tectonophysics*, 136(3-4):299–321.

Bahr, K. (1997). Electrical anisotropy and conductivity distribution functions of fractal random networks and of the crust: the scale effect of connectivity. *Geophysical Journal International*, 130(3):649–660.

Bailey, A., King, R., Holford, S., Sage, J., Backe, G., and Hand, M. (2014). Remote sensing of subsurface fractures in the Otway Basin, South Australia. *Journal of Geophysical Research*, 119:6591–6612.

Bain, J. (1962). Pretty Hill 1, southwest Victoria, Well Completion Report. Technical Report 7200-G-94, Frome - Broken Hill Company Pty. Ltd.

Barelli, A., Bertini, G., Buonasorte, G., Cappetti, G., and Fiordelisi, A. (2000). Recent deep exploration results at the margins of the Larderello-Travale geothermal system. In *Proceedings, World Geothermal Congress*, pages 965–970.

Barnett, P. and Evans, T. (2010). Exploration and assessment of Hot Sedimentary Aquifer (HSA) geothermal resources in the Otway Basin Victoria. In Gurgenci, H. and Weber, R., editors, *Proceedings of the 2010 Australian Geothermal Energy Conference*, Record 2010/35, pages 106–111. Geoscience Australia.

Barton, C. A., Hickman, S., Morin, R. H., Zoback, M. D., Finkbeiner, T., Sass, J., and Benoit, D. (1997). Fracture permeability and its relationship to in-situ stress in the Dixie Valley, Nevada, geothermal reservoir. In *Proceedings, Twenty-Second Workshop on Geothermal Reservoir Engineering*.

Barton, C. A., Zoback, M. D., and Moos, D. (1995). Fluid flow along potentially active faults in crystalline rock. *Geology*, 23(8):683–686.

Berkowitz, B. (1989). Boundary conditions along permeable fracture walls: Influence on flow and conductivity. *Water Resources Research*, 25(8):1919–1922.

Berkowitz, B. (1995). Analysis of fracture network connectivity using percolation theory. *Mathematical Geology*, 27(4):467–483.

Berkowitz, B. (2002). Characterizing flow and transport in fractured geological media: A review. *Advances in water resources*, 25(8):861–884.

Bernabé, Y. (1995). The transport properties of networks of cracks and pores. *Journal of Geophysical Research: Solid Earth (1978–2012)*, 100(B3):4231–4241.

Bibby, H. M. (1986). Analysis of multiple-source bipole-quadripole resistivity surveys using the apparent resistivity tensor. *Geophysics*, 51(4):972–983.

Bibby, H. M., Caldwell, T. G., and Brown, C. (2005). Determinable and non-determinable parameters of galvanic distortion in magnetotellurics. *Geophysical Journal International*, 163(3):915–930.

Bittar, M. S., Klein, J. D., Randy, B., Hu, G., Wu, M., Pitcher, J. L., Golla, C., Althoff, G. D., Sitka, M., Minosyan, V., et al. (2009). A new azimuthal deep-reading resistivity tool for geosteering and advanced formation evaluation. *SPE Reservoir Evaluation & Engineering*, 12(02):270–279.

Bonnet, E., Bour, O., Odling, N. E., Davy, P., Main, I., Cowie, P., and Berkowitz, B. (2001). Scaling of fracture systems in geological media. *Reviews of geophysics*, 39(3):347–383.

Boult, P. (2002). *The Petroleum Geology of South Australia: Volume 1. Otway Basin*, chapter 1. Summary and Introduction, pages 1–8. Department of Primary Industries and Resources South Australia.

Boult, P., Camac, B., and Davids, A. (2002a). 3D fault modelling and assessment of top seal structural permeability – Penola Trough, onshore Otway Basin. *The Australian Petroleum Production and Exploration Association Journal*.

Boult, P., White, M., Pollock, R., Morton, J., Alexander, E., and Hill, A. (2002b). *The Petroleum Geology of South Australia: Volume 1. Otway Basin*, chapter 6. Lithostratigraphy and Environments of Deposition, pages 1–98. Department of Primary Industries and Resources South Australia.

Bour, O. and Davy, P. (1997). Connectivity of random fault networks following a power law fault length distribution. *Water Resources Research*, 33(7):1567–1583.

Brown, S. (1989). Transport of fluid and electric current through a single fracture. *Journal of Geophysical Research*, 94(B7):9429–9438.

Brown, S. R. (1987). Fluid flow through rock joints: the effect of surface roughness. *Journal of Geophysical Research: Solid Earth (1978–2012)*, 92(B2):1337–1347.

Brown, S. R. (1995). Simple mathematical model of a rough fracture. *Journal of Geophysical Research: Solid Earth*, 100(B4):5941–5952.

Brown, S. R. and Scholz, C. H. (1985). Broad bandwidth study of the topography of natural rock surfaces. *Journal of Geophysical Research: Solid Earth (1978–2012)*, 90(B14):12575–12582.

Brown, S. R., Stockman, H. W., and Reeves, S. J. (1995). Applicability of the reynolds equation for modeling fluid flow between rough surfaces. *Geophysical Research Letters*, 22(18):2537–2540.

Brush, D. J. and Thomson, N. R. (2003). Fluid flow in synthetic rough-walled fractures: Navier-stokes, stokes, and local cubic law simulations. *Water Resources Research*, 39(4):1–15.

Buckingham, I. (1992). Killara No. 1., Otway Basin, Victoria, Well Completion Report. Technical report, Anglo Australian Oil Company, N.L.

Cagniard, L. (1953). Basic theory of the magneto-telluric method of geophysical prospecting. *Geophysics*, 18(3):605–635.

Caine, J. S., Evans, J. P., and Forster, C. B. (1996). Fault zone architecture and permeability structure. *Geology*, 24(11):1025–1028.

Caldwell, T. G., Bibby, H. M., and Brown, C. (2004). The magnetotelluric phase tensor. *Geophysical Journal International*, 158(2):457–469.

Carman, P. (1937). Fluid flow through granular beds. *Transactions-Institution of Chemical Engineeres*, 15:150–166.

Carson, L., Bradshaw, M., and Jaques, L. (2014). Australian energy resource assessment. Technical report, Geoscience Australia.

Chave, A. D. and Jones, A. G. (2012). *The magnetotelluric method: Theory and practice*. Cambridge University Press.

Clark, D., McPherson, A., and Collins, C. (2011). Australia's seismogenic neotectonic record: a case for heterogeneous intraplate deformation. *Geoscience Australia Record*, 2011/11:1–95.

Constable, S. C., Parker, R. L., and Constable, C. G. (1987). Occam's inversion: A practical algorithm for generating smooth models from electromagnetic sounding data. *Geophysics*, 52(3):289–300.

Cook, A. E., Anderson, B. I., Malinverno, A., Mrozewski, S., and Goldberg, D. S. (2010). Electrical anisotropy due to gas hydrate-filled fractures. *Geophysics*, 75(6):F173–F185.

Crandall, D., Ahmadi, G., and Smith, D. H. (2010). Computational modeling of fluid flow through a fracture in permeable rock. *Transport in porous media*, 84(2):493–510.

Cumming, W. (2009). Geothermal resource conceptual models using surface exploration data. In *Proceedings, Thirty-Fourth Workshop on Geothermal Reservoir Engineering*. Citeseer.

Davies, R. J., Stewart, S. A., Cartwright, J. A., Lappin, M., Johnston, R., Fraser, S. I., and Brown, A. R. (2004). 3D seismic technology: are we realising its full potential? *Geological Society, London, Memoirs*, 29(1):1–10.

de Graaf, B., Reid, I., Palmer, R., Jenson, D., and Parker, K. (2010). Salamander 1: a geothermal well based on petroleum exploration results. In *Proceedings of the 2010 Australian Geothermal Energy Conference*.

Didana, Y. (2016). *Magnetotelluric imaging of conventional and unconventional geothermal resources*. PhD thesis, University of Adelaide.

Drazin, P. G. and Reid, W. H. (2004). *Hydrodynamic stability*. Cambridge university press.

DSD-SA (2015). Petroleum Exploration and Production System South Australia database. `http://petroleum.statedevelopment.sa.gov.au/old-site/access_to_data/peps-sa_database`. Accessed July 2015.

Egbert, G. D. and Kelbert, A. (2012). Computational recipes for electromagnetic inverse problems. *Geophysical Journal International*, 189(1):251–267.

Fossen, H. and Hesthammer, J. (1997). Geometric analysis and scaling relations of deformation bands in porous sandstone. *Journal of Structural Geology*, 19(12):1479–1493.

Fridleifsson, G. O. and Elders, W. A. (2005). The iceland deep drilling project: a search for deep unconventional geothermal resources. *Geothermics*, 34(3):269 – 285.

Garven, G. (1995). Continental-scale groundwater flow and geologic processes. *Annual Review of Earth and Planetary Sciences*, 23:89–118.

Geoscience Australia (2014). Geoscience Australia Petroleum Well Database. `http://dbforms.ga.gov.au/www/npm.well.search`.

Geoscience Victoria (2014). Geovic 3.0 well report. `http://er-info.dpi.vic.gov.au/sd_weave/anonymous.html`.

Glover, P., Matsuki, K., Hikima, R., and Hayashi, K. (1997). Fluid flow in fractally rough synthetic fractures. *Geophysical research letters*, 24(14):1803–1806.

Glover, P., Matsuki, K., Hikima, R., and Hayashi, K. (1998a). Fluid flow in synthetic rough fractures and application to the hachimantai geothermal hot dry rock test site. *Journal of Geophysical Research: Solid Earth (1978–2012)*, 103(B5):9621–9635.

Glover, P., Matsuki, K., Hikima, R., and Hayashi, K. (1998b). Synthetic rough fractures in rocks. *Journal of Geophysical Research: Solid Earth (1978–2012)*, 103(B5):9609–9620.

Glover, P. W. (2010). A generalized archies law for n phases. *Geophysics*, 75(6):E247–E265.

Guéguen, Y., David, C., and Gavrilenko, P. (1991). Percolation networks and fluid transport in the crust. *Geophysical Research Letters*, 18(5):931–934.

Hart, B. S. and Balch, R. S. (2000). Approaches to defining reservoir physical properties from 3-D seismic attributes with limited well control: An example from the Jurassic Smackover Formation, Alabama. *Geophysics*, 65(2):368–376.

Hashin, Z. and Shtrikman, S. (1963). A variational approach to the theory of the elastic behaviour of multiphase materials. *Journal of the Mechanics and Physics of Solids*, 11(2):127–140.

Heise, W., Caldwell, T., Bibby, H., and Brown, C. (2006). Anisotropy and phase splits in magnetotellurics. *Physics of the Earth and Planetary interiors*, 158(2):107–121.

Heise, W. and Pous, J. (2003). Anomalous phases exceeding 90° in magnetotellurics: anisotropic model studies and a field example. *Geophysical Journal International*, 155(1):308–318.

Hermanrud, C. and Bols, H. M. N. (2002). Leakage from overpressured hydrocarbon reservoirs at Haltenbanken and in the northern North Sea. *Norwegian Petroleum Society Special Publications*, 11:221–231.

Herwanger, J., Worthington, M., Lubbe, R., Binley, A., and Khazanehdari, J. (2004). A comparison of cross-hole electrical and seismic data in fractured rock. *Geophysical prospecting*, 52(2):109–121.

Hillis, R. R., Monte, S., Tan, C., and Willoughby, D. R. (1995). The contemporary stress field of the Otway Basin, South Australia: implications for hydrocarbon exploration and production. *The Australian Petroleum Production and Exploration Association Journal*, 35:494–506.

Hogarth, R., Holl, H., and McMahon, A. (2013). Flow testing results from Habanero EGS project. In *Proceedings of the 2013 Australian Geothermal Energy Conference*.

Holford, S. P., Tuitt, A. K., Hillis, R. R., Green, P. F., Stoker, M. S., Duddy, I. R., Sandiford, M., and Tassone, D. R. (2014). Cenozoic deformation in the Otway Basin, southern Australian margin: implications for the origin and nature of post-breakup compression at rifted margins. *Basin Research*, 26(1):10–37.

Hot Rock Ltd. (2009). Stratigraphic horizon interpretations for the Otway Basin. unpublished data.

Hoversten, G. M., Gritto, R., Washbourne, J., and Daley, T. (2003). Pressure and fluid saturation prediction in a multicomponent reservoir using combined seismic and electromagnetic imaging. *Geophysics*, 68(5):1580–1591.

Ishibashi, T., Watanabe, N., Hirano, N., Okamoto, A., and Tsuchiya, N. (2015). Beyond laboratory scale prediction for channeling flows through subsurface rock fractures with heterogeneous aperture distributions revealed by laboratory evaluation. *Journal of Geophysical Research: Solid Earth*, 120:106–124.

Jaeger, J. and Cook, N. (1969). Fundamentals of rock mechanics. *Barnes and Noble, New York*.

Jensen-Schmidt, B., Cockshell, C., and Boult, P. (2002). *The Petroleum Geology of South Australia: Volume 1. Otway Basin*, chapter 5. Structural and tectonic setting, pages 1–14. Department of Primary Industries and Resources South Australia.

Jones, A. G. (1987). MT and reflection: an essential combination. *Geophysical Journal International*, 89(1):7–18.

Jorand, C., Krassay, A., and Hall, L. (2010). Otway Basin Hot Sedimentary Aquifers and SEEBASE (TM) Project. Technical report, FrOG Tech Pty Ltd.

Kelbert, A., Meqbel, N., Egbert, G. D., and Tandon, K. (2014). ModEM: a modular system for inversion of electromagnetic geophysical data. *Computers & Geosciences*, 66:40–53.

Kennedy, W. D., Herrick, D. C., et al. (2004). Conductivity anisotropy in shale-free sandstone. *Petrophysics*, 45(01).

Key, K. (2009). 1D inversion of multicomponent, multifrequency marine CSEM data: Methodology and synthetic studies for resolving thin resistive layers. *Geophysics*, 74(2):F9–F20.

Khamforoush, M., Shams, K., Thovert, J.-F., and Adler, P. (2008). Permeability and percolation of anisotropic three-dimensional fracture networks. *Physical Review E*, 77(5):056307.

Kim, Y.-S., Andrews, J. R., and Sanderson, D. J. (2000). Damage zones around strike-slip fault systems and strike-slip fault evolution, Crackington Haven, southwest England. *Geosciences Journal*, 4(2):53–72.

Kim, Y.-S. and Sanderson, D. J. (2005). The relationship between displacement and length of faults: a review. *Earth-Science Reviews*, 68(3):317–334.

Kirkby, A., Heinson, G., Holford, S., and Thiel, S. (2015). Mapping fractures using 1D anisotropic modelling of magnetotelluric data: a case study from the Otway Basin, Victoria, Australia. *Geophysical Journal International*, 201(3):1961–1976.

Kirkby, A., Heinson, G., and Krieger, L. (2016). Relating permeability and electrical resistivity in fractures using random resistor network models. *Journal of Geophysical Research: Solid Earth*.

Knott, S. D., Beach, A., Brockbank, P. J., Brown, J. L., McCallum, J. E., and Welbon, A. I. (1996). Spatial and mechanical controls on normal fault populations. *Journal of Structural Geology*, 18(2):359–372.

Kozeny, J. (1927). *Über kapillare Leitung des Wassers im Boden:(Aufstieg, Versickerung und Anwendung auf die Bewässerung)*. Hölder-Pichler-Tempsky.

Krassay, A., Cathro, D., and Ryan, D. (2004). A regional tectonostratigraphic framework for the Otway Basin. In *Eastern Australasian Basins Symposium II, Petroleum Exploration Society of Australia, Special Publication*, pages 97–116.

Krieger, L. and Peacock, J. R. (2014). MTpy: A Python toolbox for magnetotellurics. *Computers & Geosciences*, 72(0):167 – 175.

Ladeira, F. and Price, N. (1981). Relationship between fracture spacing and bed thickness. *Journal of Structural Geology*, 3(2):179–183.

Law, B. E. and Curtis, J. B. (2002). Introduction to unconventional petroleum systems. *AAPG Bulletin*, 86(11):1851–1852.

Li, Q., Omeragic, D., Chou, L., Yang, L., Duong, K., et al. (2005). New directional electromagnetic tool for proactive geosteering and accurate formation evaluation while drilling. In *SPWLA 46th Annual Logging Symposium*. Society of Petrophysicists and Well-Log Analysts.

Long, J. and Witherspoon, P. A. (1985). The relationship of the degree of interconnection to permeability in fracture networks. *Journal of Geophysical Research: Solid Earth*, 90(B4):3087–3098.

Lüschen, E., Görne, S., Hartmann, H., Thomas, R., and Schulz, R. (2015). 3D seismic survey for geothermal exploration in crystalline rocks in Saxony, Germany. *Geophysical Prospecting*, 63(4):975–989.

Lüschen, E., Wolfgramm, M., Fritzer, T., Dussel, M., Thomas, R., and Schulz, R. (2014). 3D seismic survey explores geothermal targets for reservoir characterization at Unterhaching, Munich, Germany. *Geothermics*, 50:167–179.

Lyon, P., Boult, P., Watson, M., and Hillis, R. (2005a). A systematic fault seal evaluation of the Ladbroke Grove and Pyrus traps of the Penola Trough, Otway Basin. *The Australian Petroleum Production and Exploration Association Journal*, 45(1):459 – 474.

Lyon, P. J., Boult, P. J., Hillis, R. R., and Mildren, S. D. (2005b). Sealing by shale gouge and subsequent seal breach by reactivation: A case study of the Zema Prospect, Otway Basin. *American Association of Petroleum Geology special volumes*, pages 179 – 197.

MacFarlane, J., Thiel, S., Pek, J., Peacock, J., and Heinson, G. (2014). Characterisation of induced fracture networks within an enhanced geothermal system using anisotropic electromagnetic modelling. *Journal of Volcanology and Geothermal Research*, 288:1–7.

MacGregor, L., Sinha, M., and Constable, S. (2001). Electrical resistivity structure of the Valu Fa Ridge, Lau Basin, from marine controlled-source electromagnetic sounding. *Geophysical Journal International*, 146(1):217–236.

Madadi, M., VanSiclen, C. D., and Sahimi, M. (2003). Fluid flow and conduction in two-dimensional fractures with rough, self-affine surfaces: A comparative study. *Journal of Geophysical Research: Solid Earth*, 108(B8). 2396.

Mandelbrot, B. B. (1983). *The fractal geometry of nature*, volume 1. New York, WH Freeman and Co., 1983, 495 p.

Marrett, R. and Allmendinger, R. W. (1991). Estimates of strain due to brittle faulting: sampling of fault populations. *Journal of Structural Geology*, 13(6):735–738.

Martí, A. (2014). The role of electrical anisotropy in magnetotelluric responses: From modelling and dimensionality analysis to inversion and interpretation. *Surveys in Geophysics*, 35(1):179–218.

Matsuki, K., Chida, Y., Sakaguchi, K., and Glover, P. (2006). Size effect on aperture and permeability of a fracture as estimated in large synthetic fractures. *International Journal of Rock Mechanics and Mining Sciences*, 43(5):726 – 755.

Mohais, R., Xu, C., Dowd, P., and Hand, M. (2012). Permeability correction factor for fractures with permeable walls. *Geophysical Research Letters*, 39(3).

Morton, J., Sansome, A., and Boult, P. (2002). *The Petroleum Geology of South Australia: Volume 1. Otway Basin*, chapter 10. Reservoirs and seals, pages 1–30. Department of Primary Industries and Resources South Australia.

Mourzenko, V., Thovert, J.-F., and Adler, P. (2005). Percolation of three-dimensional fracture networks with power-law size distribution. *Physical Review E*, 72(3):036103.

Mourzenko, V., Thovert, J.-F., and Adler, P. (2011). Permeability of isotropic and anisotropic fracture networks, from the percolation threshold to very large densities. *Physical Review E*, 84(3):036307.

Muñoz, G. (2014). Exploring for geothermal resources with electromagnetic methods. *Surveys in Geophysics*, 35(1):101–122.

Muraoka, H. and Kamata, H. (1983). Displacement distribution along minor fault traces. *Journal of Structural Geology*, 5(5):483–495.

Nabawy, B. S., Rochette, P., and Graud, Y. (2010). Electric pore fabric of the nubia sandstones in south egypt: characterization and modelling. *Geophysical Journal International*, 183(2):681–694.

Naif, S., Key, K., Constable, S., and Evans, R. (2013). Melt-rich channel observed at the lithosphere-asthenosphere boundary. *Nature*, 495(7441):356–359.

Nelson, E., Hillis, R., Sandiford, M., Reynolds, S., and Mildren, S. (2006). Present-day state-of-stress of Southeast Australia. *The Australian Petroleum Production and Exploration Association Journal*, 46(1):283–305.

Nelson, P. H. (1994). Permeability-porosity relationships in sedimentary rocks. *The Log Analyst*, 35(03):38–61.

Newman, G. A., Commer, M., and Carazzone, J. J. (2010). Imaging CSEM data in the presence of electrical anisotropy. *Geophysics*, 75(2):F51–F61.

Nicholl, M., Rajaram, H., Glass, R., and Detwiler, R. (1999). Saturated flow in a single fracture: Evaluation of the Reynolds equation in measured aperture fields. *Water Resources Research*, 35(11):3361–3373.

Odling, N., Gillespie, P., Bourgine, B., Castaing, C., Chiles, J., Christensen, N., Fillion, E., Genter, A., Olsen, C., Thrane, L., et al. (1999). Variations in fracture system geometry and their implications for fluid flow in fractured hydrocarbon reservoirs. *Petroleum Geoscience*, 5(4):373–384.

Ogilvie, S. R., Isakov, E., and Glover, P. W. (2006). Fluid flow through rough fractures in rocks. ii: A new matching model for rough rock fractures. *Earth and Planetary Science Letters*, 241(3):454–465.

O'Neil, B. (2002). *The Petroleum Geology of South Australia: Volume 1. Otway Basin*, chapter 2. History of petroleum exploration and development, pages 1–27. Department of Primary Industries and Resources South Australia.

Pape, H., Clauser, C., and Iffland, J. (1999). Permeability prediction based on fractal porespace geometry. *Geophysics*, 64(5):1447–1460.

Parkinson, W. (1959). Directions of rapid geomagnetic fluctuations. *Geophysical Journal International*, 2(1):1–14.

Peacock, J. (2012). *Magnetotelluric Monitoring*. PhD thesis, University of Adelaide.

Peacock, J. R., Thiel, S., Heinson, G., and Reid, P. (2013). Time-lapse magnetotelluric monitoring of an enhanced geothermal system. *Geophysics*, 78(3):B121–B130.

Peacock, J. R., Thiel, S., Reid, P., and Heinson, G. (2012). Magnetotelluric monitoring of a fluid injection: Example from an enhanced geothermal system. *Geophysical Research Letters*, 39(18):1–5.

Pek, J. and Santos, F. A. (2006). Magnetotelluric inversion for anisotropic conductivities in layered media. *Physics of the Earth and Planetary Interiors*, 158(24):139 – 158.

Pellerin, L., Johnston, J. M., and Hohmann, G. W. (1996). A numerical evaluation of electromagnetic methods in geothermal exploration. *Geophysics*, 61(1):121–130.

Perincek, D. and Cockshell, C. D. (1995). The Otway Basin: early Cretaceous rifting to Neogene inversion. *The Australian Petroleum Production and Exploration Association Journal*, 35:451–451.

Pramanik, A., Singh, V., Vig, R., Srivastava, A., and Tiwary, D. (2004). Estimation of effective porosity using geostatistics and multiattribute transforms: A case study. *Geophysics*, 69(2):352–372.

Reches, Z. (1986). Networks of shear faults in the field and in experiments. In *Fragmentation, form and flow in fractured media*, volume 8, pages 42–51. Israel Physics Society.

Rees, N., Carter, S., Heinson, G., and Krieger, L. (2016a). Monitoring shale gas resources in the Cooper Basin using magnetotellurics. *Geophysics*, In press. Accepted manuscript.

Rees, N., Carter, S., Heinson, G., Krieger, L., Conway, D., Boren, G., and Matthews, C. (2016b). Magnetotelluric monitoring of coal-seam gas and shale-gas resource development in Australia. *The Leading Edge*, 35(1):64–70.

Rees, N., Heinson, G., and Krieger, L. (2016c). Magnetotelluric monitoring of coal seam gas depressurisation. *Geophysical Research Letters*.

Reid, P. and Messeiller, M. (2013). Paralana Engineered Geothermal Systems project 3.5MW development plan. In *Proceedings of the 2013 Australian Geothermal Energy Conference*.

Reynolds, O. (1883). An experimental investigation of the circumstances which determine whether the motion of water shall be direct or sinuous, and of the law of resistance in parallel channels. *Proceedings of the royal society of London*, 35(224-226):84–99.

Roberts, A. (2001). Curvature attributes and their application to 3-D interpreted horizons. *First break*, 19(2):85–100.

Robertson, K., Taylor, D., Thiel, S., and Heinson, G. (2015). Magnetotelluric evidence for serpentinisation in a Cambrian subduction zone beneath the Delamerian Orogen, southeast Australia. *Gondwana Research*. http://dx.doi.org/10.1016/j.gr.2014.07.013.

Rosas-Carbajal, M., Linde, N., Peacock, J., Zyserman, F., Kalscheuer, T., and Thiel, S. (2015). Probabilistic 3-D time-lapse inversion of magnetotelluric data: application to an enhanced geothermal system. *Geophysical Journal International*, 203(3):1946–1960.

Russell, B., Hampson, D., Schuelke, J., and Quirein, J. (1997). Multiattribute seismic analysis. *The Leading Edge*, 16(10):1439–1443.

Ryan, S., Knight, L., and Parker, G. (1995). The stratigraphy and structure of the Tyrendarra Embayment, Otway Basin, Victoria. Victorian Initiative for Minerals and Petroleum Report 15, Department of Agriculture, Energy and Minerals.

Schlische, R. W., Young, S. S., Ackermann, R. V., and Gupta, A. (1996). Geometry and scaling relations of a population of very small rift-related normal faults. *Geology*, 24(8):683–686.

Scholz, C. and Cowie, P. (1990). Determination of geologic strain from fault slip data. *Nature*, 346:837–839.

Scholz, F. (2009). *Electroanalytical methods: guide to experiments and applications*. Springer Science & Business Media.

Simpson, F. and Bahr, K. (2005). *Practical magnetotellurics*. Cambridge University Press.

Tassone, D. (2014). *Compressional deformation and exhumation in sedimentary basins at 'passive' continental margins, with implications for hydrocarbon exploration and development*. PhD thesis, Australian School of Petroleum.

Telfer, A. (1993). Groundwater resource management and community consultation – Blue Lake, South Australia. *Australian Journal of Geology and Geophysics*, 14(2):201–206.

Tester, J., Blackwell, D., Petty, S., Richards, M., Moore, M., Anderson, B., Livesay, B., Augustine, C., DiPippo, R., Nichols, K., et al. (2007). The future of geothermal energy: an assessment of the energy supply potential of engineered geothermal systems (egs) for the united states. In *Proc. 32nd workshop on geothermal reservoir engineering, Stanford University*.

Tiab, D. and Donaldson, E. C. (2012). *Petrophysics: Theory and Practice of Measuring Reservoir Rock and Fluid Transport Properties*. Elsevier, 3 edition.

Tikhonov, A. N. (1950). On determining electrical characteristics of the deep layers of the Earth's crust. *Doklady Akademii Nauk*, 2:295–297.

Ussher, G., Harvey, C., Johnstone, R., and Anderson, E. (2000). Understanding the resistivities observed in geothermal systems. In *Proceedings of the World Geothermal Congress*, pages 1915–1920.

Van Siclen, C. D. (2002). Equivalent channel network model for permeability and electrical conductivity of fracture networks. *Journal of Geophysical Research: Solid Earth*, 107(B6):ECV 1–1–ECV 1–10.

Vandenberg, A. (2000). The Tasman Fold Belt system in Victoria: geology and mineralisation of Proterozoic to Carboniferous rocks. Technical Report Geological Survey of Victoria Special Publication, Department of Agriculture, Energy and Minerals, Victoria.

Wang, T. and Fang, S. (2001). 3-D electromagnetic anisotropy modeling using finite differences. *Geophysics*, 66(5):1386–1398.

Wannamaker, P. E. (2005). Anisotropy versus heterogeneity in continental solid earth electromagnetic studies: Fundamental response characteristics and implications for physicochemical state. *Surveys in Geophysics*, 26(6):733–765.

Watterson, J. (1986). Fault dimensions, displacements and growth. *Pure and Applied Geophysics*, 124(1-2):365–373.

Weckmann, U., Ritter, O., and Haak, V. (2003). A magnetotelluric study of the Damara Belt in Namibia: 2. MT phases over 90 reveal the internal structure of the Waterberg Fault/Omaruru Lineament. *Physics of the Earth and Planetary Interiors*, 138(2):91–112.

Witherspoon, P., Wang, J., Iwai, K., and Gale, J. (1980). Validity of cubic law for fluid flow in a deformable rock fracture. *Water Resources Research*, 16(6):1016–1024.

Wright, P. M., Ward, S. H., Ross, H. P., and West, R. C. (1985). State-of-the-art geophysical exploration for geothermal resources. *Geophysics*, 50(12):2666–2696.

Xu, C. and Dowd, P. (2010). A new computer code for discrete fracture network modelling. *Computers & Geosciences*, 36(3):292 – 301.

Yazdi, A., Hamzehpour, H., and Sahimi, M. (2011). Permeability, porosity, and percolation properties of two-dimensional disordered fracture networks. *Physical Review E*, 84(4):046317.